

TECHNISCHE UNIVERSITÄT MÜNCHEN
Lehrstuhl für Physikalische Chemie

**Reactivity of Cluster Model Catalysts:
Influence of Support Material Properties and
Reaction Conditions**

Vahideh Habibpour

Vollständiger Abdruck der von der Fakultät für Chemie der Technische Universität München zur Erlangung des akademischen Grades eines

Doktors der Naturwissenschaften

genehmigten Dissertation.

Vorsitzender: Univ.-Prof. Dr. K.-O. Hinrichsen

Prüfer der Dissertation:

1. Univ.-Prof. Dr. U. K. Heiz
2. Univ.-Prof. Dr. K. Köhler

Die Dissertation wurde am 15.06.2009 bei der Technischen Universität München eingereicht und durch die Fakultät für Chemie am 21.07.2009 angenommen.

Abstract	1
Chapter 1	5
1. Introduction	5
1.1. Factors controlling the activity of cluster model catalysts.....	6
1.1.1. Nanocatalytic factors	7
1.1.2. Support-induced factors	12
1.1.3. Kinetic factors.....	17
1.1.4. Cooperative coadsorption factors.....	18
1.2. Content of this thesis.....	19
Chapter 2	21
2. Experimental setup	21
2.1. Cluster source, ion optics and mass selector.....	22
2.2. Analysis chamber.....	24
2.2.1. Cleaning of metal single crystals.....	25
2.2.2. Synthesise of thin oxide films	26
2.2.3. Characterisation methods.....	26
2.2.4. Calibration of the pulsed-valves and molecular beam doser.....	30
2.3. Micro-calorimeter chamber.....	32
2.3.1. Cantilever array sensor	33
2.3.2. Optical element.....	34
Chapter 3	37
3. Preparation and characterisation of model catalysts.....	37
3.1. Preparation and characterisation of thin oxide films.....	37
3.1.1. Preparation of MgO and SiO ₂ thin films.....	38
3.1.2. Characterisation of thin films	40
3.2. Exploration of the reactivity of cluster-based catalysts.....	53
3.2.1. Principles of temperature programmed desorption experiments.....	53
3.2.2. Introduction to CO combustion on surfaces	54
3.2.3. Experimental.....	57
3.2.4. Theoretical.....	58
3.2.5. Results and discussions	59
3.2.6. Summary	67
Chapter 4	69
4. Catalysis of magnesia supported Au ₂₀ clusters.....	69
4.1. Tuning of the catalytic performance of Au ₂₀ model catalysts.....	69

Table of contents

4.1.1.	Experimental and theoretical methods	70
4.1.2.	Experimental and theoretical findings	71
4.2.	Reaction mechanisms of CO combustion on supported Au ₂₀ clusters	75
4.2.1.	Low-temperature mechanisms on thin defect-poor MgO films	75
4.2.2.	High-temperature mechanisms on thin defect-poor MgO films	77
4.2.3.	Reaction mechanisms on thick defect-poor MgO films	77
4.2.4.	Reaction mechanisms on thick defect-rich MgO films	78
4.3.	Summary	80
Chapter 5	83
5.	Catalysis of oxygen treated palladium cluster catalysts	83
5.1.	Reactivity of oxygen treated Pd ₁₃ clusters	84
5.1.1.	TPR type I	85
5.1.2.	TPR type II	86
5.1.3.	TPR type III	87
5.2.	Reactivity of oxygen treated Pd ₃₀ cluster catalysts	89
5.3.	FTIR investigations of palladium clusters	90
5.3.1.	Pd ₉ cluster catalysts	91
5.3.2.	Pd ₁₃ cluster catalysts	92
5.3.3.	Pd ₃₀ cluster catalysts	92
5.3.4.	Pd _n cluster catalysts	93
5.4.	Summary	95
Chapter 6	97
6.	Micro-cantilever sensors	97
6.1.	Experimental	98
6.2.	Operation modes and properties of bimetallic cantilevers	99
6.3.	Calibration of the calorimeter	100
6.3.1.	Sensitivity of the bimetallic-cantilevers	100
6.3.2.	Response time of the bimetallic-cantilever	101
6.4.	Calorimetric applications	106
6.4.1.	Cluster binding energies	106
6.4.2.	Hydrogenation of 1,3-butadiene on Pd model catalysts	108
	Hydrogen interaction on palladium clusters	113
6.5.	Summary	114
Appendix A	115
A.1.	Auger electron spectroscopy	115
A.2.	Theory of Auger electron spectroscopy	115

Table of contents

A.3. AES instrumentation.....	116
Appendix B	121
B.1. Introduction to FTIR spectroscopy	121
B.2. IR frequency range and spectrum presentation	121
B.3. Theory of infrared absorption/vibrational spectroscopy.....	122
B.4. FTIR instrumentation.....	123
B.5. Spectrometer components	123
Appendix C	125
C.1. Electron spectroscopy with metastable atoms	125
C.2. De-excitation mechanisms	125
C.3. Instrumentation.....	127
Appendix D	129
TPR simulations	129
Acknowledgements	133
References	135

Abstract

Since the early days of heterogeneous catalysis, the development of methods to control and design cluster-based catalysts with specific functions has been one of the major goals of modern research in catalysis. In this context, a molecular- or atomic-scale understanding of the reaction energetics is required, since the intrinsic properties of the catalysts may change in the nanoscale regimes. The catalytic activities of nanometer-sized metal clusters, supported on thin oxide films (< 15 ML) are further affected by the atomic structure, size of the clusters and support properties. The experimental and theoretical investigations performed in the present PhD thesis aim to address the dependency of the catalytic activities on the thickness of magnesia films, dimensionalities of adsorbed clusters, and oxygen pretreatment of the catalysts. Since the catalytic activity of cluster model catalysts depends sensitively on the support properties, MgO films of various thicknesses and defect concentrations were initially characterised using Auger electron spectroscopy, metastable helium impact electron spectroscopy and ultraviolet photoelectron spectroscopy. To explore the contribution of the non-reactive spill-over of reactants on the support material in CO oxidation reaction, temperature programmed reaction spectra were simulated using Langmuir-Hinshelwood based kinetics. The observed changes of the reactivity of various model catalysts through experiments (temperature programmed reaction and Fourier transform infrared spectroscopy for Au₂₀ and Pd₃₀ and Pd₁₃ clusters) and first-principles theoretical calculations (only for gold clusters) can be summarised as follow:

- **CO-combustion on Au₂₀:** The oxidation of carbon monoxide on 20-atom gold clusters is shown to depend on the thickness and stoichiometry of the magnesia films grown on a molybdenum single crystal. These dependencies are reflected in variations of the reaction temperatures, the amount of carbon dioxide produced and vibrational frequencies of adsorbed carbon monoxide. The observed changes are correlated with the dimensionality crossover from three-dimensional tetrahedral gold clusters on thick films (≥ 10 ML) to two-dimensional planar structures on

thin films (≤ 3 ML). The interaction between excess charges, accumulated at the cluster/oxide interface with the metal substrate, underlies the stabilisation of a planar geometry for Au₂₀ clusters on thin MgO films. Additionally, the enhanced support-induced effects on thin-film-based catalysts lead to increasing of the binding strength of the reaction intermediates and/or adsorbed product molecules, and thus higher exit barriers. On thick films, 3D tetrahedral and bilayer structures are stable and charge accumulation and concomitant charging of adsorbed clusters can be induced by defect sites. For these measurements, direct adsorption of reactants on the catalysts plays an essential role on the reaction mechanisms.

- **CO-combustion on Pd_n:** Using various schemes of isotopically-labelled temperature programmed reaction experiments, three main reaction mechanisms (chemisorbed oxygen sites) are observed for CO oxidation over oxygen-treated palladium clusters (Pd₃₀ and Pd₁₃). In the α - and β -mechanism highly activated molecularly bound O₂ molecules are involved and CO₂ product molecules are formed at low (~ 200 K) and intermediate (~ 330 K) temperature regimes, respectively. Note that at these temperatures oxygen is not dissociated on bulk palladium and thus it could be valid for the clusters as well. The γ -mechanism occurs at higher temperature (~ 410 K) and presumably originates from dissociatively adsorbed oxygen at the surface or subsurface. At temperatures above ~ 550 K no reactivity is observed. This suggests that at these temperatures clusters and/or oxide-clusters on defect-poor magnesia films are either not stable or they agglomerate to form larger nanoparticles. Fourier transform infrared investigations reveal that stretching frequencies of adsorbed CO vary on metallic and pretreated (oxidised and reduced) clusters, indicating various adsorption sites on the different palladium catalysts. Oxidation and reduction cycles are reversible to high extent; however, the reduction does not completely recover the metallic state of clusters.

In the last chapter of this work, a novel microcalorimeter is introduced to measure heats of surface reaction and adsorption as well as cluster deposition processes. The thermally sensitive element of the sensor is a micromachined silicon cantilever onto which a 120 nm thick gold film is evaporated. The difference between the thermal expansion coefficients of silicon and gold layer, leads to the thermal bending of the sensor when heat exchanges with the cantilever. Based on obtained results, the minimum detectable power for the sensors is in the range of ~118 nW, which is sensitive enough to measure reactions heats ($\sim 200 \text{ kJ mol}^{-1}$).

Chapter 1

1. Introduction

In recent years, heterogeneous catalysts are more considered as small clusters of active materials, typically late transition metals, deposited on thin oxide films (TiO_2 , NiO , Al_2O_3 , MgO , Fe_2O_3 , and SiO_2). Clusters are intermediates between isolated atoms and bulk materials, and often possess specific properties unique to their nanoscale size, whose properties cannot be extrapolated through scaling arguments from knowledge of the bulk materials.¹⁻³ For modern heterogeneous catalysts, supported metal oxide films represent a convenient compromise between the atomically flat metal oxide single crystalline surfaces and industrial high surface area metal oxides. For the former support materials, very low electrical and thermal conductivities hinder the use of electron or ion spectroscopies as well as the accurate control of surface temperature. The industrial catalyst's supports are very complex materials consisting of wide size-distributed crystallites of various phases with often ill-defined surfaces. As a result, it is complicated to clearly identify the influence of the microscopic structure of the surface on the catalytic performance. However, these problems are much less critical for thin metal oxide films, where the small thickness of the oxide layer (1-100 nm) allows for a better heat transfer from the substrate to the oxide surface. Tunnelling of electrons from the underlying conductive substrate eliminates the charging problem accompanying the application of electron spectroscopies to many single crystalline oxide surfaces. Also, quantum chemical calculations become more and more powerful tools in understanding catalytic performance in the nanoscale cluster size regime. Thus, thin metal oxide based catalysts are very promising for future industrial applications. However, despite the great technological importance, little is known about the complex electronic mechanism, which governs the formation of the metal/oxide interface.

One of the principal goals of modern research in chemical catalysis is the development of methods for control and manipulation of the activity of catalytic systems. Control of the catalytic properties through the manipulation of particle size has been illustrated for a large range of different systems. Single crystal catalytic activity⁴ can be modified by reducing the size of the metal

nanoparticles with an average size on the nanometer scale.^{5,6} By reducing the size further to metal clusters with typically less than 100 atoms new emergent catalytic properties have been observed.⁷ In certain cases, the catalytic properties are altered by the pre-treatment of the catalyst.⁸⁻¹⁰ However, high temperature pre-treatments (in reduced or oxidised background) may also cause the collapse of the support and encapsulation of the active metals, their agglomeration as well as poisoning of the catalysts.^{11,12}

The following prominent factors are playing important roles in the efficiency of the cluster-based model catalysts.

1.1. Factors controlling the activity of cluster model catalysts

An intimate understanding of support effects on the catalytic properties of metal clusters is of great importance in designing supported size-selected cluster catalysts. The complexity of the metal/support interface, however, makes it difficult to obtain direct structural and electronic information even under ultrahigh vacuum conditions. Nevertheless, quantum mechanical models and theoretical description of cluster/oxide interactions provide an intuitive picture, which supports experimental observations and therefore, are widely used for a better understanding of this class of materials. For such planar model catalysts, the oxide support cannot be considered as a simple mechanical support for metal particles since catalyst/support interactions can control the morphology, modify the electronic properties and concomitantly, the reactivity and selectivity of the clusters and nanoparticles.¹³⁻¹⁶

Overall, the key factors that control the catalytic properties of cluster catalysts on surfaces can be classified into four different types:

- (i) **Nanocatalytic factors** are cluster intrinsic, including structural dynamical fluxionality, electronic size effects and impurity-doping effects.
- (ii) **Support-induced factors**, which are defects sites present on the support surface, charge transfer, effects related to variations in cluster morphology and appearance of new specific active sites at cluster/support perimeter interfaces.
- (iii) **Kinetic factors** such as the well-known spill-over and reverse spill-over.

- (iv) **Cooperative coadsorption factors** such as the influence of coadsorbates on the reactivity of the model catalyst. In this respect, cooperative effects either improve the catalytic performance, or hinder the reactant adsorption by blocking active sites, i.e. poisoning effects.

The next section focuses on the above-mentioned effects and reviews experimental and theoretical progresses in the exploration of the catalytic properties of supported size-selected metal clusters.

1.1.1. Nanocatalytic factors

Structural dynamical fluxionality. Defined as the propensity of small clusters to transform between various energetically accessible structural isomers to enhance the reaction rates in the course of chemical reactions. Hence, at a given temperature an ensemble of different isomers with very close lying energies are present. This complicates the determination of a discrete structure, but on the other hand is fundamental for catalytic activity as each isomer has its unique chemical reactivity. Additionally, the inter-conversion between various isomeric arrangements along the reaction coordinate enables the system to find the most favourable reaction energy pathway by choosing the most suited isomeric structure.

Electronic size effects: The features that make metal cluster-based catalysts so significant are the distinctive properties of the matter under spatial confinement. Finite systems are basically characterised by discrete electronic levels and size effects in terms of surface to volume ratio. In fact, the electronic structure is a function of the spatial arrangement of the atoms, which in turn depends on the ability of the resulting electronic bands to accommodate the outer electrons. The quantised electronic structure leads to a distinct odd-even alternation in the binding energy that has direct implications on the chemical reactivity toward adsorbate molecules.

In respect to supported clusters, electronic size effects play further important roles in the cluster/support interactions. Firstly, they influence the charge transfer and secondly, dynamics of the clusters (migration and coalescence) through their bonding character to the substrate.^{3,17} Hence, the evolution of the electronic properties with size is accompanied by dramatic changes in the

optical, chemical and magnetic behaviour of small particles with respect to bulk materials.¹⁸⁻²⁰

It is noteworthy that the study of cluster size effects in catalysis is complicated for a structure sensitive reaction, since the activity depends not only on the particle size (mainly through the amount of low coordinated sites) but also on the particle morphology, which has to be accurately determined.²¹

Impurity-doping effects: It has been realised that the intrinsic properties of materials, reduced to the cluster size regime (from a few to hundreds atoms) are non-scalable from their bulk analogues. In this size range, the electrical structure of clusters can be selectively altered as a function of size and by introducing suitable dopant atoms into clusters to enhance the catalytic performance of model catalysts.

In this regard, adding various alkali atoms (Li, Na,...) to the supported clusters with the purpose of donating one extra electron, may lead to an increased reactivity of the catalyst. For example, enhanced reactivity was measured by the addition of a sodium atom to the Au₂₀ clusters, thus attaining an electronic configuration similar to the more active anionic Au₂₀ clusters.²²

Experimental evidence of nano-catalytic factors: Figure 1.1 illustrates selected examples of temperature programmed reaction (TPR) results, obtained in our group subsequent to the ¹⁸O₂ and ¹³C¹⁶O exposure on the clean MgO(100) film, gold film, and various size-selected Au_n and Au_nSr clusters (1 ≤ n ≤ 9). Size-selected clusters were soft-landed onto well characterised MgO(100) thin films, which possessed a high concentration of surface oxygen vacancies (defect-rich film) that act as strong trapping sites for the clusters at low temperatures.^{23,24}

In these TPR spectra, only the production of the ¹³C¹⁶O¹⁸O isotopomer was detected, indicating that the oxidation of CO occurs only on the cluster and no oxygen from the MgO substrate is involved into the reaction. Furthermore, the evolution of size-dependent reactivity is clearly observed, as the smallest gold cluster that significantly catalyses the CO oxidation reaction is Au₈ (Fig. 1.1(b-d)). The inset figure shows that the onset for CO₂ formation on doped clusters is shifted to lower sizes (Au₃Sr) in comparison to the pure clusters (Au₈).

Interestingly, the doped Au_3Sr reveals reactivity at two temperatures, ~ 250 K and ~ 500 K, while Au_4 is inert. It is well known that gold is strongly electronegative thus, the mixing with the alkaline or alkaline earth metals, which leads to ionic alloys, can be a reason for observed reactivity (see below). Finally, the clean $\text{MgO}(100)$ surface (Fig. 1.1(a)) and multilayer gold film (Fig. 1.1(e)) are catalytically inert, the later reflecting the noble character of bulk gold.²⁵

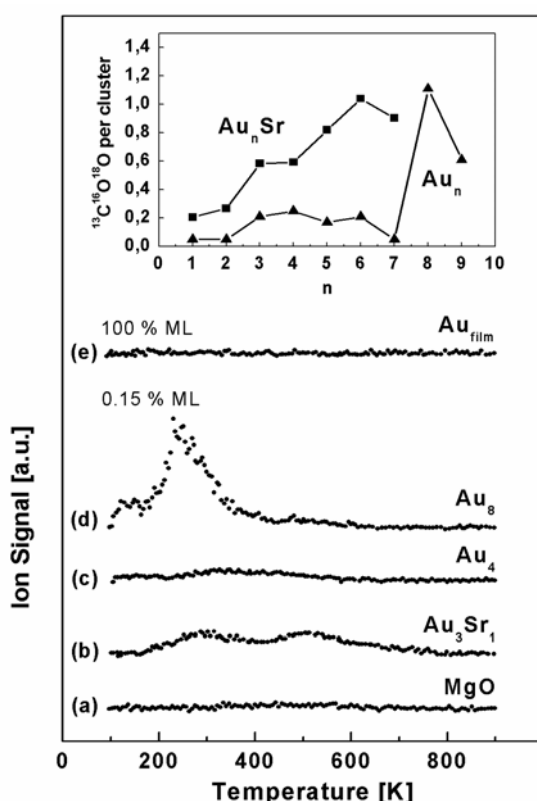


Fig. 1.1: TPR spectra of the CO_2 formation on: (a) an MgO film, (b) $\text{Au}_3\text{Sr}/\text{MgO}(\text{FC})$, (c) $\text{Au}_4/\text{MgO}(\text{FC})$, (d) $\text{Au}_8/\text{MgO}(\text{FC})$, and (e) a thick gold film grown on $\text{MgO}(100)$. The inset compares the chemical reactivity, R , of pure Au_n and doped Au_nSr clusters, with $1 \leq n \leq 9$, expressed by the number of product $^{13}\text{C}^{16}\text{O}^{18}\text{O}$ molecules per deposited cluster. The TPR spectra were recorded after exposure of the model catalyst to $^{18}\text{O}_2$ and $^{13}\text{C}^{16}\text{O}$ at ~ 90 K.

Theoretical evidence of nano-catalytic factors: To understand the origin of the observed nano-catalytic properties (dynamic structural fluxionality, electronic size effects and impurity-doping effects), the atomic structure and electronic spectra of the model catalysts were further studied by first-principles simulations.

The optimised structures for Au_8 , Au_4 , and Au_3Sr adsorbed on $\text{MgO}(\text{F}_{5c})$ are shown in Fig. 1.2, before (a-d) and after (e-h) O_2 adsorption. The **structural dynamical fluxionality** is nicely seen here by the different chemical properties of the two coexisting isomers for Au_8 clusters. A two-layered structure (Fig.

1.2(b)) is thermodynamically less stable (by 0.29 eV) than the quasi-planar structure (Fig. 1.2(a)), and showing a higher energy gain upon oxygen adsorption. Further dynamical adaptation of clusters is seen in Fig. 1.2(f), illustrating a large structural transformation upon O₂ adsorption in comparison to the Fig. 1.2(b). Such fluxionality is essential for the reaction to occur *via* the energetically optimal reaction pathway. Constraining the clusters to maintain its original geometry (Fig. 1.2(b)) prevents the adsorption and activation of O₂.

Based on *ab initio* calculations of local density of states (LDOS), strong **electronic size effects** in the binding and activation energy of oxygen by model catalyst was found. These key steps in the CO oxidation reaction depend on resonances formed between the electronic state of the cluster and the 2π* molecular state of oxygen. Figure 1.3(a) depicts the LDOS projected on the O₂ molecule that is adsorbed at the periphery site (Fig. 1.2(f)) of the more reactive isomer of the Au₈/MgO(F_{5c}) model catalyst. Upon interaction of oxygen with Au₈ cluster, the antibonding states are pulled below the Fermi level of the system, which in turn results in the occupation of electron in these antibonding states. The population of the antibonding states is accompanied by the activation of O₂, and a change in spin state of the molecule from triplet state in the gas-phase, to a peroxy-like one in the adsorbed state.

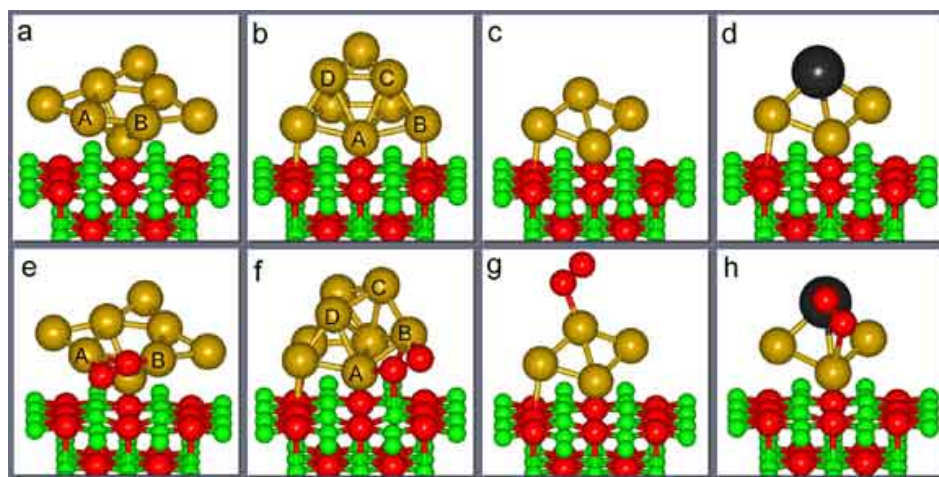


Fig. 1.2: The optimised atomic structures of model catalysts comprising Au₈ (a) and (b), Au₄ (c), and Au₃Sr (d) clusters adsorbed at an F-centre of an MgO(100) surface. The optimal geometries for the adsorption of O₂ molecule on these model catalysts are shown in panels (e) to (h).

A significantly different scenario, however, was found for the interaction of O₂ with the Au₄/MgO(F_{5c}) cluster, where molecular oxygen adsorbs in an “on-top” configuration, with one of the oxygen atoms binding to a single gold atom (Fig.

1.2(g)). Due to the narrow d-band of Au₄ clusters, and the location of the spin-down antibonding orbitals ($2\pi_{\parallel}^*$ and $2\pi_{\perp}^*$) above the Fermi level, the consequently small overlap between the electronic states, results in no activation and no change in the spin state of the oxygen molecule, upon interaction of O₂ with the Au₄ cluster (Fig. 1.3(c) and (d)).

Finally, enhancing the catalytic activity of a nanoclusters by the incorporation of an impurity (**impurity-doping effects**), is demonstrated here on Au₃Sr/MgO(F_{5c}) based catalyst. The LDOS spectra projected onto the oxygen molecule, the strontium (Sr) atom, and the Au₃ part of the metal cluster, are displayed in Fig. 1.3(e-g), respectively. Doping by a single impurity atom significantly changes the bonding and activation of O₂ compared to the pure gold tetramer. The bonding of O₂ is mainly to the Sr atom of the Au₃Sr cluster (Fig. 1.2(h)), and is characterised by a substantially higher adsorption energy (1.94 eV compared to 0.18 eV for the configuration shown in Fig. 1.2(g)). The activation of the O-O bond, reflected in an increased bond length of 1.37 Å is also observed. This activation is due to the occupation of the spin-down $2\pi_{\perp}^*$ oxygen orbital, resulting in a superoxo-like state of the adsorbate (in Fig. 1.3(e), this state contributes to the peak just above E_F). Bonding of the oxygen molecule to Au₃Sr/MgO(F_{5c}) occurs *via* resonances formed between the Sr states in the energy intervals 5 - 6 eV and 0 - 1 eV below E_F , with the spin-up $1\pi_{\parallel}$ and $2\pi_{\perp}^*$ states, as well as with the spin-down $1\pi_{\perp}$ and $2\pi_{\perp}^*$ orbitals, of the adsorbed activated oxygen molecule.

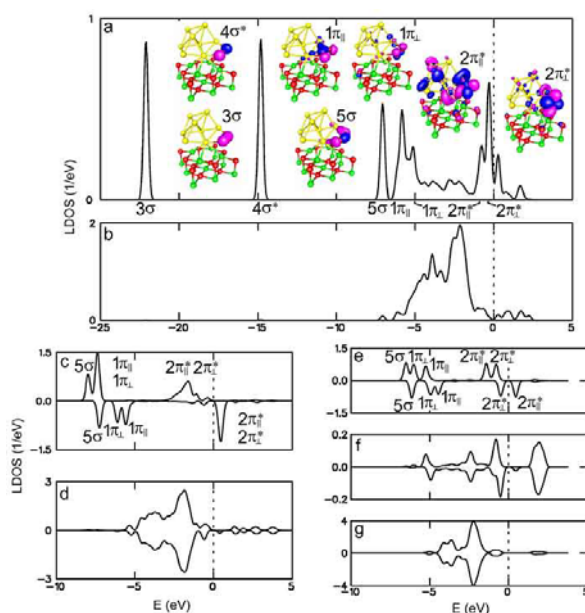


Fig. 1.3: Local density of spin-up and spin-down electronic states (LDOS) of the model catalysts shown in figure 1.2(f-h) for oxygen (a, c, e) and the metal part (b, d, f, g). The prominent peaks of the oxygen LDOS are labelled following the conventional nomenclature for the molecular orbitals of the gas-phase O₂ molecule, with \perp and \parallel meaning perpendicular and parallel to the MgO surface, respectively. The Fermi energy E_F is at 0 eV.

1.1.2. Support-induced factors

The choice of support material and the preparation method are particularly important for modern nanocatalysis. Oxides are often considered as the most promising support materials due to their ease of preparation, surface characterisation, and cleaning processes. Additionally, their large band gap keeps the characteristic electronic levels of the clusters at the surface to certain extent, intact.²⁶⁻³³

To address support-induced effects, I first focus on the intrinsic chemical activity of the oxide surfaces, which is largely dominated by the presence of **defect sites**. Possible surface defects can be classified in four major kinds of low-coordinated sites, divacancies, impurity atoms, and surface vacancies. The latter category includes cation vacancies (V-centres) as well as oxygen vacancies (F-centres). In a broader sense, an F-centre is defined as an electron trapped in an anion vacancy thus, it may act as an electron source for charge transfer reactions (see below).³⁴

Interesting results of *ab initio* theoretical studies have suggested that the metal atoms/support interaction energy can be significantly improved by the creation of appropriate surface vacancies. These vacancies on MgO film, namely F_s , F_s^+ , F_s^{2+} , V_s , V_s^- , V_s^{2-} sites, used in the models of acid or basic sites, correspond to the removal of O, O^- , O^{2-} , Mg, Mg^+ , Mg^{2+} atoms or ions from the surface, respectively. Surface vacancies appear to play an important role in the cluster/support binding nature. For instance, F_s^{2+} -centres exhibit a very high electron affinity, which ionises metal atoms upon interaction. In contrast, metal bonds are very weak on regular sites or neutral F_s -centres.

In our group, thin MgO films with well characterised density of oxygen vacancies have been routinely grown onto Mo(100). Usually, two types of films are selectively prepared: defect-poor and defect-rich. The latter films are grown with higher Mg evaporation rates compared to the defect-poor films and therefore contain more oxygen vacancies (see chapter 3).

Also, in joint experimental and theoretical investigations (described in § 1.1.1), a significant increase in the binding of various size-selected gold clusters to the surface F-centres was found. These results correlate fairly well with the observed thermal stability and activity of the supported clusters. Interestingly,

the same clusters adsorbed on an MgO defect-free surface are catalytically inactive for CO combustion.^{2,25}

Contrary to F-centres, V-centres are electron-deficient sites with different properties. For instance, metal atoms on neutral V_s tend to form a cation and replace the missing Mg ion in the lattice with a large gain in the electrostatic energy. On the other hand, no charge transfer between metal atoms and electronically saturated V_s^{-2} sites is observed. In this case bond strength is governed by the metal polarisability.³⁵

Next issue associated to the support-induced properties is the **charge transfer effects**. The cluster-charging propensity of deposited clusters on defect-free and defect-rich films was studied both experimentally and theoretically by examining the vibrational properties of adsorbed CO molecules on clusters. The internal CO stretch frequency $\nu(\text{CO})$, measured in the presence of coadsorbed O_2 for the $\text{Au}_8/\text{MgO}_{\text{defect-rich}}$ system shifted to lower frequency, by 25-50 cm^{-1} compared to the $\nu(\text{CO})$ frequency recorded for the $\text{Au}_8/\text{MgO}_{\text{defect-poor}}$ system. Systematic *ab initio* calculations^{2,25} revealed that this shift was caused by enhanced back-donation from the gold nanocluster into the antibonding $2\pi^*$ orbital of the CO adsorbed on the cluster anchored to a surface F-centre. In addition, calculations addressing free $\text{Au}_8/\text{O}_2/\text{CO}$ coadsorption complexes provided further evidence that the bonding characteristics and spectral shifts are interrelated, and sensitive to the charge state of the cluster. Consequently, cluster/surface interactions are accompanied by charge transfer from substrate into the adsorbed clusters. This correlates with variations in the population of antibonding states. For the aforementioned model catalysts, a net charge of 0.5e, 0.3e and 0.3e was found to transfer into adsorbed Au_8 , Au_4 and Au_3Sr clusters, respectively (Fig. 1.2). The activity, observed at ~140 K and ~280 K (Fig. 1.1(d)) was attributed to the charging of clusters *via* electron transfer from the surface and oxygen vacant F-centre defects.

The tunnelling of electron density from the underlying metal substrate has been observed on various surfaces.³³ In this context, a question may arise regarding the occurrence of the opposite mechanism, namely, the charge transfer to the substrate from adsorbed atoms. It was shown based on DFT calculations that the charge transfer could also occur in the opposite direction by the adsorption of electropositive atoms into metal supported oxide films.³⁶ Earlier studies on

single crystal oxide surfaces have already shown that the bonding of the metal adsorbate to oxygen causes charge transfer to the substrate.³⁷⁻³⁹

It is worthy to note that changes in the work function of the metal substrate induced by thin oxide films are of great importance in determining the charge transfer mechanisms. Accordingly, experimental results and theoretical studies have reported a significant increase or decrease of the work function depending on the nature of the grown films. For instance, a reduction in the work function was found for insulators ($\text{Al}_2\text{O}_3/\text{Mo}(110)$)⁴⁰, ionic oxides ($\text{MgO}/\text{Pd}(100)$, $\text{MgO}/\text{Mo}(100)$)^{41,42}, and alkali chlorides (alkali chloride thin films on $\text{Au}(111)$ and $\text{Ag}(100)$)^{43,44}, whereas oxide films such as $\text{SiO}_2/\text{Mo}(112)$ and $\text{TiO}_2/\text{Mo}(100)$ led to an increase of the work function by pronounced charge transfer.⁴²

In the following, effects of the support on **cluster morphology** will be introduced. The shape of nanoparticles is essential for the adsorption/desorption of reactants/products and therefore their catalytic properties, as it determines to a great extent which crystallographic planes are exposed to the reactants. For supported nanoparticles, it is not so trivial to distinguish between size and morphology effects. In particular, for smaller clusters (< 5 nm) the influence of low-coordinated atoms (e.g., atoms at edge and corner sites) in the reactivity of the model catalysts are more pronounced compared to larger particles (> 10 nm).⁴⁵ These low-coordinated sites have different electronic properties that generally induce higher binding energies and lower dissociation barriers for the adsorbed molecules. Particle shape characterisation is feasible on planar model catalysts (e.g., using TEM studies), but remains very difficult on industrial catalysts.^{20,21}

In addition, the complex structure of the metal/support interface is a function of the metal nanoparticle shape and configuration. Thus, it is plausible that one expects a stronger influence from the support on the catalytic properties of planar two-dimensional (2D) clusters rather than three-dimensional (3D). Obviously, the shape of the supported clusters (2D or 3D) depends on the strength of the cluster/support interaction and cluster size.⁴⁶⁻⁴⁸ In many cases both geometries are stable, and there is a marked energy barrier between them. The density functional approach has demonstrated that for copper clusters in $\text{Cu}_n/\text{MgO}(001)$ systems ($5 < n \leq 13$), the 3D configuration is preferred to the 2D structure. These observations are in line with the study of square planar Ni_4 and

Cu₄ clusters over cationic and anionic sites of regular MgO(100) surface. Indeed, the metal/metal bond in the cluster prevails over metal/oxygen bond, which correlates directly with the nature of the metal cluster. For instance, Ni/support interaction is stronger than the Cu/support interaction due to the presence of an incomplete 3*d* shell in Ni. In fact, the mixing of the 3*d* orbitals with the O(2*p*) band leads to the formation of a covalent polar bond of moderate strength, where Cu binds mainly *via* its 4*s* electrons and therefore, the interaction is weaker. Results of these calculations suggest that on MgO surfaces Cu and in particular Ni particles preferentially grow in a three-dimensional fashion.⁴⁹

Another very important approach in planar model catalysis is the possibility to control and tune some of the above-mentioned properties (e.g., the cluster geometry and dimensionality, adsorption energies and diffusion barriers, charge distributions, and chemical reactivities) through manipulation of the support thickness.^{9,50,51} It has been shown that on thin films (~1 nm) the strength of electrostatic interactions between the underlying metal substrate and the excess electronic charges (i.e., accumulated at the cluster/oxide interface) augments markedly with the number of clusters. As a consequence, the cluster adhesion energy (i.e., energy needed to separate the metal/oxide interface) increases with the charge penetrating the cluster from the substrate, which leads to a higher stability of planar cluster isomers. The origin of the dimensional crossover of the Au₂₀ clusters, from a 3D to 2D configuration, is attributed to the enhanced wettability resulting from the maximum contact between the cluster and the oxide surface. However, by increasing the thickness of the oxide films, electrostatic effects decrease and results resemble the observations obtained from bulk oxides.^{36,52,53} An interesting study, based on a low-temperature scanning tunnelling microscopy has been performed by Sterrer and co-workers, who have demonstrated a crossover from 3D to 2D geometry for gold nanostructures, deposited onto an Ag(001)-supported thin magnesia film (~3 ML).⁵⁴

It is obvious that the relative abundance of possible active sites on facets, at edges and corners between facets varies with cluster size. The key point for the high activity of nanoparticles has been interpreted in terms of the enhanced proportion of the low-coordinated sites at the cluster surfaces.^{15,55} More

interesting, however, is the situation at the **periphery of the cluster/support interface**, where special types of reaction sites appear only for clusters of certain sizes. The optimised reactivity at these special sites is ascribed to the additional attractive interactions between reaction intermediates and the substrate.

Various geometrical aspects of the CO oxidation over Au nanoparticles have been introduced by Molina *et al.*^{56,57}, and Remediakis *et al.*⁵⁸

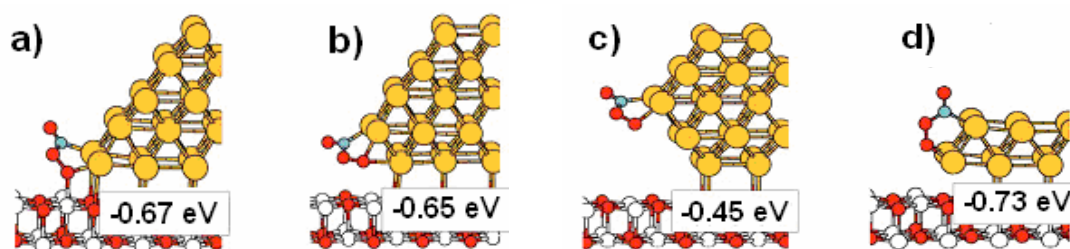


Fig 1.4: Illustrating CO-O₂ relaxed structures at different Au/MgO interfaces. For each cluster the corresponding revised potential barrier energy calculated with respect to CO(g) and O₂(g), is also given.⁵⁶

Figure 1.4 represents DFT results for different configurations of Au/MgO(100) interfaces during CO combustion reaction. The structure and relative stabilities of CO-O₂ complexes vary strongly with the structure of the interface. The potential energy of CO-O₂ intermediates is least for structures exhibited in figure 1.4(a), (b), and (d), which all are Au/oxide interface perimeter sites. Consequently, these sites are better for the binding of intermediates. In these geometries, the adsorbates locate at the proximity of the oxide surface (allowing for charge transfer stabilisation) and at the same time bind to the low-coordinated Au atoms in the cluster. At interface, (a), the steric repulsions between the CO-O₂ complex and substrate, forbid the complex to rotate around the edge to attain its most favourable orientation. Whereas for the second type of interface, (b) the lifting from the substrate by one Au layer of the low-coordinated atoms hampers undesirable CO/substrate interactions. For type (c) configuration (Au at edges) a larger CO-O₂/MgO distance leads to a sizable decrease in the stability of the intermediate and hence more negligible binding energy of the reactants. On the contrary, in the latter case (d), the slightly different geometry of Au edges contacted to the substrate results in a

weakening of the O₂/MgO interaction and hence, a lowering in the energy barriers of the complex formation. Altogether, reaction through type (b) species appears to be the most preferable reaction path.

1.1.3. Kinetic factors

In the previous sections, intrinsic support-related effects on the catalytic performance of size-selected cluster catalysts were presented. The next important issue regarding the reactivity of clusters is the **kinetic**. The nature and composition of the support material control the kinetics of adsorption as well as diffusion of the adsorbed species, which in turn determines the supply of reactants to the reaction centres of the catalyst.

In this respect, well-established phenomena such as spill-over and reverse spill-over are of great importance in the dynamics of nanocatalysis. The former phenomenon (spill-over) incorporates the diffusion of atomic or molecular intermediates from the catalyst to the support. In the latter case, adsorbed species on the support diffuse toward the catalyst. The area of the collection zone on the oxide close to the catalyst and concomitantly the reverse spill-over depends on the temperature, adsorption and diffusion of reactants, oxide material as well as cluster surface density (see § 3.2).

It has been shown experimentally that CO adsorbed within a collection zone can reversibly spill-over from the oxide over the cluster catalyst and thereby, increase the apparent CO flux. Thus, physisorbed CO on the oxide (MgO(100)) acts as a precursor state for chemisorption on supported Pd particles.^{59,60} The influence of the direct (from gas-phase) and indirect flux (diffusion from the support) on the reactivity of size-selected supported Pd clusters was shown by varying the cluster coverage independent of cluster size. At low temperatures and high cluster densities the collection zones may overlap, effectively resulting in smaller collection zones. Pulsed-molecular beam experiments revealed that the change in the reaction rate at two different cluster coverages is different for Pd₈ and Pd₃₀ clusters. For smaller clusters (Pd₈), evolution of the measured turn over frequencies, TOFs, is higher for low coverage sample. This is due to the enhanced indirect flux resulting from effective reverse spill-over. On the other hand, measured TOFs for the Pd₃₀ clusters are similar for both low and high coverages. However, the reaction probabilities for Pd₃₀ are strongly dependent on the cluster coverage, showing higher values for higher coverages. This

observation can be understood when assuming that direct and indirect flux do not have the same effect on the reaction. Indeed, for smaller Pd₈ clusters, the reaction probability of an impinging CO molecule is independent of whether it is supplied by diffusion or direct flux. In contrast, for larger clusters (Pd₃₀), a reduced reaction probability is found for CO supplied by reverse spill-over compared to the direct CO flux. Interestingly, modelling of the CO flux onto clusters using the capture zone model has also indicated that the effective reverse spill-over varies with cluster size.⁶¹

In section 3.2, kinetic simulation of the CO oxidation on Pd based catalysts will be introduced briefly for better understanding the effect of reverse spill-over in TPR experiments.

1.1.4. Cooperative coadsorption factors

Whilst the understanding of the adsorption properties of reactants (O₂, CO, H₂O, etc.) is important to gain knowledge of the catalytic activity of nanocatalysts, it is their coadsorption properties that may play a more important role.^{62,63} Several experimental studies have shown that the presence of trace moisture enhances CO conversion over supported gold catalyst (Au/TiO₂, Au/Al₂O₃ and Au/SiO₂) by four orders of magnitude.⁶⁴⁻⁶⁷

In particular, investigations on free gold cluster anions, Au_n⁻¹ (n ≤ 10), have demonstrated that in many cases a pre-adsorbate (O₂ or CO) augments the ability of clusters to bind an incoming molecule rather than lowering the probability of subsequent adsorption. The latter (CO) may cause poisoning when electron acceptor elements such as, chlorine are present.³¹ In another study, it has shown that near room temperature, the humid source produces abundant gold-hydroxy cluster anions (Au_nOH⁻) which reveal reversed oxygen adsorption activity. Non-reactive bare gold clusters become active when in the form Au_nOH⁻, while active bare clusters are inactive when -OH is bound. The high electron affinity of OH (~1.8 eV), makes the electron transfer from the even-n clusters to OH highly favourable and causes transfer from odd-n clusters to become stable. In this case, the electronic structure of gold clusters alters from the situation seen for bare clusters, i.e., the bare, odd-n Au_n⁻ clusters have no unpaired electrons, while the odd-n Au_nOH⁻ clusters now have an unpaired electron.⁶⁸

Moreover, first-principles quantum calculations have revealed a significant enhancement of the binding and activation of O₂, occurring upon coadsorption of oxygen and water on small Au clusters supported on defect-free MgO(100), as well as on gas-phase neutral clusters. The key point underlying the water-induced reactivity enhancement of gold clusters towards CO combustion is found to be the formation of a complex between the coadsorbed molecules. In such instances, the proton sharing results in hydroperoxyl-like (O₂...H₂O) intermediates. The activated O-O bond in the complex shows superoxo- or peroxy-like characteristics, and consequently the reaction with CO may occur readily between the adsorbed molecules with a relatively low barrier of ~0.5 eV.⁶⁹

1.2. Content of this thesis

In the course of this PhD thesis, the control and tunability of the reactivity of model nanocatalysts (supported size-selected metal clusters) are explored through temperature programmed reaction measurements as well as Fourier transform infrared spectroscopy in conjunction with first-principles theoretical calculations carried out by the U. Landman group. To this end, dependencies of the microscopic reaction mechanisms on the thickness of the MgO films, dimensionalities of adsorbed clusters, and oxygen pre-treatment of catalysts are demonstrated. Furthermore, the composition and stoichiometry of the oxide support material, MgO film grown onto a Mo(100) single crystal, is extensively investigated *in situ* using, Auger electron spectroscopy (AES), metastable helium impact electron spectroscopy (MIES), and ultraviolet photoelectron spectroscopy (UPS). The influence of kinetic factors on the CO oxidation reactions on surfaces are presented *via* a self-written code for temperature programmed studies. Finally, a new cantilever based micro-calorimeter is introduced for the measurement of the heat of adsorption and reaction.

Chapter 2

2. Experimental setup

To explore catalytic properties of the cluster based model catalysts, a state-of-the-art ultrahigh vacuum (UHV) apparatus, equipped with surface science methods was employed.⁷⁰ In this work, the model catalysts were prepared either by depositing size-selected metal clusters onto oxide films grown on metal substrates or by depositing size-selected clusters onto bimetallic-cantilevers.

The experiment consisted of: **a)** high vacuum chambers including a high frequency laser vaporisation cluster source; ion optics; a quadrupole bender and a mass selection unit, **b)** an analysis chamber with equipments to clean various metal substrates (an electron gun for thermal cleaning and an ion gun for sputtering), to synthesise various oxide films (a magnesium evaporator of in-house design, commercial e⁻-beam evaporator), and to characterise the model catalyst by means of spectroscopic techniques such as: Auger electron spectroscopy (AES), Fourier transform infrared spectroscopy (FTIR), metastable helium impact electron spectroscopy (MIES) and ultraviolet photoelectron spectroscopy (UPS) as well as temperature programmed reaction (TPR), molecular beam dosing (MBD) and pulsed-molecular beam reactive scattering (p-MBRS) experiments, **c)** a micro-calorimeter chamber to study heat of reaction/adsorption on the model catalysts, which consisted of micro-machined silicon cantilevers, a position sensitive detector (PSD) and a home-built pulsed valve.

Each part of the vacuum apparatus was pumped differentially with a turbo-molecular pump to maintain the pressure difference of more than 10 orders of magnitude between the cluster formation chamber (10^{-2} - 10^{-3} mbar) and the analysis or micro-calorimeter chambers (10^{-9} - 10^{-10} mbar). The analysis chamber was additionally pumped with an ion getter and titanium sublimation pump. This additional pumping was not used during the experiments, since the latter pump gives a Ti ion pulse when switched on. Furthermore, the analysis and source chambers were separated from the rest of the system through a gate valve. A 3D schematic of the whole apparatus is depicted in Fig. 2.1.

In the next sections the performance of the entire system as well as methods used for the characterisation of the model catalysts are described.

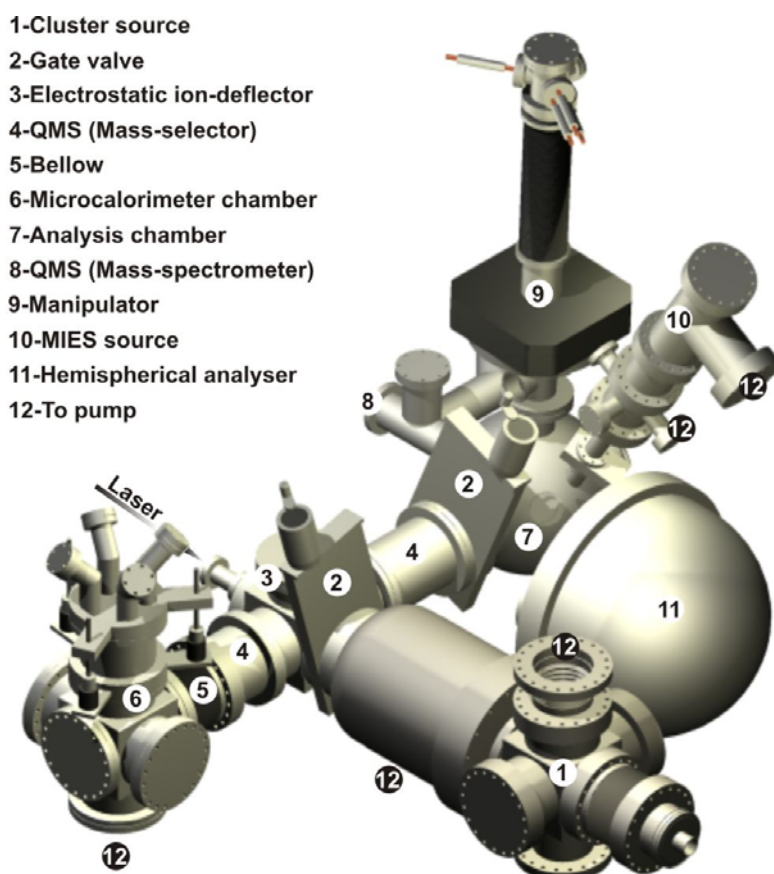


Fig. 2.1: Schematic 3D view of the UHV apparatus (see text).

2.1. Cluster source, ion optics and mass selector

Metal clusters (Pd or Au) were produced using a 120 Hz laser vaporisation source in which the 2nd harmonic of a Nd:YAG laser (*Innolas, Spitlight 600*) was focussed onto a rotating target. The resultant plasma was cooled by a helium pulse from a piezo-driven pulsed-valve. The clusters were formed upon the supersonic expansion of the metal-gas mixture through a nozzle.⁷⁰ Neutral and charged clusters were guided by a set of ion optics through differentially pumped vacuum chambers; positively charged clusters were deflected by a custom-made quadrupole bender and focused into the mass-selecting unit (*ABB-Extrel; mass limit 4000 amu*). Following a path through further sets of ion optics, the mass-selected clusters were soft-landed ($E_{kin} = \sim 0.2$ eV) onto

prepared oxide supports. Cation clusters were neutralised either by interaction with surface defects or *via* charge tunnelling through the support. The coverage of clusters was obtained from integration of the cluster current during deposition. Investigations of catalytic properties of the size-selected clusters on surfaces were carried out in the analysis or micro-calorimetric chambers.

The entire components of the optical path consisting of a skimmer, an octopole ion guide, pinholes, several stacks of Einzel-lenses, a quadrupole bender, a quadrupole mass-selection unit on each side, and a focussing octopole (FO) is depicted in Fig. 2.2.

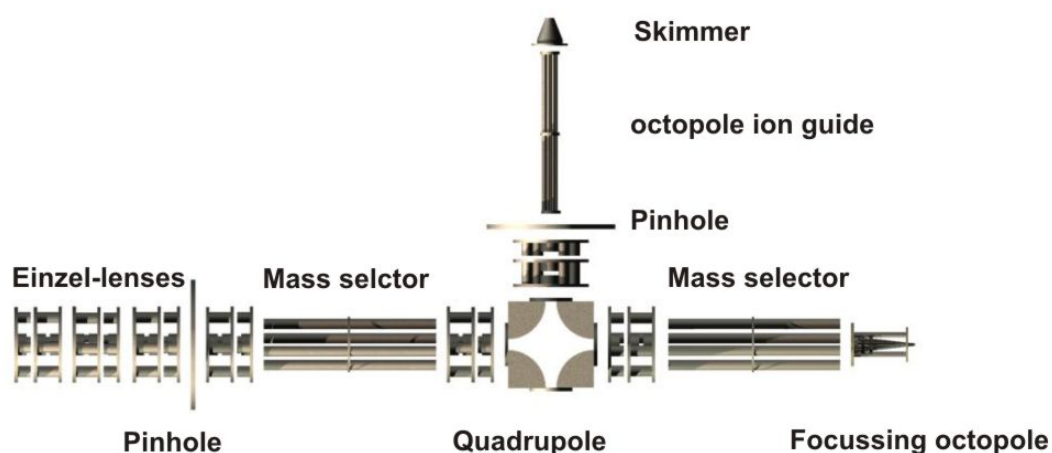


Fig. 2.2: Schematic 3D view of the ion optics including: a skimmer, an octopole ion guide, pinholes, Einzel-lenses, a quadrupole bender, mass selector units, and a focussing octopole.

Neutral species, which cannot be guided using the ion optics failed to negotiate the bender and were collected onto a quartz substrate. By inverting the polarity of the quadrupole, the cluster beam was selectively directed to the right (analysis chamber) or left (micro-calorimeter chamber) side of the UHV systems.

A conical focussing octopole, developed in our group⁷¹, was used as a final optical element in micro-calorimetric chamber to increase cluster density on the cantilever without increasing the deposition time by focusing the cluster beam for effective deposition onto the small cantilever area ($\sim 7.5 \times 10^{-2} \text{ mm}^2$). The focussing octopole was mounted onto a motorised bellow assembly allowing easy distance adjustment between the focussing octopole and the cantilever, which was particularly important for controlling the diameter of the cluster beam. Detailed information regarding the function of each component in the ion transport path see references.⁷²⁻⁷⁴

Representative mass spectra of gold and palladium clusters detected with the channeltron (*Burle channeltron*[®]) electron multiplier at room temperature are shown in Fig. 2.3(a) and (b), respectively. Inset in figure 2.3(a) illustrate larger mass distributions.

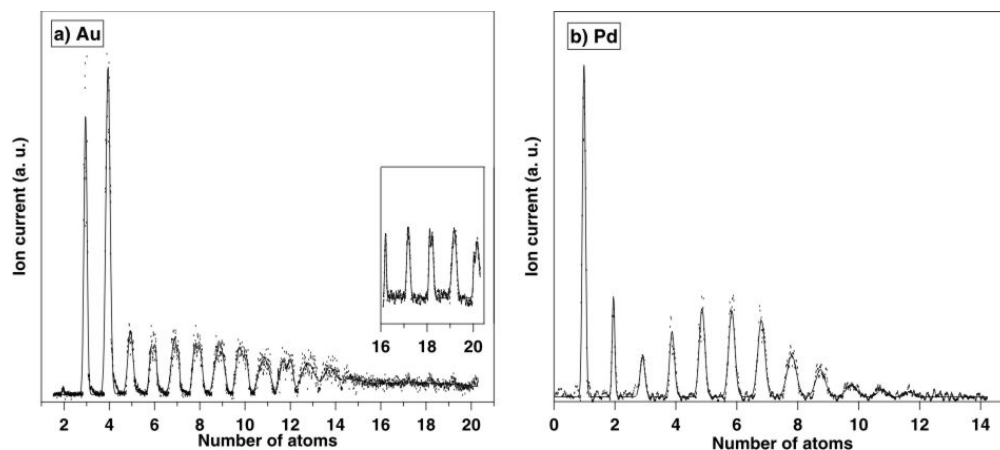


Fig. 2.3: Illustrating (a), gold and (b), palladium mass spectrum (clusters up to 14 atoms) recorded at room temperature. Inset shows larger clusters between 16 and 20 gold atoms.

2.2. Analysis chamber

The base pressure of the analysis chamber was usually maintained at $\sim 1 \times 10^{-10}$ mbar and the working pressure was $\sim 5 \times 10^{-10}$ mbar. The chamber was equipped with facilities to clean metal single crystals (§ 2.2.1), synthesise thin oxide films (§ 2.2.2), and characterise nano-assembled model catalysts (§ 2.2.3).

A very important element of this chamber was the crystal holder, since for all experiments the sample should be positioned in an optimal position. Three single crystals were attached to a liquid-nitrogen-cooled holder, which was mounted on a three dimensional translation stage with manual X-Y and motorised Z-axes. The rotation was achieved by a motorised, differentially-pumped rotary feedthrough.

Each crystal was held in place using Ta wires (D. 0.4 mm, purity 99%, *Goodfellow*) allowing computer-controlled resistive heating of the sample. The tantalum heating wires were spot-welded to two tantalum posts mounted on a stack of 5 copper disks interspaced with sapphire disks. The copper parts are in thermal contact with a liquid nitrogen reservoir. Effective nitrogen cooling of the

system prevents undesired thermal expansion from the heated sample to the metallic posts.

The temperature of the sample was monitored using a type C (W - 5% Re / W - 26% Re) thermocouple spot-welded to the edge of the crystals. Temperature could be accurately controlled using a proportional-integral-derivative (PID), controller (*RHK Technology, TM 310*) coupled to a programmable power supply (*HP-6032A*). The sample was resistively heated at a constant rate between ~ 100 and ~ 1200 K.

Figure 2.4(a) and (b) depict two different views into the analysis chamber including the crystal holder, QMS unit, beam doser, and Einzel-lenses of the ion optics.

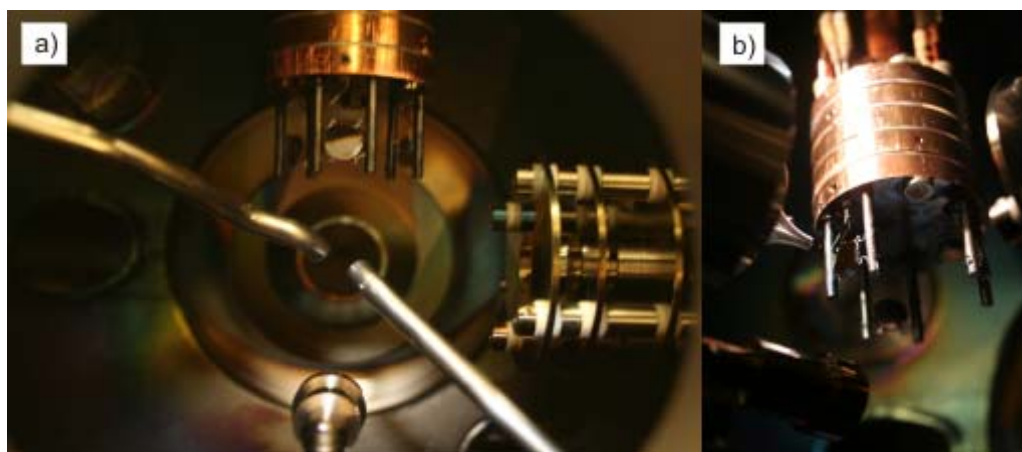


Fig. 2.4: Showing the inside of the analysis chamber. (a) Front view from QMS position; (b) side view including crystal holder in the middle, skimmer attached to the QMS unit and beam doser on the left-bottom and Einzel-lenses on the right.

2.2.1. Cleaning of metal single crystals

Metal single crystals were cleaned using an electron gun or an ion sputter gun depending on the melting point of the substrate. In the course of this work, mainly a home-built electron gun was used, since investigations were performed on a Mo(100) single crystal with a high melting temperature (~ 2896 K). The Mo(100) single crystal was chosen as a substrate because of the relative ease of cleaning, the small lattice mismatch with respect to the prepared MgO films, and the ability to thermally desorb the thin films from the surface.

The sample was heated up to ~ 2200 K *via* an electron beam from a Ta filament (D 0.3 mm, purity 99%, *Goodfellow*), which was placed behind the crystal, and

could be moved into operating position through the use of a linear drive. In operation, a voltage of typically ~3 kV (*Oltronixs* power supply) and a heating current up to ~40 mA was usually required.

For each experiment the substrate was cleaned and its composition was verified by Auger electron spectroscopy.

2.2.2. Synthesis of thin oxide films

Magnesium oxide and silicon/silicon oxide (Si/SiO₂) thin films (~10-15 ML) were produced employing two different types of evaporators. The magnesium, Mg, source of in-house design was made from the high purity Mg ribbon (W 3 mm, *Merck*) wrapped around a tantalum filament (D 0.3 mm, purity 99%, *Goodfellow*). To prevent deposition of magnesium onto the chamber's wall or other elements in the setup, a cylindrical metal shield was placed around the filament assembly. Typically, film growth was made at filament voltage around ~2.0-2.4 V and a current of ~1.3-1.6 A.

To prepare surfaces similar to the cantilever's material (p-doped silicon), an electron beam evaporator (*Tectra*) was used for depositing Si onto the Mo(100) single crystal in an oxygen atmosphere. Ejected electrons, usually provided from a coiled tungsten filament (~1000 kV, ~9 A) in the vicinity of the rod (p-doped Si rod, *Alfa Aesar*) or crucible (Mo), produce extremely high heating power that facilitate evaporation of any material in the temperature range ~400 to ~3100 K. Optimum growth conditions are described in § 3.1.

2.2.3. Characterisation methods

Standard spectroscopy methods were conducted at various stages of the catalytic reaction experiments to verify composition, adsorption sites, electronic structure and catalytic activity of the sample. Introduction to the principle of each technique is presented in the appendix A-C. All the measurements were carried out at ~100-120 K, otherwise it is mentioned.

Auger electron spectroscopy (AES)

The AES experiments were performed employing a 150 mm hemispherical analyser (VSW series) in fixed retarded ratio (FRR) mode and a HAC5000 analyser control unit, which was operated *via* an ESCA interface. A single channel electron multiplier was used to detect and amplify the electron signal

passing through the exit slit of the analyser. Further amplification was achieved with a lock-in amplifier (*ITHACO Dynatrac 391 A*), driven by an extra AC voltage applied to the crystal using a function generator (*HP 3310A*). Data was collected and digitised through the ESCA interface unit with home-written Lab-View programs.

Fourier transform infrared spectroscopy (FTIR)

IR radiation of a commercial FTIR spectrometer (*Thermo Nicolet 6700*) was focussed onto the crystal at grazing incidence with the use of an IR-compatible concave mirror. The radiation reflected from the crystal surface was detected with a liquid nitrogen-cooled mercury-cadmium-tellurium detector (*MCT-A, EG&G Optoelectronics*). The ^{13}CO carbonyl stretching frequency (probe molecule) was collected, using software provided by the company at a resolution of 4 cm^{-1} with 512 scans for both the reference (CO free surface) and the sample spectra.

A schematic view of the FTIR apparatus coupled to the analysis chamber is depicted in Fig. 2.5. Also shown are the additional components of the analysis chamber with the sample in the middle.

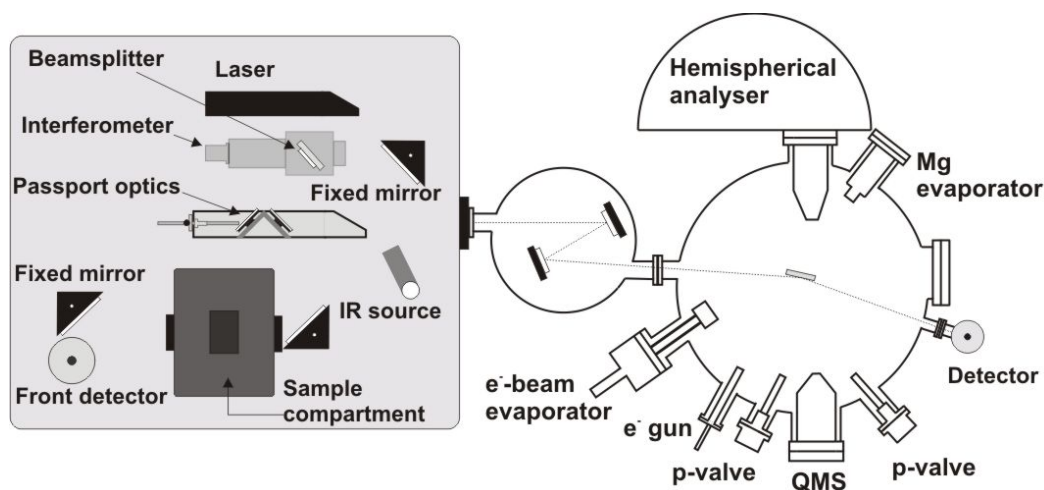


Fig. 2.5: Schematic view of the FTIR unit coupled to the analysis chamber. The IR path from the source up to the detector is depicted with a dotted line. Various elements of the analysis chamber including hemispherical analyser, Mg and e-beam evaporator, pulsed-valves as well as the e-gun are schematically illustrated.

Metastable He impact electron spectroscopy and ultraviolet photoelectron spectroscopy (MIES and UPS)

The same MIES/UPS source, originally built in the group of V. Kempter⁷⁵, was coupled to a hemispherical analyzer (VSW HA 150), and employed as a He^{*}/HeI source. The MIES/UPS spectra were measured simultaneously using a cold-cathode discharge source. The cold-cathode gas discharge source, adapted to the analysis chamber *via* a two-stage pumping systems, was separated using a gate valve.

As shown in Fig. 2.6, the MIES source consisted of: (i) two discharge regions denoted as the discharge chamber (~55 mbar) and the source chamber (10^{-4} to 10^{-5} mbar), and (ii) the high vacuum buffer-chamber (10^{-7} to 10^{-8} mbar) containing a mechanical chopper. Metastable He^{*} atoms and HeI photons were first generated in pure helium gas (~55 mbar, 99.996%) by glow discharge between a tungsten hollow cathode (~0.8 mm) and an anode that separate the two discharge regions. Following the expansion of the beam to the source chamber through the ~0.4 mm hole in the anode, the second discharge was ignited between the anode and the skimmer having a hole of ~0.8 millimetre in diameter. In the third region, a time-of-flight technique was integrated through the use of a mechanical chopper (~900 Hz) to separate discharge products, (He^{*}, $E^* = 19.8/20.6$ eV, MIES; HeI, $E^* = 21.2$ eV, UPS) and consequently, to select the electrons, emitted upon their interaction with the surface independently. In addition, two biased plates (deflector) were placed after the skimmer to remove the charged species from the beam. MIES and UPS spectra were recorded within ~400 s with a personal computer using a Lab-View program of in-house design. The angle of incidence for the mixed He^{*}/HeI beam was ~50° with respect to the surface normal.

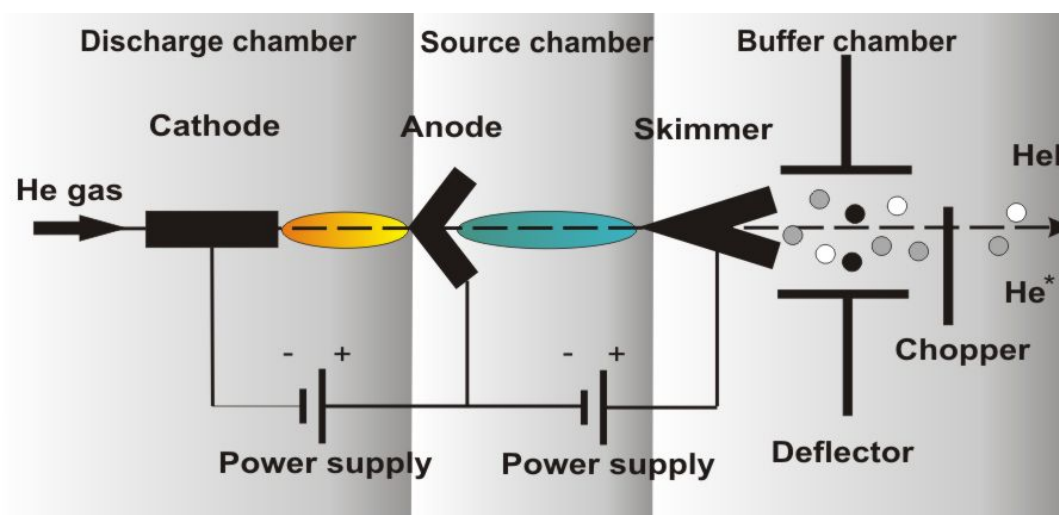


Fig. 2.6: Schematic view of the elements in MIES/UPS source (see text).

Temperature programmed reaction experiment (TPR)

To perform TPR experiments, a differentially pumped (60 L s^{-1}) quadrupole mass spectrometer (*Balzers QMG 421*) was used to detect the produced (desorbing) molecules on (from) the model catalyst, while the temperature of the sample was linearly increased at a constant rate ($\sim 2 \text{ K/s}$). The heating procedure was controlled by a feedback driven temperature controller (*RHK Technology, TM 310*) via a Lab-View computer program. An additional skimmer with a 3 mm orifice was mounted in front of the QMS housing to minimise spurious signals from the chamber background, walls, and also to selectively detect desorption products coming from the sample by positioning the crystal face $\sim 3 \text{ mm}$ away from the skimmer entrance. For monitoring the mass-to-charge ratios in TPR experiments the QMS and the sample were positioned in line-of-sight geometry.

When performing TPR, the skimmer can be floated at -150 V to prevent stray electrons impinging on the crystal, causing electron stimulated electron processes to occur. Up to 12 different masses can be simultaneously detected with the mass spectrometer. The ion current of each mass as a function of temperature, recorded directly with the spectrometer software (*Balzers, Quadstar 421 Version 2.0*), was obtained as a TPR spectrum.

Molecular beam doser and pulsed-molecular beam reactive scattering (MBD and p-MBRS)

The necessary elements to perform MBD / p-MBRS experiments in the UHV system are the QMS (used for both TPR and p-MBRS experiments), gas inlets (including a beam doser, pulsed-valve, and leak valve) and a gas handling system.⁷⁶ A micro-capillary array beam doser with a pinhole aperture made of stainless steel was employed for collimated exposures of the surface to gases. The beam doser also facilitated the quantitative measurements, since the flux of gas issuing from a pinhole can be precisely calibrated and kept constant over reaction time.

Alternatively, the model catalyst were be exposed to various reactants either through a leak valve (resulting in an isotropic pressure by filling the system with reactants) or *via* a pulsed piezo-electric valve.⁷¹ In the latter case, the optimum pulse duration and the driving voltage on the piezo-element, which controls the pulse opening, were determined individually for each experiment. Additional ~6 mm stainless steel tubing welded to the front part of the pulsed-valves was used to collimate the beam and to produce relatively high local pressures (mbar range). The length of the tubing was adjusted to be ~3 mm away from the sample surface.

The effective use of the molecular beam doser, leak valve and pulsed-valve requires a gas-handling system of appropriate design. Therefore, a bakeable stainless steel system consisting of a glass bulb, several valves, three pressure gauges (Pirani and Baratron®) and a turbo pump (60 L s^{-1}) were attached to the UHV system. Note that the Baratron® capacitance manometer measures true pressures and is insensitive to the type of the gas being measured. This is not valid for the Pirani and ion gauges.

2.2.4. Calibration of the pulsed-valves and molecular beam doser

Calibration of the pulsed-valves and molecular beam doser are essential for quantitative evaluation of the product molecules per incoming pulse/exposure of the reactant molecule. In order to calibrate the pulsed-valves, a test gas (such as CO) was admitted to the gas handling system with a backing pressure of several millibars. The valve to the ballast bulb with a known volume was then closed, and the remained gas in the line was evacuated. This volume (ballast

bulb with the gas line connectors) was measured from its weight and density of water at room temperature, $\sim 34.3 \text{ cm}^3$. Subsequently, the gas in the bulb expanded to the gas-line and built pressure was noted. Then the total volume of the gas-line (used for pulsed-valve experiments) was derived from the Boyle's law. Having amount of reduced pressure after certain pulses (e.g. 0.05 Torr, at 20 Hz for 15 minutes) and total volume of the gas line, the number of molecules per pulse ($\sim 3 \times 10^{14}$) was derived from ideal gas law. Simultaneously, measured QMS signal for a pulse of the test gas (CO), reflected from the molybdenum substrate was recorded (Fig. 2.7(a)). By integration (area) of QMS signal, the number of molecules per pulse and per area was evaluated for the test gas. This value can be used as a calibration factor for other reactant/product molecules.

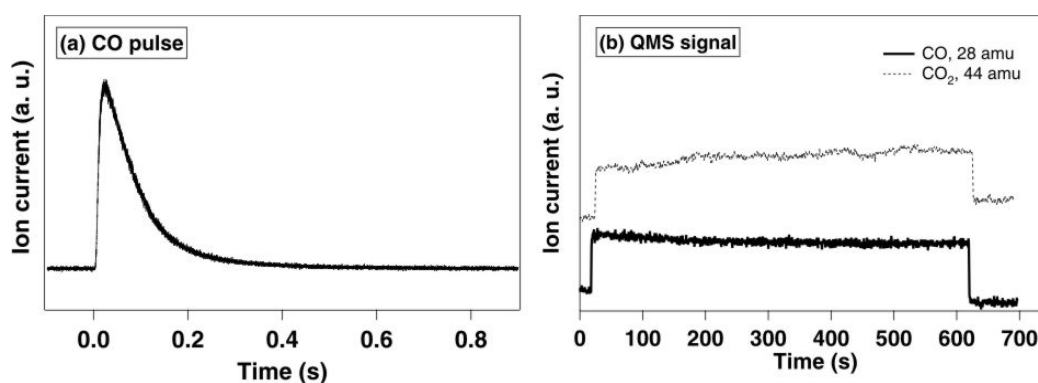


Fig. 2.7: Showing (a) detected CO molecules (28 amu) from a pulse of CO in front of a Mo substrate, (b) different masses 28 (solid line), 44 (dotted line) released from a MBD at constant flux. All spectra were recorded at room temperature.

Based on the earlier calibration results of our group, dependencies of the beam doser as a function of backing pressure, molar mass and exposure time is given by:⁷²

$$dN = 2.5 \times 10^{13} p \Delta t \frac{1}{\sqrt{M}} . \quad (1)$$

Additionally, the flux of gas molecules released from the MBD is directly proportional to the backing pressure p as expressed in the following relation:⁷⁷

$$F = \frac{p}{\sqrt{2\pi M k_B T}} , \quad (2)$$

where T is temperature, M and k_B are molar mass and Boltzmann constant, respectively. Therefore, by taking into account Eq. (1) and (2) a defined amount of reactant molecules can be dosed into the UHV system.

Note that for both types of calibration experiments a correction factor derived from the sensitivity of the mass spectrometer to products molecules with respect to the test gas should be considered. To this end, a defined value of product gas molecules was dosed through a molecular beam doser into UHV chamber and generated partial pressure was monitored with the mass spectrometer. Fig. 2.7(b) depicts the detected ion currents of CO (28 amu) and CO₂ (44 amu), released from a molecular beam doser at constant flux for a given time. Subsequently, the sensitivity factor was evaluated from the ratio of QMS signals (height-to-height intensity) for the test gas (CO) and given product molecules (CO₂).

2.3. Micro-calorimeter chamber

The micro-calorimetric chamber has been developed for a novel experimental approach to determine heats of adsorption and reaction on the cluster based catalysts. The chamber could be decoupled from the other UHV chambers by a motorised bellow assembly. When depositing clusters, the distance between focusing octopole (last optical element) and the sensor surface was adjusted horizontally *via* the bellow assembly. An additional vertical bellow assembly, combined with three over-pressured air suspension devices, provided vibrational damping. The cantilever was aligned with the axis of the cluster beam through positioning of the bellow assembly (shown in Fig. 2.8(a)). The UHV setup was equipped with **a**) the bimetallic cantilever array sensor mounted onto a piezoelectric-driven slider; **b**) the optical elements, including the position sensitive detector (*SiTek, 2L 45, 45 × 45 mm² active area*), probe and calibration diode lasers for detection and calibration of the cantilever bending, respectively. All the components were fixed onto a cryostatically copper holder. Furthermore, the sample gases were admitted into the chamber through a leak valve (*Varian Inc.*) and a pulsed piezo-electric valve, similar to those mounted in the analysis chambers. The arrangement of each element in the system can be seen in Fig. 2.8. The schematic and a picture of the inside view consisting of lasers,

cantilever array, position sensitive detector as well as focusing octopole is depicted in Fig. 2.8(b) and (c).

The base pressure of the chamber was $\sim 2 \times 10^{-9}$ mbar during the measurement. The chamber was evacuated by a 1000 L s⁻¹ turbo-molecular pump, backed with an oil-based rotary pump. The components of the system are described in detail in the following sections.

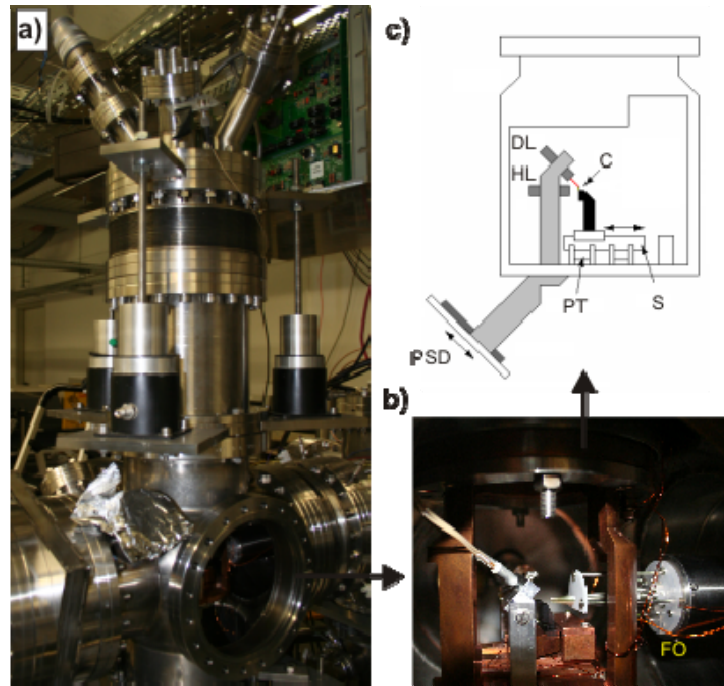


Fig. 2.8: Showing various parts of micro-calorimetric chamber; a) outside view of the chamber, b) and c) inside view and its schematic sketch both consisting of the focusing octopole (FO), heating laser (HL), detection laser (DL), slider (S), piezo-tubes (PT), position sensitive detector (PSD), and cantilever (C), respectively.

2.3.1. Cantilever array sensor

Preparation of bimetallic- cantilevers

The micro-fabricated array of eight p-doped silicon cantilevers (*Concentris, Type CLA-750-010-08, CLA-500-010-08*), onto which, a nanometer thick metal film was grown, act as the highly sensitive element for measuring the heat exchanges. Each cantilever has a length of 750 μm , a width of 100 μm , and a thickness of ~ 1 μm . The array was attached to an anodized aluminum holder, which in turn, was placed onto a trapezoidal copper support. All aluminum parts were anodised to reduce any parasitic reflection from the two laser beams used in the experiment.

In a separate high vacuum chamber (10^{-6} - 10^{-7} mbar), thin gold films were grown onto the cantilevers at ~ 320 K using an electron beam evaporator (*Tectra*). The evaporation rate ($\sim 0.4 \text{ \AA s}^{-1}$) and the thickness (~ 120 nm) of the films were controlled continuously with a flux monitor and a quartz microbalance during the film preparation. To increase the adhesion between gold and silicon, a 1 nm-thick chromium interlayer was first deposited onto the surface.⁷⁸

For the micro-calorimetric measurements the clusters were deposited onto the uncoated side of the silicon cantilever at room temperature with its natural oxide layer.

Piezoelectric inertial slider

For precisely positioning the cantilevers with respect to the detection laser, a two dimensional piezoelectric-driven inertial slider was employed. The trapezoidal copper support was placed onto three parallel multi-electrode piezo-tubes (*PI Ceramic*, OD 3.2 mm \times ID 2.2 mm \times L 12.7 mm), which in turn was glued at one end to the main body of the copper cryostat holder. These monolithic tubes contract laterally (radially) and longitudinally when a voltage was applied between their inner and outer electrodes. Thus, any axial contraction and radial displacement of the piezo-tube actuators will be adequate to move the copper support onto the three parallel sapphire rails, glued onto the bottom side of the support. This approach leads to simple *in situ* positioning of the sensor in two perpendicular directions (XY) under UHV conditions. A voltage ramp (rising time $\sim 500 \text{ \mu s}$, peak amplitude ~ 400 V) was applied using a home-made controller to deform the piezo elements and provide directional movement of the cantilever. Rapid movement of the piezo elements following the voltage ramp produces no further translation due to lack of inertia. The piezo elements driven at a frequency of 20 Hz, resulted in a translation rate of $\sim 1 \text{ \mu m s}^{-1}$.

2.3.2. Optical element

Optical detection device

Optical beam deflection technique is a common method for detecting the micro-cantilevers bending.⁷⁹ The output of a diode laser (*Shäfter+Kirchhoff, Model 57FCM, 670 nm, 1 mW full power*), coupled to the UHV chamber *via* an UHV

compatible single mode optical fiber (*Diamond GmbH*), was focused onto the metallic side of the cantilever. The tip of the fiber was positioned at a distance of ~ 5 mm from the cantilever array at an angle of 45° . The reflected light was then monitored using a PSD, located perpendicularly to the reflected beam at a distance of ~ 15 cm. The PSD could be positioned to ensure optimum detection of the reflected laser beam. Output currents from perpendicular edges of the PSD were converted into voltages U_1 and U_2 and amplified by electronics of in-house design. The sum of the two measured voltages, $U_1 + U_2$, (proportional to the intensity of the light detected by the PSD) and the difference voltage, $U_1 - U_2$, (proportional to the light intensity and to the geometric centre of the laser spot) were calculated. The spot position was evaluated by taking the quotient of the difference and the sum of U_1 and U_2 . The outputs from the PSD were digitised by an oscilloscope (*LeCroy, WaveRunner 6030, 350 MHz*) for measurements on the microsecond to millisecond timescale.

Calibration laser

Since every cantilever has a unique response (even when prepared at the same conditions) to a thermal load, it is necessary to calibrate the cantilever based heat sensors for each measurement. The calibration process was conducted by releasing a known heating power onto the cantilevers and determining consequent thermal bending of the micro-cantilevers through the displacement of the reflected laser spot on the PSD.^{80,81} To this end, a pulsed diode laser (*Lasiris PTM Serie, StockerYale Inc., 635 nm, 1 mW full power*) was used as a calibration laser with adjustable output power between 0 and $800 \mu\text{W}$. This laser was also coupled to the UHV chamber through an optical fiber, placed in front of the cantilever surface for uniformly heating the entire sensor area. Possible scattered light from the calibration laser that could be detected by the PSD, was removed by placing a long-pass filter (cut-off wavelength 665 nm, transmission $< 1\%$ at 635 nm) in front of the PSD. The response time of the micro-cantilever was taken from the time constant of the exponential fit of the recorded data. Temporal response of the cantilever to a pulsed thermal load measured on an oscilloscope is depicted in Fig. 2.9. Based on the unique cantilever properties, various response times between 0.5 and 2 ms in vacuum was obtained from exponential fit of cooling and heating periods (solid line in Fig. 2.9).

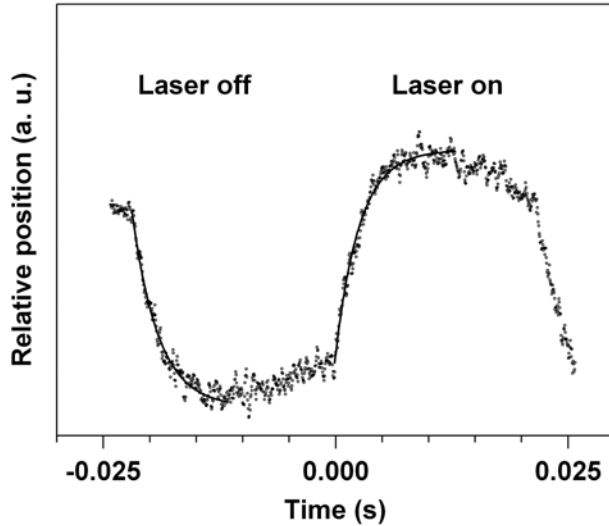


Fig. 2.9: Showing response of the micro-cantilever to the incident laser power modulated by a square wave. Markers illustrate data points and solid lines exponential fit of the cooling and heating periods.

Due to the divergence of the calibration laser ($\sim 10^\circ$ of conical aperture) and available minimum distance between laser head and cantilever surface (not smaller than ~ 5 mm), only a small part of the initial power could reach the cantilever. In order to determine the exact amount of the absorbed power on the bimetallic-cantilever the photon flux was normalised to the surface area of the cantilever. Taking the reflectivity of the metal films into account (95% for gold) a maximum power of $\sim 6 \mu\text{W}$ could be released onto the cantilevers under our experimental conditions. Finally, typical sensitivity for prepared bimetallic-cantilevers, which was calculated from the slope of the PSD signal as a function of the absorbed power, was found to be $8.5 \times 10^{-6} \text{ nW}^{-1}$. Other parameters influencing the sensitivity of cantilever e.g., metallic material, thickness of deposited layer, and the length of cantilever are discussed extensively in chapter 6.

Chapter 3

3. Preparation and characterisation of model catalysts

3.1. Preparation and characterisation of thin oxide films

Thin oxide films deposited onto metal substrates under ultrahigh vacuum have been recognised as very attractive systems in heterogeneous model catalysis. The motivation for studying metal clusters on thin oxide supports is manifold. Firstly, the oxide support reduces electronic coupling in comparison to metal or semiconductor surfaces; secondly, metal clusters on oxide surfaces provide a model system for industrial supported catalysts. In addition, films as thin as a few monolayers (ML) can be probed by electron spectroscopy without any difficulties associated to the surface charging. Note that most metal oxides are insulators or wide gap semiconductors, causing charge build-up during surface spectroscopic measurements, in which the probe particles are charged. This difficulty, however, is eliminated by making an ultrathin, well-defined, oxide film on the top of a metal substrate such that any charging induced during a charged particle measurement will dissipate into the conductive substrate. Another advantage of thin oxide films are their effective thermal conductivities that avoids any temperature gradient on the surface, during heating process (i.e. TPR experiments in our case). Many investigations have shown that these thin films exhibit roughly the same chemical and physical properties as their bulk analogues. In recent years, there have been ever growing studies for better understanding the metal/oxide interfaces, structural transformations in the growth process, electronic structure, and chemical properties of thin oxide films.^{20,32,75,82-89}

The electronic structure of ultrathin MgO films epitaxially grown on Mo(100) at conditions similar to the procedure used in this work were investigated by Schneider and co-workers. Results are presented in Fig. 3.1. The sharp (1×1) low energy electron diffraction (LEED) pattern of an MgO film after a short annealing is illustrated in Fig. 3.1(a). Multiple phonon losses in the high-resolution electron energy loss (HREELS) spectrum (Fig. 3.1(b)), ultraviolet photoelectron spectra (UPS) from the O(2p) valence band (Fig. 3.1(c)) and electron energy loss spectra (EELS) with the characteristic loss at about 6 eV

(Fig. 3.1(d)) indicate a well ordered MgO(100) single crystal surface in good agreement with other studies.²³

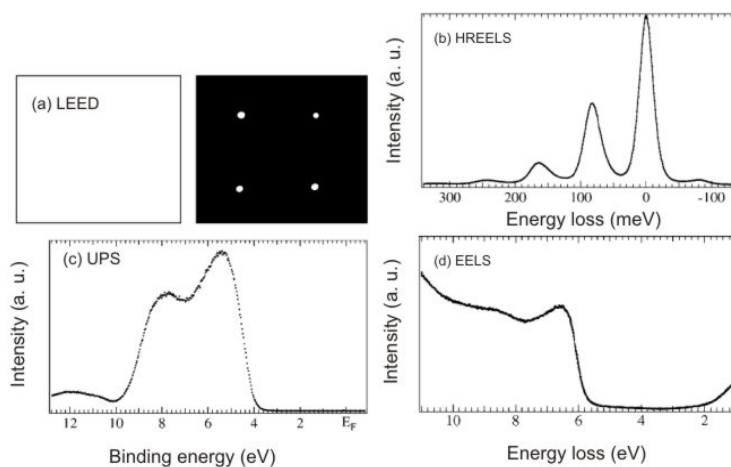


Figure 3.1: (a) LEED image ($E_p = 60$ eV) of the 20 ± 2 ML thick MgO(100) film showing a (1×1) square structure; (b) HREEL spectrum ($E_p = 3$ eV) and (c) UPS spectrum (He II) of the same MgO(100) film. The HREEL spectrum was recorded in specular geometry. All spectra were recorded at room temperature.²³

In this PhD thesis, thin oxide films with various compositions and thicknesses were synthesised on a Mo(100) single crystal. MgO(100) films were mainly prepared due to their rather simple structures (rocksalt lattice), relatively small lattice mismatch with respect to the underlying molybdenum substrate, and because they have been thoroughly characterised both experimentally and theoretically. The Mo(100) single crystal was used as a substrate because of experimental (practical) reasons. It could be resistively heated to ~ 1200 K and cooled to ~ 100 K. In addition, by means of an electron-beam heater, annealing up to ~ 2200 K was readily feasible.

In certain cases, SiO₂ films were prepared to explore the catalysis of the 1,3-butadiene hydrogenation on palladium clusters in a similar way that has been done in micro-calorimetric experiments (see chapter 6).

3.1.1. Preparation of MgO and SiO₂ thin films

Magnesium oxide thin films, used as a support for size-selected clusters, were prepared *in situ* for each experiment onto a clean Mo(100) single crystal under UHV conditions. The substrate was cleaned prior to the Mg evaporation by annealing to ~ 2000 K using an electron gun (to remove previous film and possible carbon and oxygen adsorbates from the surface). The growth

conditions were as follows: magnesium evaporation in a ¹⁶O₂ background (5×10^{-7} mbar) and at substrate temperature of ~ 300 K. Despite a 5.4% lattice mismatch between Mo(100) and MgO(100), it has been shown that at similar growth conditions MgO grows epitaxially on the Mo(100) substrate at temperatures between ~ 200 and ~ 600 K.⁸⁹

The film thickness and its composition were controlled by varying the evaporation time and Mg flux (evaporation rate) during the growth process. Earlier studies in our group revealed that the MgO films, synthesised under the optimum oxidation conditions, have essentially a one-to-one stoichiometry. Accordingly, the absence of a metallic magnesium (Mg⁰) desorption peak (~ 500 K) in thermal desorption spectrum (TDS experiment) was attributed to a fully oxidised film. Furthermore, MgO thin films have shown a relatively good thermal stability and did not decompose until ~ 1300 K.^{70,74} Moreover, the ratio between the magnesium and oxygen partial pressure was crucial to control defect concentrations (mainly F-centres) and the stoichiometry of the films.⁹⁰ Thus, films with higher defect density were grown at higher evaporation rates (~ 1.5 ML min⁻¹), whereas defect-poor films were created by slower evaporation rates (~ 0.1 ML min⁻¹). The oxygen background ($P_{\text{oxygen}} = 5 \times 10^{-7}$ mbar) and temperature of the substrate ($T_{\text{substrate}} = \sim 300$ K) were usually kept constant for oxide films synthesised in the present studies. As-grown MgO films were annealed to ~ 700 K for ~ 10 min to minimise defect density, ensure stoichiometry of the MgO surface and remove possible adsorbates or contaminations.

For better identification of the surface sites responsible for MgO reactivity, the combined experimental (TPD and FTIR) and theoretical study of the methanol interaction with defect-poor and defect-rich films have been carried out in our group previously.⁹¹ Obtained results have shown that the molecular chemisorption, activation and heterolytic dissociation occur on irregular sites (low-coordinated Mg-O pairs located at edges and steps). On defect-rich films, the O-H bond is selectively dissociated, resulting in desorption of H₂ at high temperature. Thus, these oxygen vacancy centres act as a nanocatalyst for certain reactions.⁹¹ The defect densities (F-centres) were estimated to be larger than 5×10^{13} cm⁻² through a NO-titration experiment. Assuming that one NO

molecule desorbs from each defect site, the measured amount of desorbed NO gives the defect density in temperature programmed desorption experiment.²

The composition, cleanliness, and surface defects of the grown films were characterised by common spectroscopic techniques such as Auger electron spectroscopy (AES), metastable helium impact electron spectroscopy (MIES) and ultraviolet photoelectron spectroscopy (UPS).

Note that the apparatus has recently been equipped with MIES/UPS source and the setup is still under development. Further modifications are being currently undertaken to achieve reproducible experimental conditions concerning the stability of He* beam and calibration of the analyser. The results, presented in this chapter must thus, be taken with care. However, they elucidate the performance of the setup and focus on the discussion of several optimisation factors for future experiments.

For the micro-calorimetric measurements, the clusters were deposited onto the uncoated side of the silicon cantilever. It should be noted that the silicon cantilever surface were oxidised (exposed to air) but this oxide layer has not been characterised in the following study. The investigations of ultrathin silicon dioxide films have shown that at room temperature and oxygen background pressure $< 1 \times 10^{-6}$ mbar, significant Si and SiO₂ are present in the films (SiO₂/Mo(110)) as evidenced by two major Auger features at 76 and 91 eV.⁹² Therefore, the evaporation was performed at ~300 K in a 5×10^{-7} mbar oxygen background for ~45 minutes. Post annealing for ~2 minutes at ~750 K was conducted to obtain slightly better stoichiometry.

In the following sections representative AES, MIES and UPS spectra of the synthesised thin films are demonstrated.

3.1.2. Characterisation of thin films

AES

The Auger electron shows characteristic peaks, which describes elemental compositions of the film and the underlying metal substrate depending on the film thickness. The Auger spectra were measured with primary beam energy of ~3 keV and a beam current of ~2.2 A. Fig. 3.2 exhibits a typical Auger spectrum of the Mo crystal after cleaning with an electron gun (~2000 K) for ~3 minutes prior to the MgO film growth. In the inset, the characteristic Auger peaks of

Molybdenum are labelled on the spectrum (96, 123, 148, 161, 186, 221, and 354 eV). Usually, the main impurities on the Mo (100) surfaces are carbon and oxygen.⁹³ In the collected Auger spectrum of the Mo(100) single crystal, an oxygen peak (~503 eV) but no carbon (~271 eV) and sulphur peaks (~152 eV) are present, which indicate the purity and cleanliness of the substrate. Cleaner Mo surfaces can be obtained when oxygen and annealing cycles are applied.

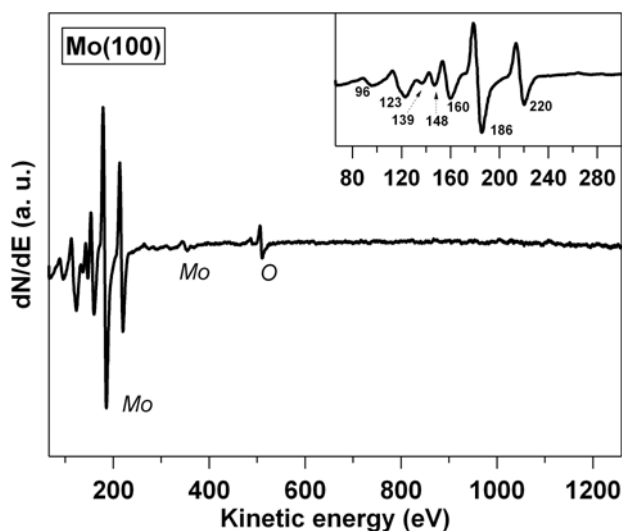


Fig. 3.2: Auger spectra of a clean Mo(100) single crystal, recorded at ~120 K, subsequent to the e⁻-gun annealing at ~2000 K. The inset spectrum shows the enlarged characteristic peaks of the molybdenum substrate.

As the chemical and catalytic properties of the cluster model catalysts varies depending on the composition and the thickness of oxide films, it is necessary to grow reproducible films at a given condition (see chapter 4). A common way to obtain the MgO film thickness is by determining the magnesium evaporation rate by combining AES and TPD measurements. The first break-point in a plot of Auger intensity, magnesium-to-molybdenum ratio, versus deposition time typically correlates to the completion of the first Mg monolayer (ML). Consequently, assuming the sticking probability of Mg atoms to the Mo(100) substrate is unity during the growth of the MgO films, the thickness of the films can be determined from the evaporation time using the calibrated Mg evaporation rate.^{89,90}

It is important to note that for MgO films grown at a relatively low oxygen pressure, the substrate Mo(MNN) Auger signals are less attenuated than that of the substrate covered with the stoichiometry MgO films. This implies that at low oxygen pressures, Mg deposition onto Mo(100) produces three-dimensional Mg and MgO islands.⁸⁹ The strong attenuation of the molybdenum Auger signals is seen by our AES observations for defect-poor films with increasing evaporation

time (Fig. 3.3). Therefore, the value obtained for Mo Auger peak (186 eV) in the break-point analysis using Mg/Mo ratio is erroneous.

Additionally, the MgO coverage can be determined by comparing the MgO Auger spectrum with a clean Mo surface, since decrease of the Mo peak is also directly related to the film thickness. Note that the spectrum of a clean Mo surface taken before Mg deposition cannot be used as a reference, because the Auger parameters vary with time. As a consequence, in our earlier studies the Auger spectrum of the back side of the crystal (clean Mo surface) was collected after each evaporation time. Having electron inelastic mean free path, λ , which is a function of the escaping electron energy, the thickness was obtained by the following relation:

$$\frac{I_{Mo,front}(t)}{I_{Mo,front}(t_0)} = \frac{I_{Mo,front}(t)}{I_{Mo'back}(t)*F} = \exp\left(\frac{R}{\lambda}*t\right) = \exp\left(-\frac{d(t)}{\lambda}\right),$$

where F is the correction factor obtained from the ratio of the Mo Auger intensities at the front and back side of the Mo substrate, R and $d(t)$ are the evaporation rate and film thickness, respectively.⁷⁴

The previously described procedure was used in our group to determine thickness of the prepared films. However, for the measurements presented in this work, the back side of the crystal was not accessible, as the crystal holder is different compared to the holder used in earlier studies. Consequently, to evaluate the coverage corresponding to the growth time, rough break-point analysis using Auger signals (peak-to-peak height) of Mg/Mo and Mg/O for each deposition time was made (see below).

To explore the composition and stoichiometry of the MgO films, various films at optimum growth conditions ($P_{oxygen} = 5 \times 10^{-7}$ mbar, $T_{substrate} = \sim 300$ K) were prepared at different evaporation times. Fig. 3.3 shows typical Auger spectra of as-grown defect-poor films (i.e. films prepared by low Mg evaporation rate) of different thicknesses, acquired at ~ 120 K. The evolution of magnesium (~ 1174 eV) and oxygen Auger peaks (~ 503 eV) is nicely seen as the thickness increases (Fig. 3.3 (a-e)). Magnesium peaks become more predominant and the substrate's molybdenum, Mo, peaks attenuate with the evaporation time ($\sim 1-2$ ML min^{-1}).

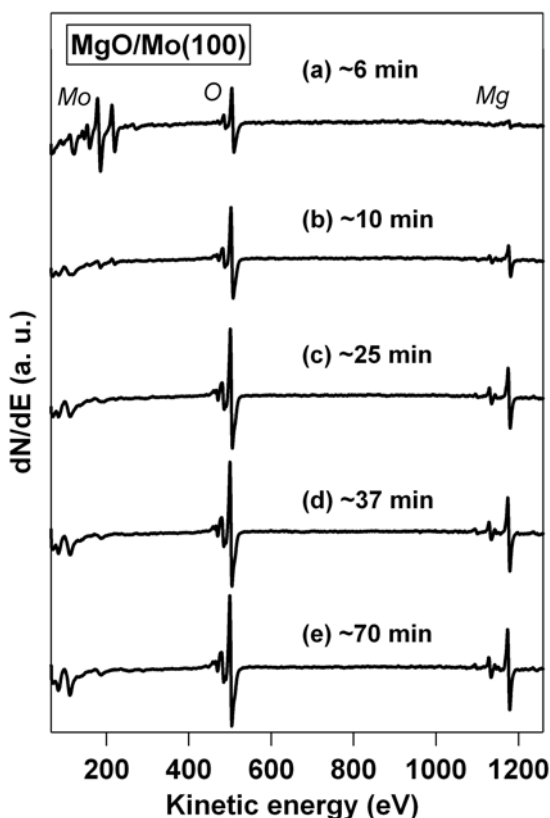


Fig. 3.3: Depicts Auger spectra of defect-poor MgO films at various evaporation times. Films were prepared by evaporating of Mg in a $^{16}\text{O}_2$ atmosphere (5×10^{-7} mbar) onto a Mo substrate at ~ 300 K. All spectra were recorded at ~ 120 K.

It was found that MgO films, grown at a very high magnesium flux or low oxygen pressures reveal metallic character as evidenced by AES.⁹³ This is also valid for films, which are prepared in the present work under similar conditions. Fig. 3.4(a) shows an MgO film, grown with very high Mg flux at ~ 300 K. A major Auger peak at (~ 1140 eV, ~ 1186 eV) indicates the presence of metallic magnesium on the surface. By annealing the same film at ~ 300 K in an oxygen atmosphere for ~ 2 minutes, a typical MgO Auger spectrum is obtained.

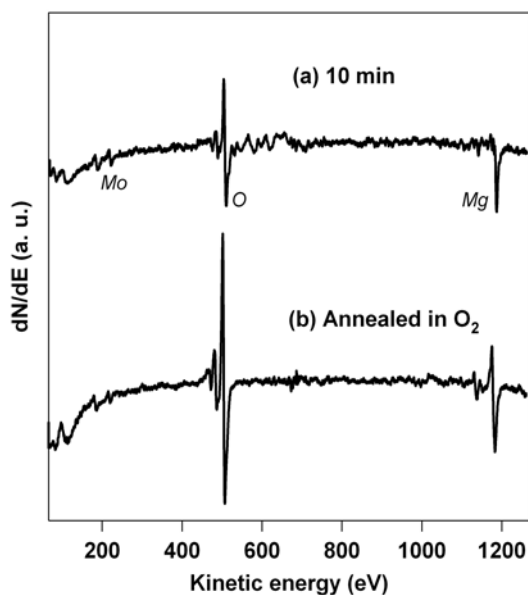


Fig. 3.4: Auger spectra of an MgO film grown at high Mg flux acquired at ~ 120 K. (a) As-grown film. (b) The same film annealed in a O_2 background at ~ 300 K. Note the evolution of ~ 1174 eV peak representative of a MgO film after annealing.

As mentioned in § 3.1.1, defect-rich MgO films were prepared at higher magnesium evaporation rates ($\sim 1.5 \text{ ML min}^{-1}$) compared to defect-poor films ($\sim 0.1 \text{ ML min}^{-1}$). These defective films mainly contain oxygen vacancies, which were characterised by EELS, FTIR, TDS, and NO/CO-titration experiments.^{23,24,70} The Auger spectra of defect-rich films at various evaporation times are depicted in Fig. 3.5. Application of MIES technique as an extremely surface sensitive method to characterise defects of (F-centres) the support material is one of our future prospects.^{88,94}

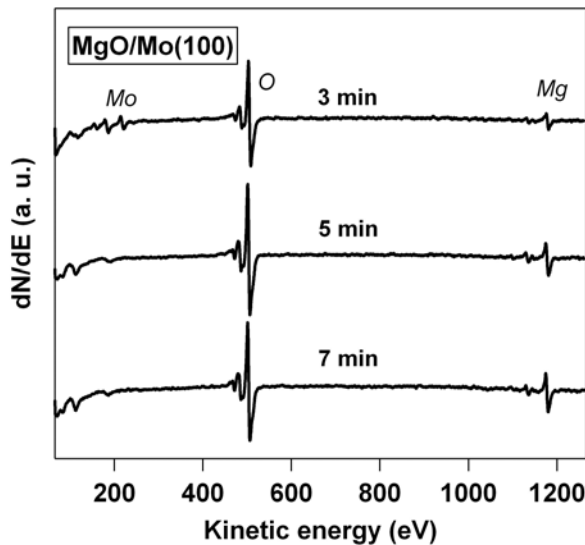


Fig. 3.5: Illustrating Auger spectra of defect-rich MgO films at various evaporation times, grown onto a Mo(100) single crystal at $\sim 300 \text{ K}$. No signature of metallic magnesium is present in the spectra.

As discussed, film thicknesses were obtained from the ratio of the Mg/O, and Mg/O Auger intensities as a function of evaporation time for defect-poor films (break-point analysis). In Fig. 3.6 and 3.7, the Mg/Mo and Mg/O ratio for various evaporation times are depicted, respectively. Although, the determination of the thickness in both cases is erroneous, the break-point is observed to occur at the same evaporation time. In the former case, the weak Mo Auger signal is a source of uncertainty, whereas for the Mg/O ratios the substrate contribution in the oxygen Auger intensity is unknown. As the ratio varies with the evaporation times of up to ~ 20 minutes, and then remains almost constant for longer evaporation times, a clear break-point, marked by an arrow, can be seen (by extrapolating linear fits). In the inset of Fig. 3.6, the variation of Mg (Δ) and Mo (\blacktriangledown) Auger intensities are shown. Fig. 3.7 (a) and (b) indicate the enlarged O and Mg peaks of a defect-poor film, used to determine the peak-to-peak height.

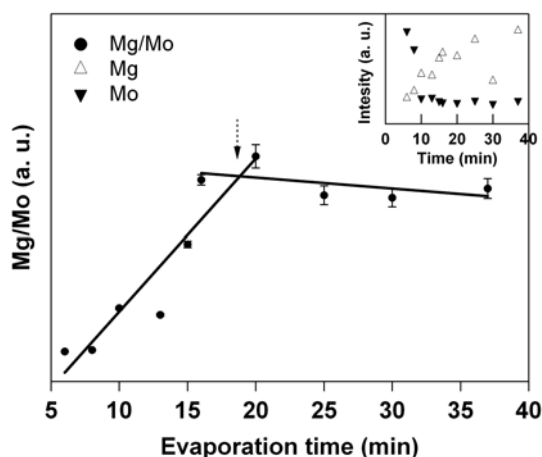


Fig. 3.6: Illustrating the evolution of the Mg/Mo Auger peak ratios as a function of evaporation time. Also shown are Mg (Δ) and Mo (∇) Auger peaks in the inset. Error bars were calculated from standard deviation of Mg/Mo ratios of four repeated film measurements.

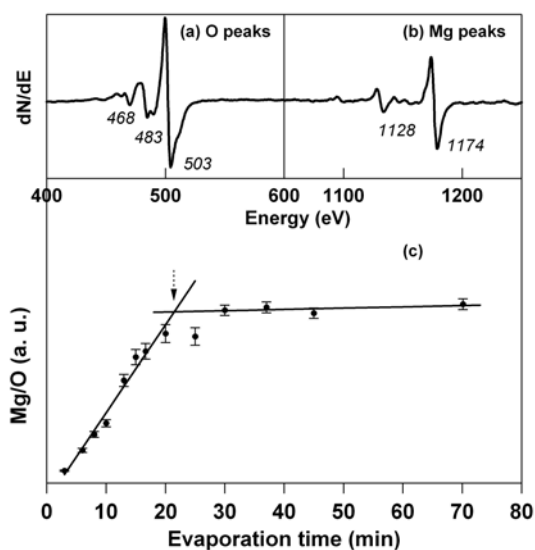


Fig. 3.7: Spectrum (a) and (b) depict enlarge O and Mg Auger peaks of a ~ 10 ML thick defect-poor MgO film, respectively. (c) Shows the evolution of the Mg/O Auger peak ratios as a function of evaporation time. Error bars were calculated from standard deviation of Mg/O ratios of four repeated film measurements.

These experimental findings reveal that MgO does not grow *via* a layer-by-layer growth mode but rather by island formation, where the inter-islands Mo surface regions contribute to the Auger oxygen peak. A constant Mg/O Auger peak ratio at higher coverages is assigned to the closed stoichiometric MgO films. By taking into account earlier studies and recent AES measurements, the break-point is attributed to a closed film with the MgO islands up to ~ 3 ML thick. The growth of the MgO films by the formation of the small islands of various thicknesses is consistent with recent scanning tunnelling microscopy (STM) and atomic force microscopy (AFM) studies carried out in our group for the growth of the MgO films on a silver single crystal⁹⁵ as well as with other similar studies.^{82,83}

In the following, properties of silicon dioxide films are addressed. As silicon (Si), and silicon dioxide (SiO_2) species can be easily differentiated based on their characteristic Auger transition energies, it is feasible to synthesise a film

containing both elements (Si, SiO₂). Silicon has a major Si (LVV) peak at 91 eV, whereas SiO₂ has Auger peaks at 76, 63, and 59 eV. In the Auger spectrum of SiO₂ film, Si (large peak at 91 eV) and SiO₂ (63 eV) as well as oxygen peaks are observed (Fig. 3.8).

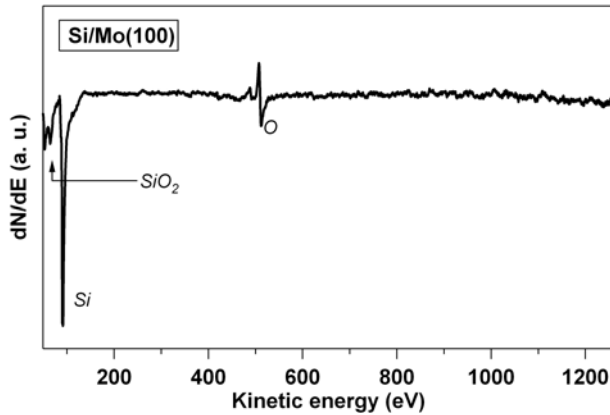


Fig. 3.8: Showing Auger spectrum of a Si/SiO₂ film, grown onto a Mo(100) single crystal at ~300 K in a 5×10^{-7} mbar oxygen background.

MIES/UPS

The spectra presented here were recorded at ~120 K on the annealed samples (10 min at ~700 K). To enhance the detection efficiency near zero kinetic energy, during all measurements the sample was biased to ~20 V with respect to the ground. This prevents the detection of low energy electrons present in the chamber (ion gauge). This procedure also permits a more precise determination of the work function (WF) of metals and WF changes. Additionally, it has been shown that shift of the spectra by a constant amount energy has no influence on the MIES/UPS spectra.^{75,96}

Conventionally, the binding energies in the spectra are referenced to the Fermi level, E_F , of the metallic substrate, as depicted in Fig. 3.9. Experimentally, the E_F is a fixed point on the energy scale and corresponds to the maximum kinetic energy at which electrons can be measured with MIES and UPS from a metallic substrate. Since the substrate and the analyser are in electrical contact, E_F appears at the same kinetic energy, irrespective from substrate work function. Thus, presenting the spectra with a binding energy scale, with E_F as origin, allows the change of the work function (due to, for example, adsorption or charging) to be determined from the shift of the high-energy cut-off of the spectra.⁹⁷

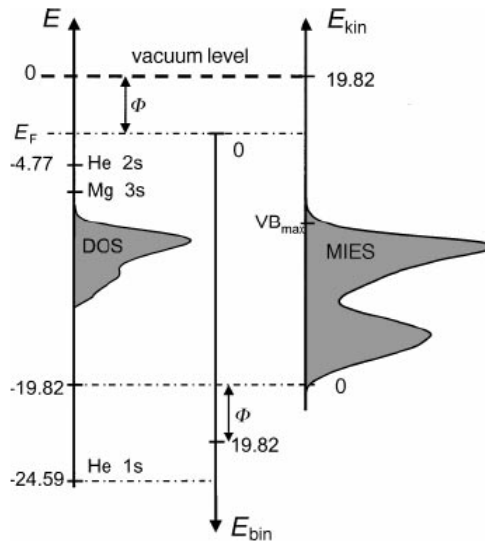


Fig. 3.9: Energy diagram for a He* probe atom in front of a surface of insulator. Left side: energy levels of the isolated He and Mg atoms and surface density of states in the valance band. Also shown is the position of the Fermi level in the insulator band gap; Φ is the work function of the surface. Middle: binding energies, $E_{bin} = E_F - E$, of electrons involved in the Auger de-excitation process are usually presented with respect to this axis, which has its origin at E_F . Right side: schematic of the experimental spectrum of kinetic energies of the electrons emitted in the AD process. Zero kinetic energy corresponds to a binding energy of 19.82 eV with respect to the vacuum level (or $(19.8 - \Phi)$ eV) with respect to E_F .⁹⁷

In addition, the absolute value of the work function i.e., the distance between E_F and vacuum level can be derived from the energetic distance between the spectra cut-off at large binding energies and the point on the energy scale that equals the excitation energy of the probe atoms (19.8 and 21.2 eV, for MIES and UPS, respectively). For the metal supported insulators (oxide films), this is true when the Fermi level of the metal substrate is known and the system is calibrated for E_F . Otherwise, for insulators the Fermi energy lies in the band gap and as discussed the interpretation of the electronic spectra is more involved. Unfortunately, in our setup the Fermi energy of the Mo substrate has not been measured yet and thus, the calibration of the spectrometer is missing. This is an important issue, which makes WF determination ambiguous.

Considering aforementioned points, another issue in our experiments is the improper electrical contacts between the sample and analyser. As shown in figure 3.10(a) the MIES electrons, vs. measured kinetic energies, (-20 V biased was corrected) of an $\text{MgO}_{\text{defect-poor}}$ film (~6 ML) begins at negative energies (with a ~-4 eV offset relative to the zero point). The offset is attributed to the position of the E_F (band gap). Moreover, the discrepancy in the position of the O(2p)

feature (originated from the ionisation of MgO valence band (VB) states in an Auger de-excitation process) at higher energies (~8-12 eV) from literature values is due to experimental errors. Therefore, all the spectra were shifted to the literature values since the spectrometer was not calibrated for these measurements (Fig. 3.10(b)).^{97,98}

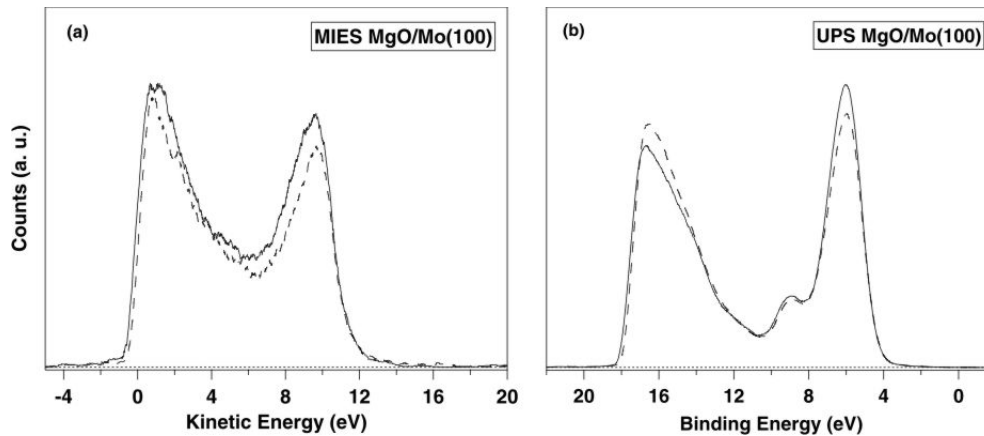


Fig. 3.10: (a) and (b) showing MIES and UPS spectra of an MgO film (~6 ML) deposited onto a Mo(100) single crystal, respectively. Dashed lines are spectra recorded with a film of the same thickness, synthesised at a different day.

Simultaneously, the reproducibility of the measured spectra of the MgO films with equal thicknesses, prepared at different days is also shown (solid and dashed lines).

A question may arise about the size and position of the metastable beam on the sample surface. The optimum position was first determined through rough adjustment using geometrical parameters (the sample position with respect to the the analyser slit). Subsequently, the final configuration was obtained by the fine positioning of the crystal holder in order to detect the best spectrum. In this context, to define accuracy of the measurements, both MIES and AES spectra of a defect-poor MgO film (~10 ML) and the oxidised molybdenum substrate ($P_{\text{oxygen}} = 5 \times 10^{-7}$ mbar, $T = 15$ minutes) are recorded for each sample. In the collected MIES spectra (Fig. 3.11(a)), the O(2p) feature is significantly attenuated for Mo-oxide. This is also in consistent with corresponding AES spectra (Fig. 3.11(b)), which indicate no Mg peak on the oxidised substrate.

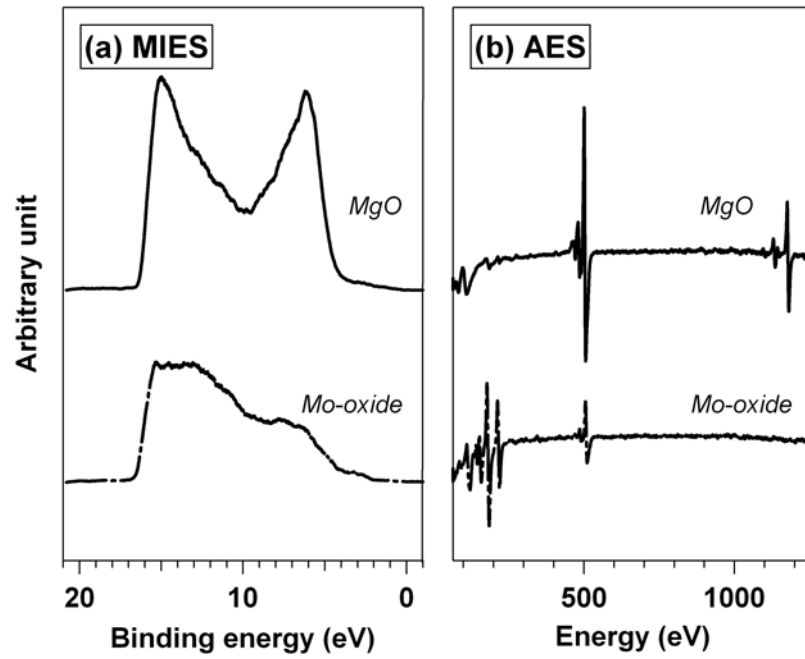


Fig. 3.11: Showing (a) MIES and (b) AES spectra of a defect-poor MgO film (~10 ML). Data were collected at ~120 K.

Considering the energy diagram of a metallic probe with respect to the spectrometer (Fig. 3.12), the work function of the sample can be derived from the width of the UPS spectrum, using following relations⁹⁹:

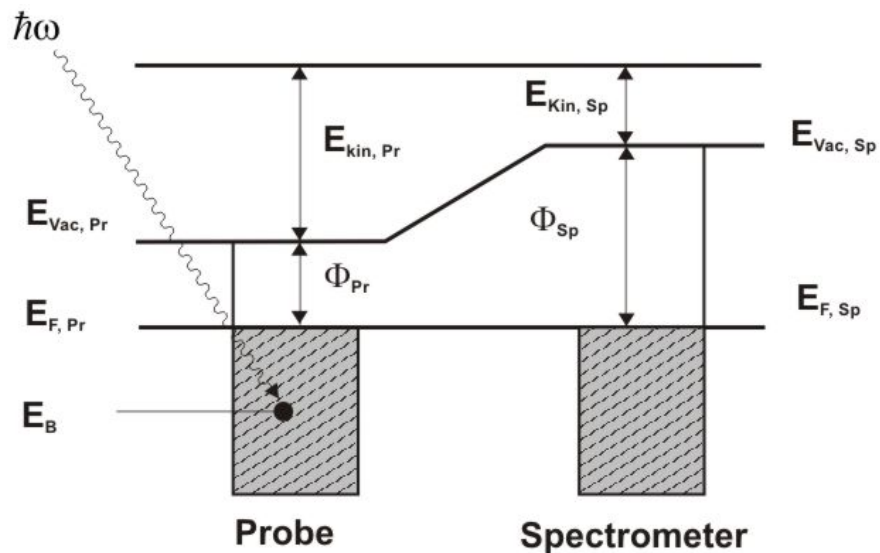


Fig. 3.12: The energy diagram of an UPS measurement. Probe and analyser are in electrical contact (the Fermi levels are aligned).

$$\begin{aligned}
 E_{kin,Pr} &= \hbar\omega + E_B - \Phi_{Pr} \\
 E_{kin,Sp} &= E_{kin,Pr} + \Phi_{Pr} - \Phi_{Sp} \\
 \rightarrow E_{kin,Sp} &= \hbar\omega + E_B - \Phi_{Sp} \\
 E_{kin,Sp}^{\max} &= \hbar\omega - \Phi_{Sp}, & \text{Metal} \\
 E_{kin,Sp}^{\max} &= \hbar\omega - |E_{VBM}| - \Phi_{Sp}, & \text{Insulators} \\
 E_{kin,Sp}^{\min} &= \Phi_{Pr} - \Phi_{Sp}
 \end{aligned}$$

where $E_{kin,Sp}$, $E_{kin,Pr}$ and E_{VBM} are the kinetic energy of the ejected electrons, measured kinetic energy and maximum valence band energy, respectively. $\Phi_{Pr,Sp}$ is the work function of the probe and spectrometer, $\hbar\omega$ the photon energy. Binding energy, E_B , is negative, since the E_F is the zero level. Note that for semiconductors and insulators electrons with maximum kinetic energy originate from the valence band. Furthermore, it is common to align the vacuum energy level of the spectrometer with the Fermi level of the sample (eliminating the work function of the spectrometer). Hence, ejected electrons with lower kinetic energy can be easily detected. Finally, the work function of the metal and insulators are given by:

$$\begin{aligned}
 \Delta E &= E^{\max} - E^{\min} = \hbar\omega - \Phi_{Pr}, & \text{Metal} \\
 \Delta E &= E^{\max} - E^{\min} = \hbar\omega - |E_{VBM}| - \Phi_{Pr}, & \text{Insulator}
 \end{aligned}$$

Knowing the work function of the spectrometer (calibration experiment with metallic sample), the work function of the semi-conductors can be evaluated from the low energy cut-off of the UPS spectrum.

For the present study, widths of UPS spectra were taken, although there are several experimental problems concerning the work function evaluation (unknown E_F of the metallic substrate, calibration of the spectrometer). The aim was to have a rough estimation of the relative energies involved in the system. Accordingly, it is essential to have reproducible procedure to define precisely the low- and high-energy cut-offs. In Fig. 3.13 a close-up of the measured UPS signal (dashed line) of an MgO film (~10 ML) is illustrated. This data was modelled as follow: first the original data (dashed line) is levelled to the zero height by subtraction of a linear fit (dotted line) from the recorded data; the signal-to-noise ratio of the spectrum at high binding energies was then taken to determine the start and end points.

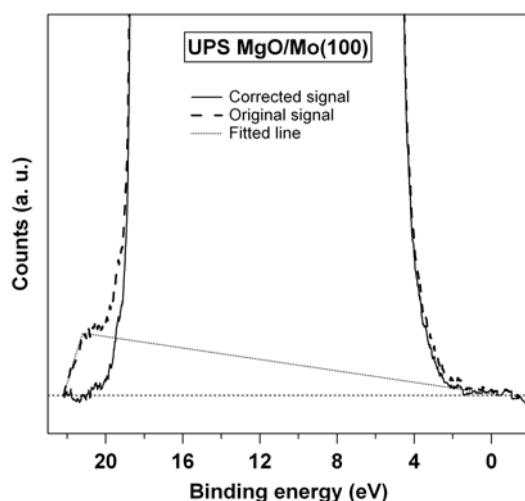


Fig. 3.13: Enlarged UPS spectra of an MgO film (~10 ML) at cut-off regions, recorded at ~120 K. Dashed and solid curves present original and corrected data, respectively. A linear fit is shown with dotted line.

It was also found that recorded data are markedly enhanced with the analyser transmission values. In the fixed analyser transmission (FAT) mode, the pass energy is usually held constant, and the retarding voltage is changed to adjust the given kinetic energy channel to the range accepted by the analyser. The influence of this parameter is clearly observed for MIES/UPS spectra of thin and thick films. In Fig. 3.14(a) and (b) MIES of a thin film (~1-3 ML) and UPS of a thick film (~10-15 ML), measured at various FAT (10 and 22 eV) are depicted, respectively. Note the significant enhancement in the recorded intensities for measurements carried out at FAT 22 eV as well as improvement at low- and high-energy cut-offs (solid lines).

In MIES spectrum contribution of the ejected electrons on both sides of the spectra are noticeably increased. Since MIES technique is only sensitive to the upper most surface layer, the role of the Mo substrate can be automatically discarded for thick films whereas, for thin films may not be the case. For UPS experiments that have longer penetration depths in comparison to MIES, at higher FAT values no subsurface contribution from the underlying metal substrate (at higher binding energy regime) in the spectrum width is observed. Enhanced intensities (amplitude) at higher energy regions ($> \sim 12$), observed for both measurements, are attributed to secondary electrons. Note that larger energies may also be affected by the emission of electrons backscattered from the bulk.

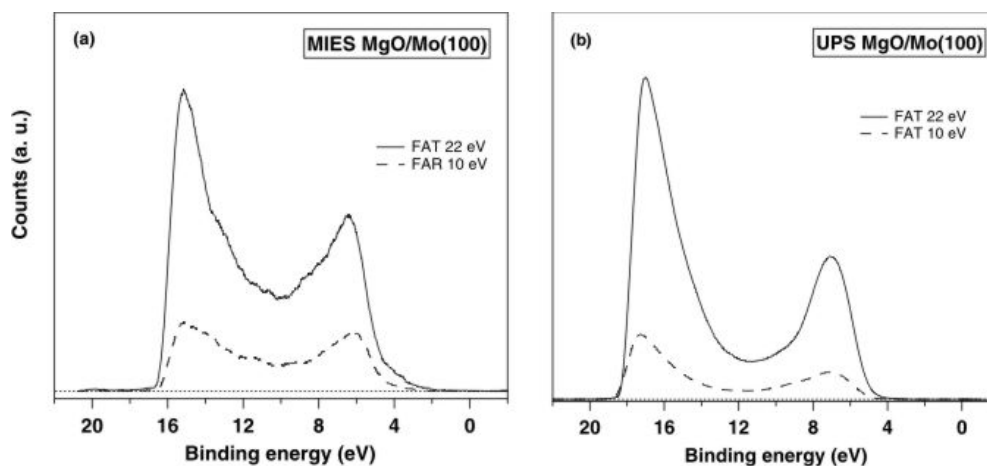


Fig. 3.14: Illustrating (a) MIES spectra of a thin (~1-3 ML); (b) UPS spectra of a thick (~10-15 ML) defect-poor MgO films measured at FAT 22 eV (solid line) and 10 eV (dashed line).

Resulting width from the treated data for a thin (~3 ML) and thick (~10 ML) film as shown in figure 3.10, is ~1.7 and ~3.8 eV, respectively. Interestingly, the measured spectrum width of a film with the thickness of ~6 ML (Fig. 3.10) is about 2.8 eV. Therefore, a broadening of the spectrum with thickness in our samples (MgO/Mo(100)) is concluded.

3.2. Exploration of the reactivity of cluster-based catalysts

3.2.1. Principles of temperature programmed desorption experiments

Temperature-programmed desorption (TPD) was originally developed by surface scientists to quantitatively investigate the kinetics of desorption of molecules from well-defined single crystal surfaces in high vacuum. In a typical TPD experiment, a surface is first exposed to a gas at a particular temperature in order to obtain a specific initial coverage. A sample is then heated, with a temperature program to create a linear rise in temperature with time. The partial pressures of atoms and molecules evolving from the sample are measured by a mass spectrometer in a continuously pumped ultrahigh vacuum system.

As the sample is heated, adsorbed gases desorb and sometimes decompose. With increased temperature, the desorption rate increases, eventually goes through a maximum, and drops back to zero as the surface is depleted of adsorbate. A desorption spectrum is a record of the concentration of desorbed gas as a function of temperature. The spectra usually have more than one maximum (peak). The shape and position of the peak maxima (peak temperature) are related to the desorption process, and therefore provide information on how the gas is adsorbed on the catalyst.^{100,101}

When experiments are performed on supported metal catalysts using a reactive gas, or when two reactive gases are coadsorbed, the technique will be referred to as temperature programmed reaction (TPR). Such reaction experiments, besides yielding kinetic data, can also contain detailed information and insight into reaction mechanisms, which cannot be obtained from steady-state experiments. This is due to the transient nature of TPD and TPR, in which both temperature and surface coverages vary with time and therefore, mechanistic information may be obtained. For instance, in steady-state reaction studies, the average of rates at several sites with different activities, possibly including sites on the support, is measured. Whereas, in TPR the rates on each of these sites can be separated, thus distinguishing different reactivities. Note that TPR is more complex than TPD, since competing processes such as the reaction of different adsorbed species and desorption of reactants and products occur simultaneously.¹⁰¹

However, the detailed analysis of the spectra can be obscured by experimental consideration, including diffusion, heterogeneous surfaces with a range of energy distributions, coverage-dependent kinetic parameters, and redesorption of the adsorbed gas. If the pumping speed is infinitely high, redesorption may be ignored. Thus, to bring out detailed kinetic information, a number of techniques are used, some of which require the generation of multiple spectra, corresponding to different rates of heating or different initial coverages on the surface.¹⁰¹ In this respect, molecular beam experiments are very valuable to study the reaction barrier heights and reaction dynamics.¹⁰²⁻¹⁰⁴

3.2.2. Introduction to CO combustion on surfaces

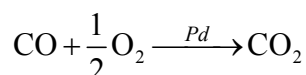
Studies of the interaction of reactant gases with metal surfaces have shown that the mechanisms of adsorption, surface reaction, and desorption can be extremely complex. However, a reasonably consistent basis for analysis of these processes has emerged from carefully performed experiments on unsupported metal single crystals under UHV conditions. The existence of precursor states in the adsorption kinetics was first proposed by Taylor and Langmuir¹⁰⁵ and a theoretical model was developed by Kisliuk¹⁰⁶. In these models one considers that molecules hitting a surface are either immediately reflected or trapped in a physisorbed state. Physisorbed molecules move across the surface and become chemisorbed when they encounter a vacant chemisorption site. These models explain sticking coefficient measurements for a large number of gases adsorbing on metallic surface.⁶⁰

The oxidation of poisonous CO over platinum group metals has received great attention in the literature due to its technological importance in cleaning exhaust pollutant of the automotive industry. Therefore, the interaction of CO with platinum group metals has been intensely studied in the last decades.^{60,102,103,107-111} It is generally accepted today that carbon monoxide adsorbs as a molecule on such a metal with the carbon atom directed towards the surface and that it can coordinate in several geometries.¹¹² The CO bonding to metal surfaces is described in the terms of the so-called Blyholder model, which invokes a donor-acceptor mechanism¹¹³. In this model the bonding occurs through a concerted electron transfer from the highest filled (5σ) molecular orbital of CO to unoccupied metal orbitals (essentially d orbitals), with back-donation occurring from occupied metal orbitals to the lowest unfilled (2π)

orbital of CO. The strength of the CO-metal bond might be expected to depend upon: 1) the nature of the adsorbent metal, 2) the crystallographic orientation of the surface, and 3) the geometric location of the adsorbed molecule on a given single crystal plane.¹¹⁴

Reaction mechanism

The CO oxidation on platinum group metal surfaces is one of the most widely studied subjects in surface chemistry as a model system of heterogeneously catalysed reactions:



There are several reaction mechanisms that one can imagine for the CO oxidation over metal surfaces. The three most popular ones are: the Langmuir-Hinshelwood (LH), Eley-Rideal (ER) and Mars van Krevelen (MvK) mechanisms. The common step in LH and ER mechanisms is dissociative chemisorption of oxygen on the catalyst. In the former mechanism, CO₂ formation takes place by interaction between both reactants in the chemisorbed state, whereas the ER mechanism is a collision type mechanism between a CO molecule in the gas-phase and dissociatively adsorbed oxygen atom. It is also found that pre-adsorbed carbon monoxide may act as an inhibitor for O₂ adsorption, and therefore for the reaction itself.^{103,115-117} In Fig. 3.15 the LH and ER are schematically depicted.

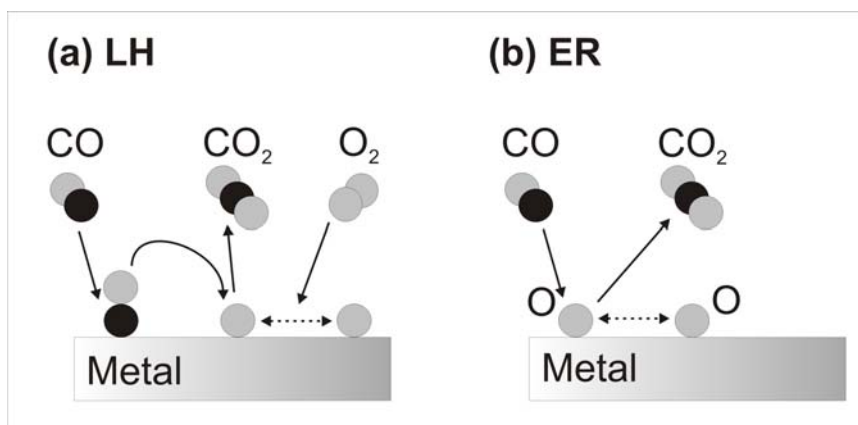


Fig. 3.15: Schematic representation of the Langmuir-Hinshelwood mechanism (a) and the Eley-Rideal mechanism (b) for the catalytic oxidation of CO. Dark and grey balls correspond to the carbon and oxygen atoms, respectively.

In the MvK mechanism the catalyst participates more actively in the reaction, playing the role of an intermediate product rather than merely a suitable substrate. The MvK mechanism consists of the following steps (Fig. 3.16). First in an oxygen-rich environment, i.e. at a high partial pressure of O_2 , and at elevated temperatures, the metal will oxidise. Depending on the detailed energetics of the metal and the oxide, either a thin film forms, as has been found for $Pt(110)^{118}$, or the oxidation slowly proceeds further into the metal, as seems to be the case for $Pd(100)^{119}$. After the palladium oxide has been formed at the surface, CO molecules adsorbed on the oxide from the gas phase will react with oxygen atoms from the oxide to produce CO_2 . The resulting oxygen vacancies are refilled rapidly by oxygen from the gas phase.

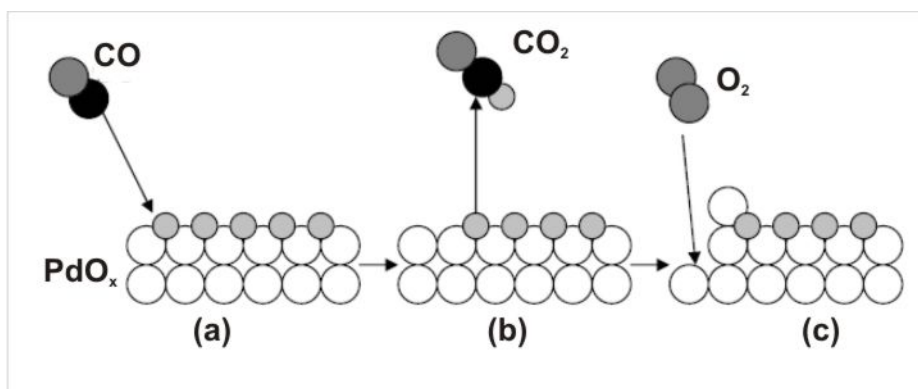


Fig. 3.16: Schematic representations of the Mars van Krevelen mechanism. The empty balls represent Pd atoms. Small and regular-sized grey balls indicate the oxygen atoms from the palladium oxide and gas-phase, respectively. The dark balls correspond to the carbon atoms. (a) PdO_x and a CO molecule diffusing to the surface. (b) Reaction between the CO molecule and one oxygen atom from the palladium oxide, the formation of the CO_2 molecule and its diffusion in the gas-phase. (c) The diffusion of the left uncoordinated Pd atom and the refill of the vacancy left by the oxygen atom, with oxygen from the gas-phase.

One of the most fascinating aspects of chemical reactions taking place under conditions far from equilibrium is the possibility to exhibit instabilities and oscillations. Two key features are used to describe such phenomena: “nonlinearity” and “feedback”. If the first term is related to the mathematics behind these processes, the feedback arises when the products of later steps in the mechanism influence the rate of some of the earlier reactions steps and, hence, the rate of their own production. This may take the form either of positive feedback (self-acceleration) or negative feedback (self-inhibition)¹²⁰. Another

phenomenon closely related to self-sustained oscillations is that of multiplicity of stationary states. In other words, under constant external conditions the reaction has more than one stationary state composition to choose from. A well-known example in heterogeneous catalysis is the oscillating oxidation of CO on platinum group metals (mainly Pt and Pd)¹²¹. In this context, the well-known “oxide model”¹²² and “carbon model”¹²³ attribute the oscillations near atmospheric pressure to periodic formation and reduction of a Pt-surface oxide or to periodic changes of the blocking of the catalyst by carbon.

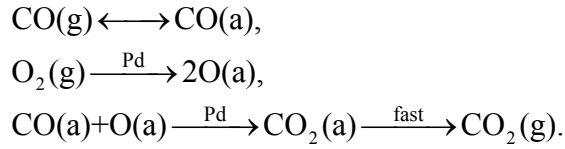
As described previously in this chapter, CO oxidation over Pd surfaces is thought to follow Langmuir-Hinshelwood kinetics. Thus, the focus of the preceding chapter will be introducing a model to simulate TPR on the basis of kinetic equations involved in the Langmuir-Hinshelwood reaction mechanism for the ¹³CO oxidation reaction, and to analyse experimental data of palladium cluster catalysts to show the potential of the method.

3.2.3. Experimental

For TPR studies, cluster model catalysts were produced by soft-landing size-selected Pd clusters onto an MgO substrate. The prepared model catalyst was then dosed at ~100 K with both reactants (coadsorption of ¹³CO and O₂). Following the loading of the catalyst with the reactants, the sample is resistively heated at constant rate (2 K s⁻¹) up to a ~700 K. A temperature feedback system was used to control the heating through a software of home-built design. The products from the TPR experiment were detected in a single reaction cycle using a quadrupole mass spectrometer and recorded using a personal computer (see chapter 2). With the known cluster coverage and a calibrated mass spectrometer the average number of formed product molecules and desorbing reactants can be measured for varying initial coverages. Moreover, the temperature of maximal reaction rate gives a simple estimation of the activation energy of the involved catalytic reaction. This value is often compared to theoretical activation energies from *ab initio* calculations in order to obtain a molecular picture of the catalytic reaction. More accurate activation energies can be obtained when using kinetic simulations to model TPR results.

3.2.4. Theoretical

To model TPR spectra, first the elementary steps in the overall CO oxidation reaction are considered, which can be summarised as following:



As the CO₂ desorption is much faster than its formation, adsorbed CO₂ is not included in kinetics analysis. Note that low energy barriers for CO₂ desorption is not necessarily always true, as it evidenced by TPR studies on Au₂₀ based catalysts supported on thin defect-poor MgO films (see chapter 4). The relatively strong bonding between reaction intermediates and support material leads to the high desorption energy. Also, it is assumed that oxygen to be fully dissociated on adsorption over palladium^{124,125} and therefore, the rate of desorption is omitted in kinetics formulation. Thus, the kinetic equations for the oxidation of CO can be solved using the following coupled differential equations:^{126,127}

$$r_{\text{CO}} = \eta_{\text{CO}} \alpha_g^{\text{CO}} - k_d \theta_{\text{CO}} - k_L \theta_{\text{CO}} \theta_{\text{O}} \quad (1)$$

$$r_{\text{O}} = 2\eta_{\text{O}_2} - k_L \theta_{\text{CO}} \theta_{\text{O}} \quad (2)$$

$$r_{\text{CO}_2} = k_L \theta_{\text{CO}} \theta_{\text{O}}, \quad (3)$$

where $\eta_{\text{CO},\text{O}_2}$ are proportional to the incoming flux of reactants, k_d is the desorption rate constant, k_L is a Langmuir-based rate constant for the reaction, $\theta_{\text{CO},\text{O}}$ the coverage of reactants, $r_{\text{CO},\text{O}}$ the rate of reactant changes and α_g^{CO} sticking coefficient for the reactants including the non-reactive reverse spill-over (also referred to as the global sticking coefficient).¹²⁸ In fact, the net CO flux is the sum of the direct flux from the gas-phase and indirect diffusion flux from the support, i.e. reverse spill-over. It has been shown experimentally^{60,61,129} that the reverse spill-over enhances the reaction rates while acting as a precursor state (molecule collector) for CO chemisorption on the catalyst. The rate of product formation is given by r_{CO_2} . For both k_d and k_L , a simple Arrhenius type temperature dependency are considered:

$$k_L = \nu_L \exp\left(-\frac{E_L}{k_B T_s}\right), \quad (4)$$

$$k_d = \nu_d \exp\left(-\frac{E_d}{k_B T_s}\right), \quad (5)$$

where T_s is the sample temperature, k_B is the Boltzmann constant, and ν_L and ν_d are desorption and Langmuir-based pre-exponential factors, respectively.

Moreover, in desorption energy a coverage dependency is introduced due to the lateral interaction of the adsorbate molecules that results in a pronounced coverage dependency of the CO adsorption energy:¹²⁷

$$E_d = E_{d,i} \left(1 - \frac{\theta_{CO}}{w\Omega_{CO}}\right), \quad (6)$$

with $E_{d,i}$ zero coverage desorption and Ω saturation coverage of CO on Pd and w weighting factor. Note that for the maximum coverages Ω_o and Ω_{CO} were chosen to be the saturation coverages of the reactants on a Pd(111) surface. In table 1 all the parameters used in the calculation are given.

Based on above-mentioned kinetics model, TPR spectra were simulated through omitting the flux of reactant molecules and starting from the saturation coverage of reactants. Following a calculation of the CO₂ amount, the CO and oxygen remaining were used to restart the calculation (Appendix D).

Parameter	Value	Details
$E_{d,i}/\text{kJ mol}^{-1}$	118	Ref. 125
Ω_{CO}	0.5	Ref. 129
Ω_o	0.25	Ref. 129
Ω_{CO}/MgO	0.5	Ref. 60
$R_c/\text{Å}$	10	Ref. 125
E_{sad}/eV	0.25	Ref. 60
ν_L/s^{-1}	$10^{7.9}$	Ref. 125
ν_{CO}/s^{-1}	10^{14}	Ref. 125

Table 3.1: The values used in the TPR simulations.

3.2.5. Results and discussions

Temperature programmed reaction experiments

Fig. 3.17(a) shows the oxidation reaction of ¹³CO over Pd₃₀ clusters (~0.2% ML) using a simple TPR experiment. Prior to a TPR, the oxygen was exposed onto

the catalysts at ~ 100 K, followed by dosing of the ^{13}CO . As the temperature is increased, the CO_2 formation begins at ~ 300 K and then finally deteriorate at higher temperatures as all reactant molecules disappeared through desorption or reaction. In case of CO oxidation, the calculated energy is attributed only to the reaction, since desorption of CO_2 molecules is a fast, barrier-less step. The single peak in the TPR does not necessarily illustrate that there is only a single reaction pathway occurring. Multiple pathways are possible, however, in order to observe these pathways as individual peaks in the TPR, they must be separated far enough in reaction energies to be seen resolved. This will be described in detail later using TPR simulations.

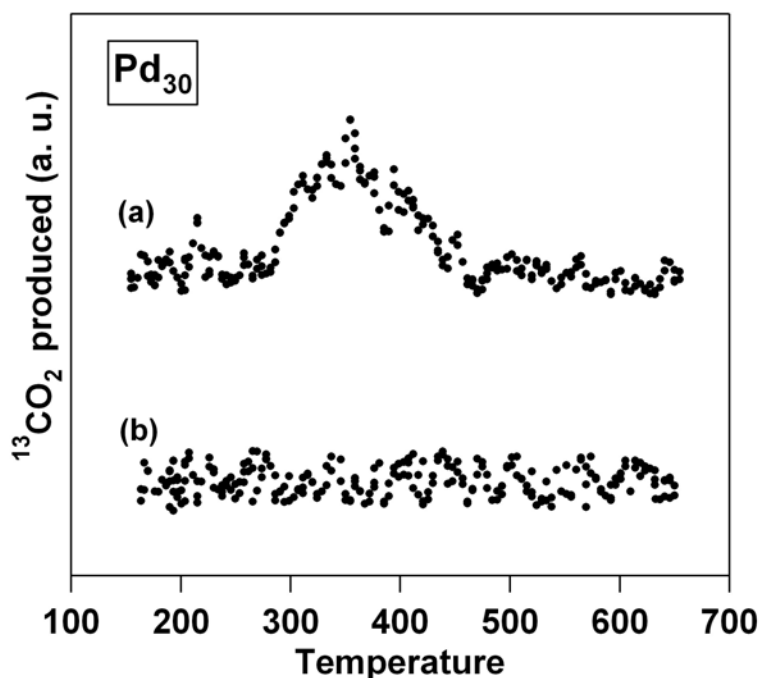


Fig. 3.17: TPR studies of Pd_{30} clusters on an MgO film ($\sim 0.2\%$ ML). (a) Shows the TPR produced when O_2 is dosed followed by CO . (b) Illustrates a TPR experiment following the dosage of CO and then O_2 .

Furthermore, in a TPR experiment by changing the order, in which the reactants are dosed, valuable information about the influence of the cooperative coadsorption of reactants on the catalytic reactivity of the catalyst can be derived. This aspect of TPR studies is illustrated by the comparison of Fig. 3.17(a) and (b). Although an identical catalyst has been used in both cases, sample in Fig. 3.16(b) shows no catalytic activity. This is simply because in the former TPR, O_2 is dosed before ^{13}CO , whereas in the latter case (Fig. 3.17(b)) the contrary is true. Since on a palladium single crystal, CO has both a larger saturation coverage and sticking coefficient than O_2 ^{130,131}, presumably this is

also true for Pd₃₀ clusters. Thus, it is clear that by initially dosing ¹³CO, all the active adsorption sites are occupied and so no O₂ can adsorb.

Temperature programmed reaction calculations

For a better understanding of the TPR spectra, micro-kinetic modelling of the system is helpful. Here a LH mechanism with a single activation barrier is assumed (appendix D). Figure 3.18 illustrates the simulated TPR spectra made at two different heating rates, for CO oxidation on Pd₃₀ clusters with various activation energies. This is obvious that in the catalytic systems with various activation energies and a similar desorption energy, the reaction starts at higher temperatures for a catalyst with higher activation energy and accordingly more reactant molecules may desorb prior to the reaction. This implies variations in peak position and height with reaction energy as seen in Fig. 3.18. Additionally, at constant activation energy by enhancing the heating rate, the height of the signal increases and the peak maximum shifts to higher temperatures. This is because the time integral of the TPR spectrum remains constant when only heating rate is changed.

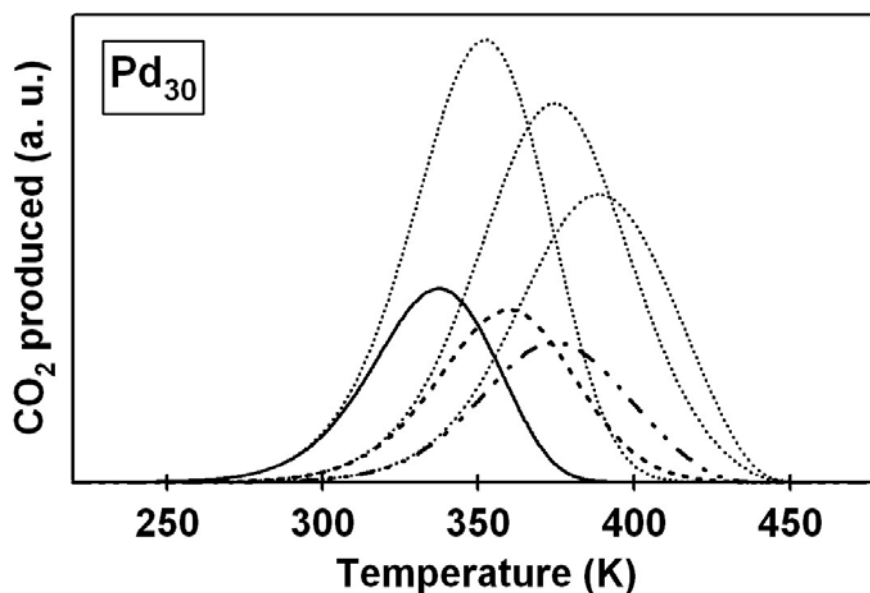


Fig. 3.18: Simulated TPR spectra using variable activation energy for the oxidation of CO used to illustrate one reaction pathway for Pd₃₀ clusters on an MgO film with a heating rate of 2 K s⁻¹. The activation energy used in each spectrum is (solid line) 55 kJ mol⁻¹, (dashed line) 59 kJ mol⁻¹ and (dash-dotted line) 62 kJ mol⁻¹. For comparison the same spectra are recalculated for a heating rate of 5 K s⁻¹ (dotted line).

When more than one reaction sites with different activation energies exist, a structured TPR spectrum results (blue solid line in Fig. 3.19) which is the

weighted superposition (50%) of individual reaction sites (blue dashed line in Fig. 3.19). If activation energies of the involved reaction sites are close in energy (black dashed lines in Fig. 3.19), the single contributions are not resolved. Consequently, the TPR reveals a broad feature as shown in Fig. 3.19 (black solid line).

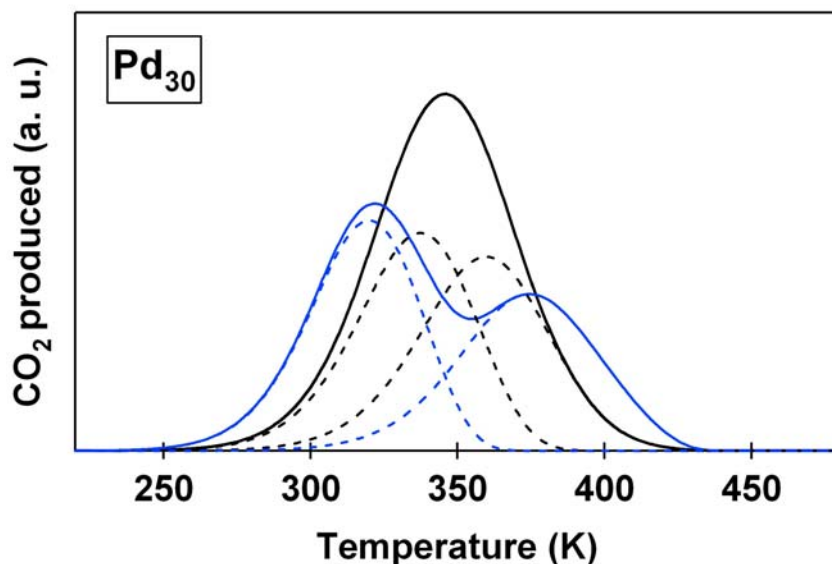


Fig. 3.19: Simulated TPR spectra of CO combustion on Pd₃₀ clusters supported onto an MgO film involving a dual reaction sites. Black solid line: 55 and 59 kJ mol⁻¹, blue solid line: 52 and 62 kJ mol⁻¹. Dashed lines correspond to each single reaction site.

Applying a weighted superposition is justified considering the reaction kinetics in more detail. That is the contribution of various reaction energies for different reactive sites (direct adsorption) as well as the reverse spill-over of reactants on the support towards reactive centres (indirect adsorption). The latter may lead to low-temperature reactivities of the catalyst. Note that the contribution of the possible reactivity paths is not necessarily equal and thus a weighted superposition is required. This concept is demonstrated with an example using the experimentally recorded TPR spectrum for the ¹³CO oxidation on Pd₃₀ clusters supported onto an MgO film. As illustrated in Fig. 3.20, the experimental data reveal a broad peak indicating the presence of manifold reaction sites (markers (•) at the bottom). A good agreement between experimental data and simulations can be achieved, if a superposition of various reaction sites with similar activation energies is considered. To do this, first different energy barriers were chosen to cover the experimental

temperature range, where the peak appears. Then, the contribution of each reaction site was determined by weighing factor.

For the present case, the experimental spectrum is well reproduced using three different activation energies (E_L) of ~ 53 , ~ 58 , and ~ 67 kJ/mol with the weighing factors of 20%, 20%, and 60%, respectively. This suggests that for the oxidation of ^{13}CO over Pd_{30} cluster catalysts, at least three different reaction pathways exist. The reaction path with highest energy barrier dominates the process. There are three times more sites for this pathway as there are for each of the other two pathways. However, the reaction occurs more effectively through the paths with lower energy barriers since there are more ^{13}CO molecules available at lower temperatures. Note that this can be different for measurements under steady state conditions having constant intensity of reactant molecules throughout the temperature and pressure ranges of investigations. In the molecular beam experiments, for a precise quantitative description of the kinetics, factors such as the change in sticking coefficients due to coadsorption and their temperature dependence, the relative rates of diffusion of the two adspecies and the surface configuration as a function of temperature and pressure are considered.

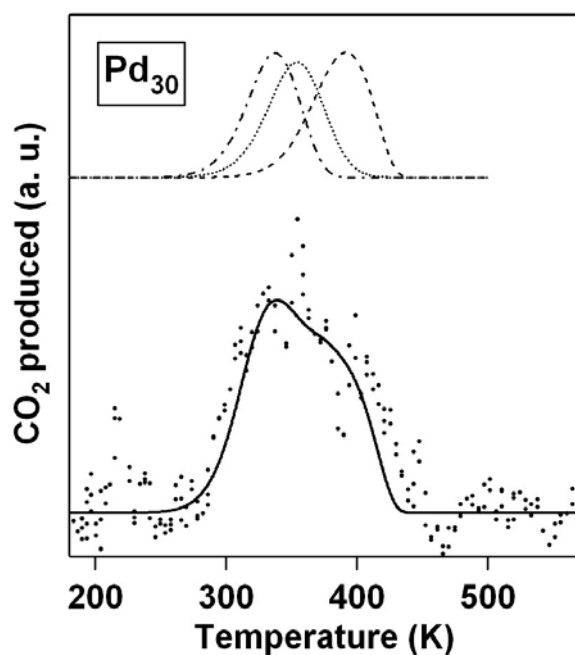


Fig. 3.20: Illustrating a comparison between experimental (dotted line) and simulated (solid line) TPR results of the ^{13}CO oxidation on Pd_{30} clusters. The superposition of three simulated spectra with the activation energies of 53, 58 and 67 kJ/mol (top spectra) is used to create final TPR spectrum.

The theoretical description was greatly enhanced for pulsed-molecular beam experiments¹²⁶ by addition of the migration of reactant molecules from the

support to the reactive centres (reverse spill-over) using a capture zone model⁶⁰. The capture zone model is a kinetic model to incorporate the flow of reactants from a support to the active centres. Including this model in the reaction kinetics is important due to the small ratio between area of the active centres and support material. As a consequent, to explore the effect of reverse spill-over of the surface adsorbed CO in the TPR experiments, a capture zone model is also included in the TPR simulations. In this context, the elementary steps involved in the adsorption process are schematically depicted in Fig. 3.21. Molecules impinging on the substrate can be (1) reflected (elastically and inelastically) or (2) adsorbed in a physisorbed state on the MgO surface, where they hop from site to site (surface diffusion). Furthermore, the chemisorption on the model catalysts originates from two channels: (3) capture of a

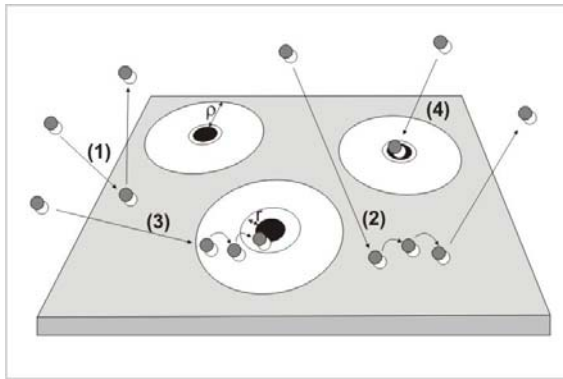


Fig. 3.21: Schematic representation of the elementary steps in CO adsorption processes. (1) Quasi-elastic reflection, (2) chemisorption on the clusters by reverse spill-over of the CO molecules adsorbed in the capture zone, (3) adsorption and diffusion on the substrate, (4) chemisorption on the clusters through direct impingement.

molecule physisorbed on the bare substrate, and (4) direct impingement. Note that a physisorbed molecule travels on a mean distance X_s prior desorbing from the surface. Therefore, a capture zone around each cluster can be defined at first approximation with a maximum width equal to X_s . This length increases with temperature as expressed by the following equations (Eq. 8-10) and hence results in a larger capture area.⁶⁰

$$X_s = \sqrt{D\tau}, \quad (8)$$

$$D = a_0^2 v_d \exp\left(\frac{-E_d}{k_B T}\right), \quad (9)$$

$$\tau = \frac{1}{v_a} \exp\left(\frac{E_a}{k_B T}\right), \quad (10)$$

where D is the diffusion coefficient, τ the mean life time of a physisorbed molecule, a_0 the pre-exponential factor related to the distance between two

neighbouring adsorption sites, ν_d and ν_a the frequency factors for the diffusion and adsorption processes, k_B the Boltzmann constant, E_d diffusion energy, E_a adsorption energy, and T the substrate temperature. Accordingly, the diffusion length X_s of the CO on the support can be defined as a function of saddle energy (difference between the adsorption and diffusion energies) and is given by:

$$X_s = a_0 \exp\left(\frac{-E_{sad}}{2k_B T}\right), \quad (11)$$

The maximum capture area is achieved when X_s is the half of the distance between neighbouring clusters (L). It is also assumed that all the molecules that adsorbed in the capture zone will join the cluster. Finally, considering the above discussed points and Fig. 8 the capture width can be defined analytically by the following equation:⁶⁰

$$\pi(\rho^2 + 2\rho R_c) = 2\pi R_c X_s P\left(\frac{R_c}{X_s}, \frac{L}{X_s}\right), \quad (12)$$

in which R_c and X_s are the cluster radius and mean diffusion length of the CO before desorption, respectively. $P\left(\frac{R_c}{X_s}, \frac{L}{X_s}\right)$ is a part of the diffusion equation modelled by modified Bessel functions. L is defined as a half of the distance between two adjacent clusters, which is related to the number density of clusters.

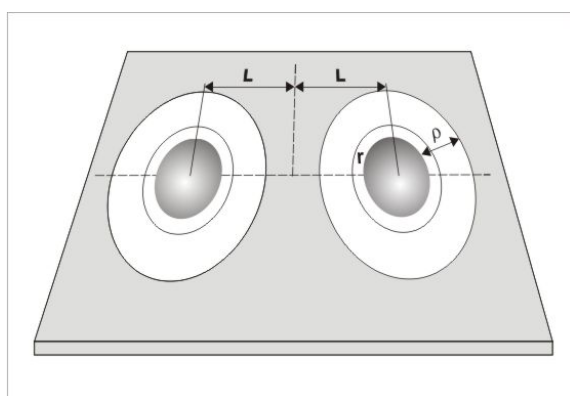


Fig. 3.22: Showing schematic representation of two neighbouring clusters with radius of R_c (grey ball in the middle). $2L$ is the distance between adjacent active centres, ρ the width of capture zone and r the width of the cluster periphery.

In the present TPR model, only the reverse spill-over of the CO adsorbed on the capture zone with a width of ρ was included. Additionally, at close vicinity of the cluster periphery a specific area (circular segment, $r = 0.2$ nm) was defined (Fig. 3.22). Arriving chemisorbed CO molecule at this area either contributes to the

reaction or desorbs when no empty active sites are available on the cluster. Given literature values for desorption and diffusion energies of CO on an MgO surface are in a range of $\sim 13\text{--}42$ kJ/mol.^{112,132,133} However, in the present model higher values were taken, to upper limit possible effects of the CO reverse spill-over in the oxidation reaction over cluster model catalysts. Consequently, for the region around the cluster periphery desorption and diffusion energies of CO molecules were considered to be ~ 50 and ~ 90 kJ/mol, respectively. The simulated TPR spectra with and without inclusion of the capture zone (CO reverse spill-over) exhibit no variation in the formation of CO₂ product molecules, as shown in Fig. 3.23.

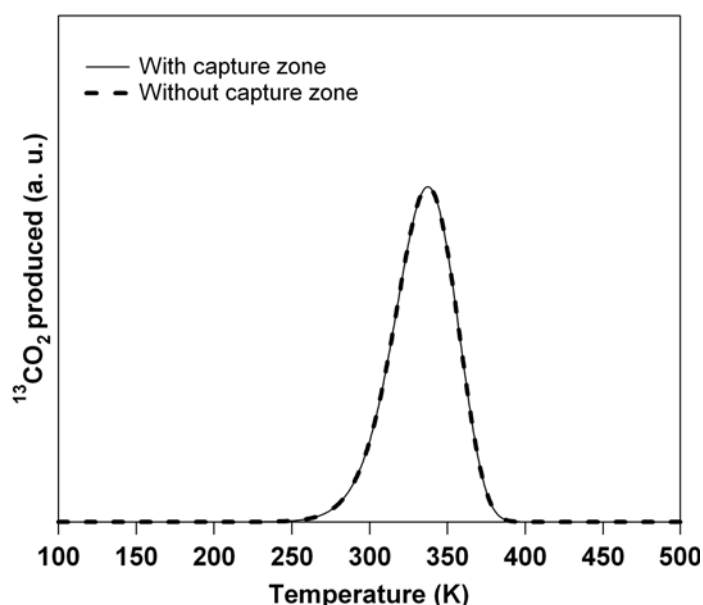


Fig. 3.23: Simulated TPR spectra for the CO oxidation on Pd₃₀ catalysts ($\sim 0.2\%$ ML) including the capture zone (solid line) and without capture zone (dashed line). To determine the influence of the CO reverse spill-over, the upper limit values for desorption and diffusion energies were considered.

Note that although the desorption energies (E_{des}) are significantly increased in comparison to the literature values, no influence of the CO reverse spill-over in the oxidation reaction during the TPR experiment is observed. This suggests that CO molecules entering the specific periphery area *via* reverse spill-over have desorbed completely prior to the beginning of the catalytic oxidation reaction and thus do not contribute to the reaction, as shown in Fig. 3.24 (dash-dotted line). By heating the catalyst in a TPR experiment, the coverage of reactants remain constant (0.5 and 0.25 for CO and O, respectively) up to a temperature, where the reaction starts ($E_{\text{des}} > E_{\text{L}}$). While oxygen is present, the coverage of both reactants reduces with same rates with increasing

temperature. Finally, when there is no more oxygen available at temperatures above 380 K (solid line), CO desorbs to completion with higher rates (dash line). The capture zone is also saturated with chemisorbed CO (dotted line) after CO exposure. Additionally, the coverage of the periphery region attains its maximum at temperature between 150 and 250 K. Consequently, at the temperature where the oxidation reaction begins (~300 K), adsorbed CO molecules on the capture zone and the region around clusters have already desorbed at lower temperatures ~230 (dotted line) and ~260 K (dash-dotted line), respectively.

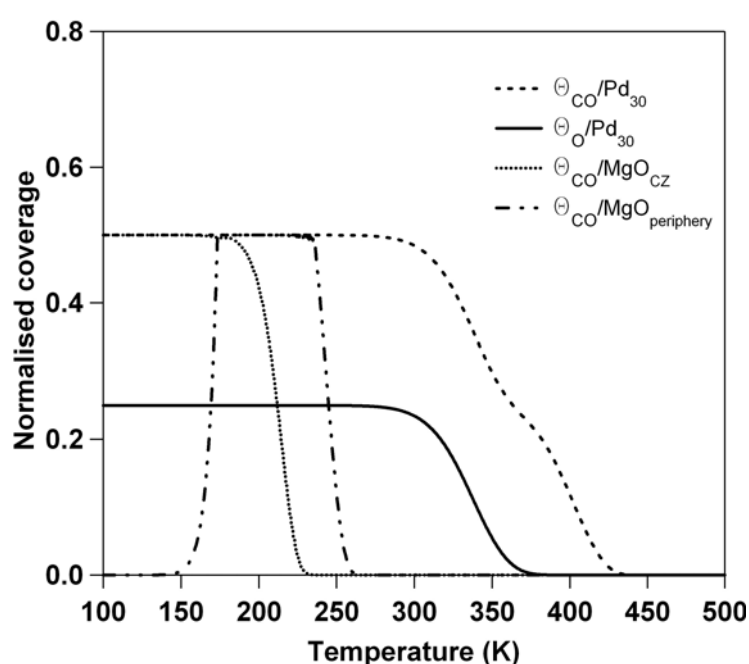


Fig. 3.24: Showing oxygen coverage on Pd₃₀ catalyst (solid line) and CO coverage on: clusters (dashed line), capture zone (dotted line), and magnesia surface close to the cluster periphery (dash-dotted line)(see text).

These results show remarkable agreement with our theoretical and experimental p-MBRS investigations of CO oxidation on palladium based catalysts.¹²⁶ In these studies, the addition of CO reverse spill-over effects has significantly improved the agreement between experimental observations and theoretical findings at low temperatures.

3.2.6. Summary

A model has been developed to simulate temperature programmed reaction spectra of the CO oxidation over Pd model catalysts. The model is particularly useful in providing information about the energetics of the manifold reaction

pathways. Furthermore, simulations revealed that for the TPR experiment, the reverse spill-over of CO on magnesia support has no influence in the oxidation reaction on the model catalyst, because the surface adsorbed CO molecules have already desorbed at lower temperatures than the reaction temperature. This is consistent with p-MBRS experiments which have shown that by introducing CO reverse spill-over effects and considering intrinsic support interactions in the kinetic simulations a better agreement with experiment can be obtained for measured low-temperature reactivity.

Chapter 4

4. Catalysis of magnesia supported Au₂₀ clusters

The discovery of the extraordinary activity exhibited by very small gold clusters on certain oxide supports¹³⁴ has stimulated considerable research^{2,15,135,136} to address the origin of such surprising observations. Although bulk gold is a classic example of chemical inertness^{137,138}, Haruta *et al.*'s findings showed that dispersed ultrafine gold particles, supported on metal oxides reveal pronounced catalytic activity for low-temperature oxidation of hydrocarbons and carbon monoxide. Many later studies have further manifested the support- and size-dependent reactivity (corresponding to the dispersion and preparation methods) of gold nanoparticles.^{18,136,139-142} A particularly nice example of this novel heterogeneous catalysis was, however, illustration of the size-dependent activity of nanoscale gold clusters (see chapter 1).^{2,23} Catalytic combustion of CO on size-selected gold clusters supported on relatively thick, defect-rich MgO surfaces has demonstrated the low-temperature reactivity of Au_n clusters with $8 \leq n \leq 20$ gold atoms. A nonplanar Au₈ cluster has emerged as the smallest catalyst to exhibit such catalytic activity.

As described thoroughly in the introductory chapter, the role of support material on nanocatalysis is indispensable for determining the morphology and catalytic performance of the cluster catalysts. Indeed, novel tunable catalytic properties may evolve from understanding particle size effects in conjunction with support-induced effects. Most recently, aberration-corrected transmission electron microscopy investigations¹⁴³ have shown that the high catalytic activity for CO oxidation at ambient temperature is unambiguously correlated with the presence of bilayer clusters (supported on a metal-oxide) that are less than 1 nm in diameter and contain only 10 gold atoms.

In the following, studies on the support-induced activity of size-selected gold clusters (Au₂₀), soft-landed onto various MgO(100) thin films, are addressed.

4.1. Tuning of the catalytic performance of Au₂₀ model catalysts

The control of geometry and catalytic properties of gold nanostructures by tuning the support properties has been predicted theoretically⁵² and confirmed experimentally⁵⁴. The experimental and theoretical investigations, performed in

this work aim to demonstrate the dependence of catalytic activity and microscopic reaction mechanisms, on the thickness and stoichiometry of the MgO films, as well as on the dimensionalities and structures of the adsorbed gold clusters (Au₂₀). In this respect, temperature programmed reaction (TPR), Fourier transform infrared spectroscopy (FTIR) experiments, and *ab initio* calculations were carried out.

TPR experiments are particularly well suited for the discussion of possible reaction mechanisms since reaction temperatures can be correlated with activation (transition state) energies obtained from first-principle simulations of reaction mechanisms. These combined experimental and theoretical studies give valuable information about reaction mechanisms, the atomic and molecular arrangements of reactants, and the electronic structure of the catalysts.

4.1.1. Experimental and theoretical methods

Preparation of the model catalyst: Model catalysts were prepared by the deposition of ~0.3% ML mass-selected Au₂₀ clusters onto MgO(100) films. Oxide films of various thicknesses (1-10 ML) and stoichiometries were synthesised by varying the growth time and magnesium flux. Changing the latter parameter in a constant oxygen background creates films with different densities of oxygen vacancy centres. The cleanliness and composition of oxide films and the underlying substrate were assessed through AES and further characterisation of the electronic structure was achieved using MIES and UPS experiments (see § 3.1).

TPR experiments: The catalytic oxidation of ¹³CO on Au₂₀ based model catalysts was investigated employing isotopic labelled TPR experiments. The reactant gases were sequentially dosed onto the surface (at ~100 K) to an exact coverage (one Langmuir, 1L) using a calibrated molecular beam doser. A temperature programmed ramp of the sample was performed between ~100 and ~800 K using a feedback-controlled resistive annealing system of in-house design. Products from the reaction were measured using a quadrupole mass spectrometer (see chapter 2). Recorded isotopically labelled product molecules (¹³C¹⁶O₂) are shown in Fig. 4.1.

FTIR experiments: For FTIR studies, low-temperature exposures were carried out in a similar procedure to that in the TPR experiments. Following the coadsorption of O₂ and ¹³CO, IR spectra were recorded at a grazing angle of incidence. The stretching frequencies of the adsorbed ¹³CO were determined both prior to, and after initiation of the oxidation reaction at various temperatures (Fig. 4.2).

Theoretical methods: First-principles density functional theory (DFT) calculations were made by group of U. Landman.^{144,145} In these theoretical studies, the generalised gradient approximation (GGA)¹⁴⁶ and ultrasoft pseudopotentials¹⁴⁷ (scalar relativistic ones for gold) with a plane wave basis (kinetic energy cutoff of 300 eV) were employed.

4.1.2. Experimental and theoretical findings

Experimental: In a first experiment, Au₂₀ clusters were deposited on a molybdenum support, which was exposed to oxygen under the same conditions as in a typical MgO film preparation procedure (5×10^{-7} mbar O₂, T \sim 300 K, \sim 20 minutes). This experiment is rather important since thin MgO films of thicknesses with up to \sim 3 ML are not necessarily continuous. Note that MgO films on molybdenum are known to grow *via* island formation. This is consistent with recent STM and AFM studies carried out in our group for the growth of MgO on silver single crystals.^{Bielezki, 2009 #365} It is therefore likely that although a film is calculated to have \sim 1-3 ML coverage, it actually consists of islands, which are 1 to 3 layers thick, interspaced by partially oxidised Mo. Consequently, Au₂₀ clusters which deposited between MgO islands could be assumed to be involved in the formation of CO₂, in addition to the reaction catalysed by the gold clusters anchored on the MgO film. The fact that the inter-island (oxidised molybdenum) does not contribute to the CO oxidation reaction has been verified by this TPR measurement, where no ¹³CO₂ signal has been recorded in TPR spectrum (Fig. 4.1(a)). As shown in spectrum (a), gold clusters deposited on partially oxidised Mo are not reactive, thus, we conclude that only Au₂₀ clusters on MgO islands contribute to the observed catalytic activity. More interesting is, however, the observed reactivity upon deposition of gold clusters on molybdenum-supported MgO films Fig. 4.1(b-e). The reactivity of gold clusters supported on MgO films appears to vary significantly with film thickness. Firstly, on relatively thin MgO films ($< \sim$ 3 ML) TPR spectra show two

regimes of CO₂ formation: a minor peak at ~180 K with the major product formation occurring at ~300 K (Fig. 4.1(b-d)). An interesting point to remark about these spectra is the narrowing of the high-temperature reaction peak with increasing film thickness. This broad high-temperature reactivity may correspond to the periphery mechanism discussed in § 4.2.2, however, it may also involve high activation energies (the formation and/or desorption of CO₂) due to more dominant metal support effects on thin films, which attenuates at higher thicknesses. Secondly, on a thick (~10 ML) and presumably continuous MgO film, (break-point analysis, see § 3.1), the model catalyst exhibits only a single peak at ~250 K that is markedly lower than the higher temperature peak recorded for the thin-film-based catalyst as shown in Fig. 4.1(e).

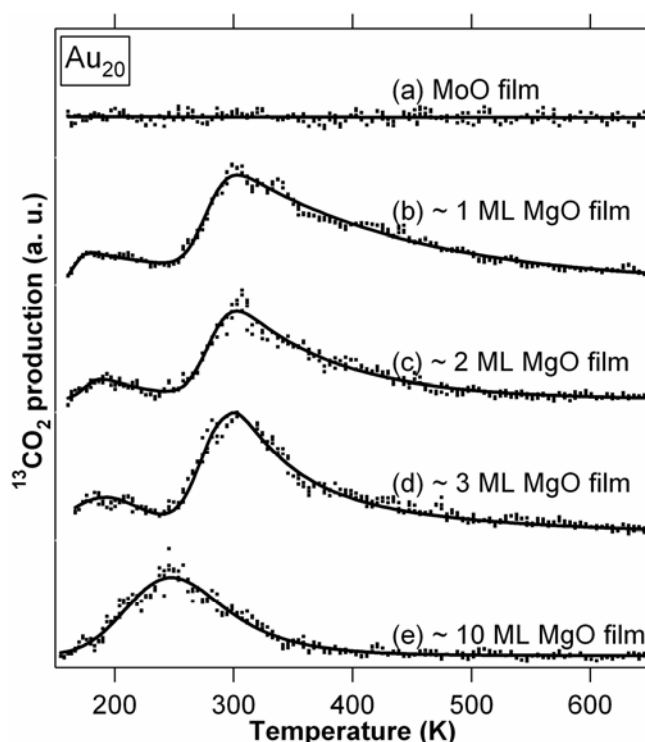


Fig 4.1: TPR spectra illustrating ¹³CO₂ reaction products over Au₂₀ clusters (~0.3% ML), deposited onto MgO films of various thicknesses (1-10 ML). Markers represent the experimental data points; the solid line is a multi-peak exponential Gaussian fit of data to guide the eye.

To explore the effects of film composition on reactivity, similar measurements were performed on thick defect-rich films (Fig. 4.2). Unlike the low-temperature reactivity of a defect-poor thick film (Fig. 4.2(a)), which indicates a single reaction channel, the TPR study of a defect-rich film (Fig 4.2(c)) shows two

reaction regimes. The lower temperature reactivity is observed at ~200 K and the higher temperature reactive regime is located in the vicinity of ~400 K.

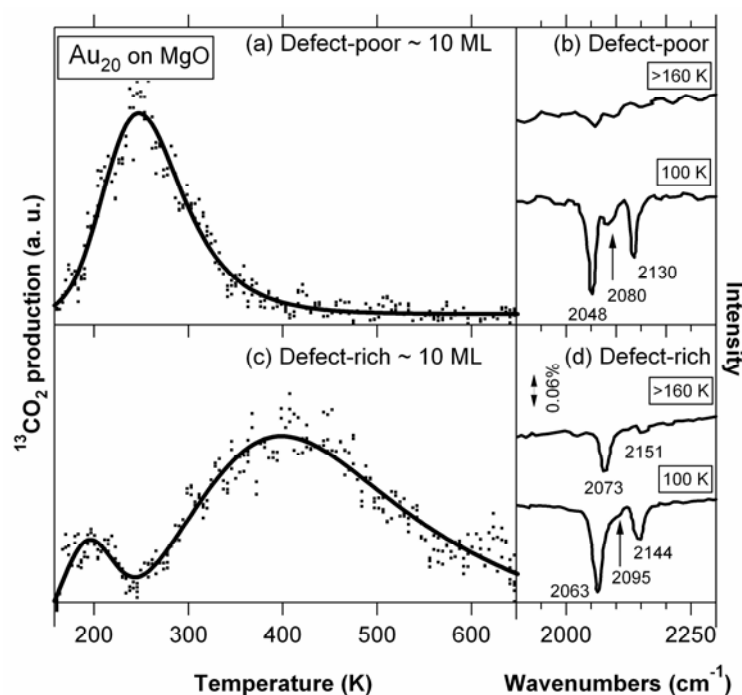


Fig 4.2: TPR measurements made on Au₂₀ clusters using thick (~10 ML), defect-poor and defect-rich MgO films shown in (a) and (c), respectively. Markers show the experimental data points and the line is a multipeak exponential Gaussian fit of the data. Figures (b) and (d) are FTIR studies corresponding to figures (a) and (c), respectively.

Further investigations of the effects of defects on the Au₂₀ catalytic activity were performed employing FTIR spectroscopy. Stretching frequencies of ¹³CO coadsorbed with ¹⁸O₂ are shown in Fig. 4.2(b) and (d). At low temperatures (~100 K) and prior to CO combustion, Au₂₀ on both defect-poor (Fig. 2(b)) and defect-rich (Fig. 4.2(d)) MgO films readily adsorbs ¹³CO. Three bands at 2048 cm⁻¹, 2080 cm⁻¹, and 2130 cm⁻¹ are observed for the model catalysts with defect-poor support materials. Note that ¹³CO on MgO reveals a typical band at 2127 cm⁻¹ but with less intensity than is observed in the spectrum shown in Fig. 4.2(b). On defect-rich support materials, Au₂₀ adsorbs ¹³CO with vibrational frequencies at 2063 cm⁻¹, 2095 cm⁻¹ (observed as small shoulder), and 2144 cm⁻¹. After initiating the reaction at temperatures above 160 K, CO either desorbs almost totally, or reacts to completion over nanocatalyst supported on a defect-poor film, whereas for Au₂₀ supported on a defect-rich film CO remains adsorbed at these temperatures. These observations concur with the low-

temperature catalysis of the CO oxidation reaction, observed for Au₂₀ clusters supported on defect-poor films. Interestingly, the shift of the main band observed for CO adsorbed on Au₂₀ on defect-poor and defect-rich films is only 15 cm⁻¹ in comparison to 53 cm⁻¹ in the case of Au₈.¹⁴⁹ This correlates with the higher degree of back-donation (substrate-induced charging) for smaller clusters, which is manifested in a larger variation in the stretching frequencies of adsorbed CO molecules.

Theoretical: First-principles DFT calculations for Au₂₀ clusters adsorbed on MgO surfaces were performed to identify cluster structures, electron charge distributions and binding energies. The location of the enhanced charge density is shown to depend sensitively on the characteristics of the underlying metal oxide.

As discussed previously (chapter 1), the interaction between excess charges at the cluster/oxide interface and metal substrate underlies the stabilisation of a planar geometry (Au₂₀(P)) of the gold clusters on thin MgO films. However, for thicker MgO films a tetrahedral structure (Au₂₀(T)) is by far the most stable structure. Since a tetrahedral 3D structure is the most stable configuration for Au₂₀ clusters in the gas-phase, it is likely however, that both 2D and 3D structures are coexisting, and not all of the clusters on thin MgO films have attained in the optimal 2D structure after deposition (Fig. 4.3(a) and (b)).

Similarly, for a thick MgO(100) film containing oxygen vacancies, three possible isomers of the Au₂₀ cluster were considered. One of these isomers is the tetrahedral Au₂₀(T) cluster adsorbed on top of an oxygen vacancy, located near the middle of the base facet of the tetrahedron in Fig. 4.3(c). The next isomers are: a bilayer cluster (Au₂₀(bilayer; FC)) adsorbed on an oxygen vacancy located near the middle of the bottom facet (Fig. 4.3(d)), and a bilayer cluster (Au₂₀(bilayer; 2FC)) adsorbed on top of two neighboring F-centres that are located near the middle of the bottom facet (Fig. 4.3(e)).

Isosurfaces of the excess electron charge distribution (Δq), which is seen to mainly accumulate at the cluster interface to the MgO(1 L)/Mo(100) surface, are also shown in Fig. 4.3. The binding energy of Au₂₀(P) (Fig. 4.3(a)) to the surface is $E_B=12.50$ eV with $\Delta q=1.62$ e, while Au₂₀(T) (Fig. 4.3(b)) is anchored less strongly, with $E_B=5.73$ eV and $\Delta q=1.06$ e. The relaxed structure of Au₂₀(T),

adsorbed on an 8-layer thick MgO film supported on Mo(100) is found to be similar to that shown in Fig. 4.3(b), with $E_B = 3.00$ eV and $\Delta q = 0.73$ e.

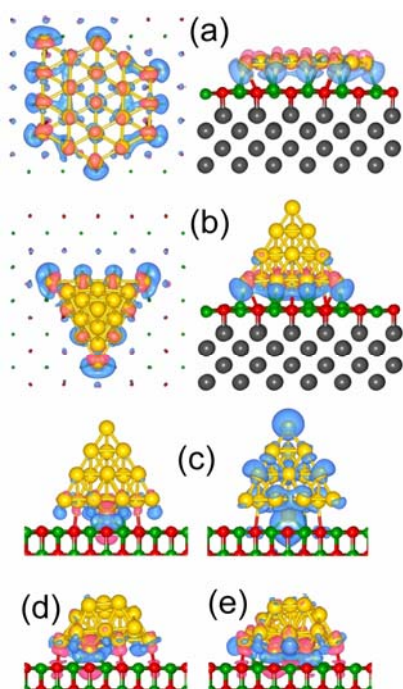


Fig. 4.3: Minimum energy structures of Au₂₀ clusters, adsorbed on MgO surfaces. In (a) and (b) top (left) and side (right) views of a planar and 3D tetrahedral gold clusters on a 1-layer thick MgO layer supported on Mo(100) are depicted, respectively. (c) Illustrating the excess electronic charge distribution (left) and electron density isosurface (right) for a tetrahedral Au₂₀ clusters adsorbed on an F-centre of a thick film. In (d) and (e) a bilayer Au₂₀ clusters located on a single and double surface F-centre (thick film) are shown, respectively.

4.2. Reaction mechanisms of CO combustion on supported Au₂₀ clusters

First-principles quantum calculations were used to elucidate microscopic reaction mechanisms, the low- and high-temperature reactivity of gold clusters observed through TPR investigations for various MgO films. Details of the theoretical calculations are thoroughly described elsewhere.¹⁵⁰ Thus, in the following, theoretical results corresponding to the experimental measurements are presented.

4.2.1. Low-temperature mechanisms on thin defect-poor MgO films

In the reaction mechanism for CO₂ formation at temperatures below ~200 K on thin MgO films (1 L), both 2D and 3D Au₂₀ clusters are involved (Fig. 4.1(b-d)). One of the reaction profiles that is active for both cluster configurations can be explained as follow: i) dissociative adsorption of an O₂ molecule at the location

of the highest charge accumulation, namely, the interface between the Au₂₀(P) cluster and the MgO surface as well as the interfacial periphery of the Au₂₀(T), ii) reaction between dissociated O₂ and a CO molecule adsorbed on the MgO surface with a negligible energy barrier, iii) desorption of an adsorbed CO₂ intermediate with low energy barrier, ~0.27 eV and 0.31 eV for 2D and 3D structures, respectively. In Fig. 4.4(a) this reaction pathway is illustrated for 2D clusters adsorbed on a one layer thick MgO film.

It is important to remark here, that the reaction mechanism under experimentally CO-poor conditions (O₂ adsorbed prior to CO) involves the non-reactive reverse spill-over of a molecularly surface adsorbed CO molecule towards cluster catalysts (Langmuir-Hinshelwood mechanism). Whereas, under CO-rich conditions a CO molecule adsorbs directly onto the gold cluster, and reacts with a pre-adsorbed peroxo-activated O₂ molecule leading to the formation of CO₂.

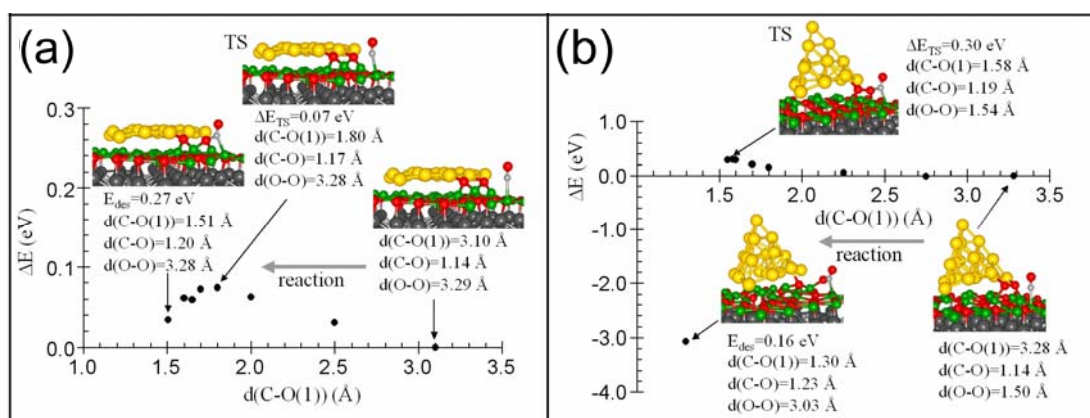


Fig. 4.4: Illustrating low-temperature reaction pathways for (a) an adsorbed planar, Au₂₀(P) cluster, and (b) an adsorbed 3D Au₂₀(T) cluster adsorbed on a one layer thick MgO film. Color designation: Mg in green, O in red, Au in yellow, C in light gray.

In other active channels at low temperatures on Au₂₀(T)/MgO(1 L)/Mo, a molecularly adsorbed oxygen at the interfacial periphery that is activated to a peroxo state, and a CO molecule on the MgO surface are involved. Formation of the CO₂ intermediate entails a barrier of ~0.3 eV with a subsequent desorption energy of ~0.16 eV, as shown in Fig. 4.4(b).

4.2.2. High-temperature mechanisms on thin defect-poor MgO films

A relatively high transition state barrier was calculated for the formation of a CO₂ (~0.66 eV) when a surface-adsorbed CO molecule (proximal to the gold cluster) reacts with an activated, but undissociated, periphery-adsorbed oxygen on Au₂₀(P)/MgO(1 L)/Mo model catalyst (Fig. 4.5(a)). Note that for this case two CO molecules are considered. Formation of a second adsorbed CO molecule *via* reaction of the second CO molecule with the remaining O atoms was found to occur with no activation barrier, but the formation of gaseous CO₂ entails a relatively high desorption energy (0.60 eV). Since one of the O atoms of adsorbed CO₂ molecule is bound also to Mg atom of the magnesia surface, which accounts for the somewhat elevated desorption energy of the product molecule. Another reaction channel that also entails a high activation barrier (~0.58 eV) was found for the tetrahedral clusters (CO/O₂/Au₂₀(T)/MgO(1 L)/Mo), where an oxygen molecule is bound to the periphery of the cluster. The O₂ molecule is in a peroxy-activated state and interacts with a CO molecule adsorbed onto a second layer of the 3D gold cluster (see Fig. 4.3(b) for the location of excess charge accumulation). The estimated desorption energy (required for the formation of a gaseous CO₂ product) is about $E_{\text{des}} = 1.06$ eV (Fig. 4.5(b)). This rather high desorption energy is attributed to the strong bonding between an oxygen atom of the CO₂ molecule and the magnesia surface (Fig. 4.5(c)). The excess accumulation of electronic charge originating from the underlying metal support (Mo(100)) may also lead to the enhancement of the bonding.

An expanded view of the desorbing CO₂ molecule showing a configuration with the carbon bonded to the gold cluster and one of the oxygen atoms bonded to two Mg surface sites is displayed in Fig. 4.5(c).

4.2.3. Reaction mechanisms on thick defect-poor MgO films

For thick films, the influence of the underlying substrate on the reactivity is markedly reduced. Thus, it is obvious that the reaction and exit barriers of CO₂ formation on Au₂₀(T)/MgO(8 L)/Mo system are also decreased in comparison to the thin film systems. The reaction between an adsorbed O₂ in a peroxy-activated state and a CO molecule bonded to a gold atom in the second layer of

the cluster leads to a CO₂ formation with a low reaction barrier (0.14 eV) and a very small exit barrier (Fig. 4.5(d)).

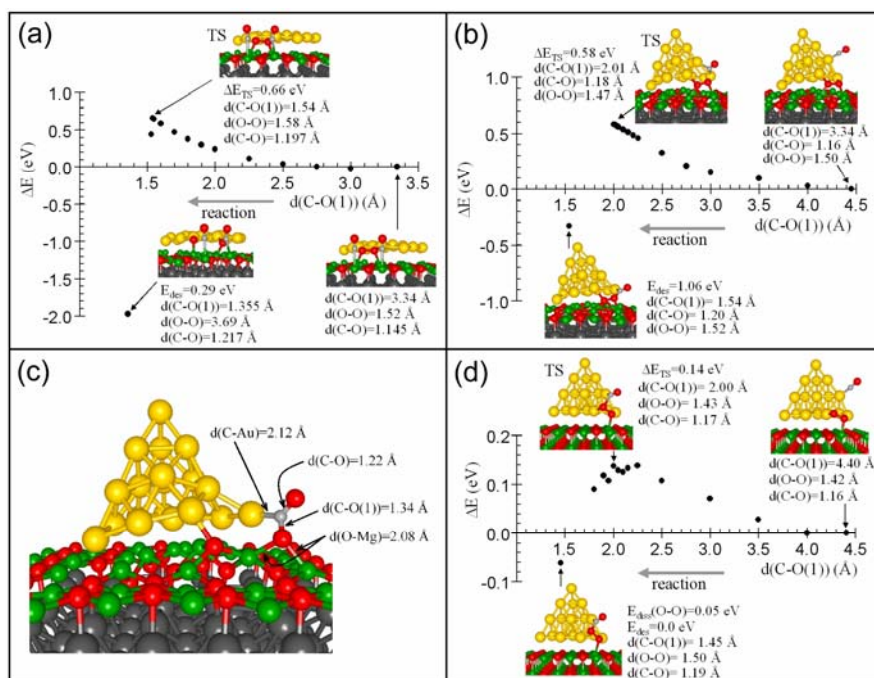


Fig. 4.5: Reaction pathways of the catalytic ¹³CO combustion on: (a-c) a thin defect-poor MgO film, (d) an 8-layer thick defect-poor film (see text).

4.2.4. Reaction mechanisms on thick defect-rich MgO films

On a thick defect-rich MgO(100) surface, the influence of underlying metal support is negligible and therefore the binding nature of the adsorbed 3D clusters on defect sites plays an essential role on reaction mechanisms. In the experimental data shown for this system (Fig. 4.2(c)), the broad distribution of the reactivity (the smaller peak at ~210 K and the main broad distribution peaking at ~400 K) can be correlated with the multiplicity of the cluster structures that coexist on thick surfaces. These competing configurations differ from each other by the isomeric structures (tetrahedral or bilayer) of the adsorbed nanoclusters and the nature of the cluster bindings to the surface. In particular, the anchoring of clusters to single or double (nearest-neighbour) surface oxygen vacancy defects are considered here (see Fig. 4.3(c-e)).

Reaction mechanisms on a tetrahedral gold cluster adsorbed on a single FC defect, located under the middle of the bottom facet of the cluster, ($E_{\text{B}}[\text{Au}_{20}(\text{T})] = 4.36 \text{ eV}$) entail interaction of an O₂ molecule bound to the top apex gold atom

of the Au₂₀(T) cluster, with a CO molecule present on the cluster tetrahedral ($E_B(\text{CO}) = 0.54$ eV). This reaction pathway possesses relatively low TS barrier of 0.41 eV with a barrierless desorption of the product CO₂ molecule (Fig. 4.6(a)).

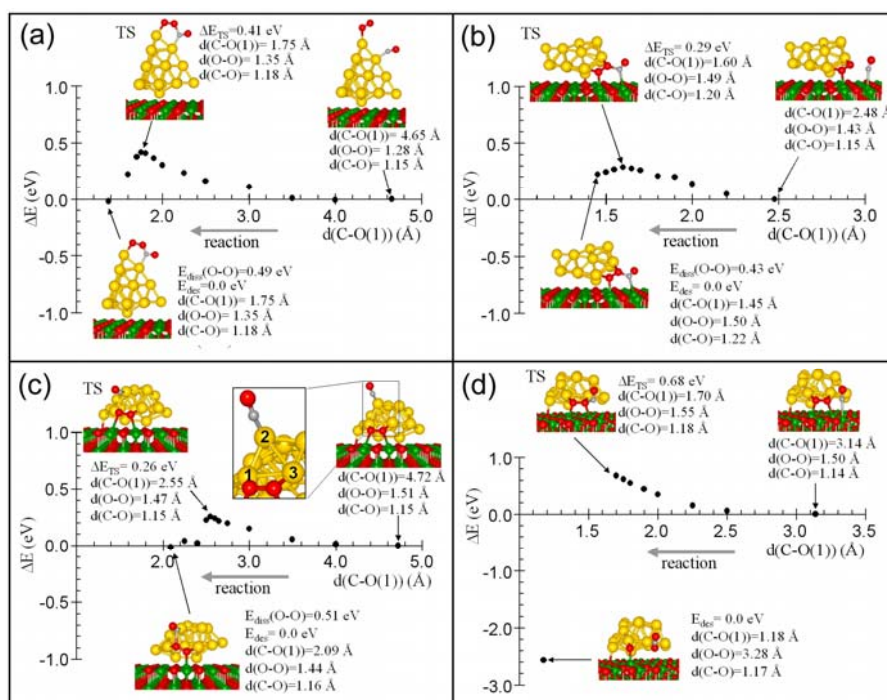


Fig. 4.6: Reaction pathways for Au₂₀ clusters adsorbed on surface oxygen vacancies (F-centres) on thick MgO(100) surfaces supported on Mo(100), corresponding to the experimental data displayed in Fig. 4.2(c) (see text).

The CO combustion reaction catalysed by bilayer Au₂₀ isomers, anchored either on a single FC defect ($E_B[\text{Au}_{20}(\text{bilayer})] = 4.92$ eV) or on top of two neighboring oxygen vacancies ($E_B[\text{Au}_{20}(\text{bilayer})] = 7.93$ eV) are illustrated in Fig. 4.6(b) and (c), respectively. In both cases, the reaction starts from a peripherally adsorbed peroxy-activated O₂ molecule with a surface adsorbed CO molecule ($E_B(\text{CO}) = 0.29$ eV) for the former isomer (Fig. 4.6(b)), and an adsorbed CO on the bilayer gold cluster ($E_B(\text{CO}) = 0.81$ eV) for the latter isomer (Fig. 4.6(c)). The transition state barrier (TS) for the formation of an adsorbed CO-O₂ complex is 0.29 eV and 0.26 eV for clusters adsorbed on a single and double FC defects, respectively. Subsequent dissociation of the inter oxygen bond between the complex and the oxygen of a reactanting O₂ molecule entails an activation energy of either $E_{\text{diss}}[\text{O-O}] = 0.43$ eV or 0.51 eV depending on the underlying single and double defect sites. In Fig. 4.6(c), the dynamical fluxionality, one of

the key principles of nanocatalysis, occurs by distortion of the metal clusters in the course of the oxidation reaction. This is manifested by variation of the formed angle between the three marked Au atoms from $\theta(123) = 59^\circ$ to 79° in order to attain minimum-energy configurations. These structural variations serve to enhance the adsorption of the reactants and to lower the activation barriers for reactions between the adsorbed reactants.

In Fig. 4.6(d) another reaction profile of the bilayer gold cluster adsorbed on a single surface FC (as in Fig. 4.6(b)) is shown. The combustion starts from a peripherally adsorbed, peroxy-activated O_2 molecule ($E_B(O_2) = 0.96$ eV), and a surface adsorbed CO molecule ($E_B(CO) = 0.27$ eV). The reaction involves a TS energy barrier of 0.68 eV, whilst the breakup of the transition state complex resulting in desorption of the product CO_2 molecule to occur with no energy barrier.

4.3. Summary

The oxidation of CO on Au_{20} depends sensitively on both the thickness of the MgO film grown on a Mo(100) single crystal, and the metal-oxide stoichiometry. These dependencies are reflected in variations of the reaction temperatures observed in temperature programmed reaction (single-heating-cycle) experiments, as well as in the amount of CO_2 produced. The first-principles theoretical investigations presented here show that the observed changes in reactivity may be correlated, in part, with a dimensionality crossover from 3D tetrahedral Au_{20} in the case of thick films (≥ 8 ML) to 2D planar structures for film thicknesses of less than ~ 3 ML.

Underlying the aforementioned structural and dimensionality variations is the enhanced charge transfer from the Mo surface through the metal-oxide occurring for the thinner films. This transferred charge mainly accumulates at the interfacial region between the adsorbed metal cluster and the metal-oxide, and leads to the stabilisation of planar configurations of the cluster through attractive charge interactions that increase the cluster/oxide contact area.⁵² On one hand, the excess charge can enhance the catalytic activity of the adsorbed (partially charged) gold clusters (both 3D and 2D), *via* transfer of charge to adsorbed reactant molecules.¹⁵¹ For example, the activation of an adsorbed O_2 through the population of the $2\pi^*$ antibonding orbital, forms a superoxo- or

peroxo- activated molecule, which can react with CO in a Langmuir–Hinshelwood mechanism with a lower activation barrier. On the other hand, the excess interfacial charge accumulation for thin metal-oxide films may enhance the binding strength of reaction intermediates and/or adsorbed product molecules, therefore increasing the exit reaction barriers. Such reaction mechanisms have been illustrated in this study for both 2D and 3D Au₂₀ nanoclusters adsorbed on thin MgO(1 L)/Mo(100).

For thick films and 3D Au₂₀ adsorbed clusters (both tetrahedral and bilayer isomeric structures), charge accumulation and concomitant charging of adsorbed clusters, can be induced by defect sites with Lewis base character (e.g. oxygen vacancies, F-centres). This charge accumulation is local and depends on the type of electron donor. In both cases, charging through thin metal-oxide films and F-centre-induced charging, results in excess charge mainly found around the perimeter atoms of the 2D or 3D adsorbed Au₂₀ clusters. Furthermore, in the case of a 3D tetrahedral Au₂₀(T) cluster anchored to a MgO surface F-centre, the highest occupied Kohn-Sham orbital exhibits an enhanced electronic density, localised on the top apex atom of the tetrahedron. This charge accumulation defines the location of the reactive site on the cluster, and consequently its reactivity can be tuned as a function of the properties (thickness and stoichiometry) of the supporting metal-oxide film.

Chapter 5

5. Catalysis of oxygen treated palladium cluster catalysts

Since the early days of heterogeneous catalysis (using active metal clusters), designing cluster-based catalysts with specific functions has always been a key goal of many research groups.¹ In chapter 1, various ways to manipulate and control the catalytic activity of the cluster catalysts were introduced in more detail. In this context, the pretreatment of catalysts, which may lead to a structural modification and different degree of interaction between the active metal component and substrate, was found to influence/alter catalytic properties of catalytic systems.¹⁵² Moreover, to optimise the efficiency and reactivity of the model catalyst, the energetic and mechanistic understanding of molecular-scale catalytic reactions is required. Despite the technological importance of cluster catalysts, little is known about possible structural variation of metal clusters in the real chemical environment.

The molecular beam experiments have demonstrated that on the outer surface of Pd nanoparticles and at Pd/Fe₃O₄ interfaces, size-dependent oxide-clusters may form (~2-100 nm).¹⁵³ Furthermore, a recent interesting density functional study suggested that small Pd clusters up to 9 atoms deposited onto magnesia (F-centres) can be transformed to nano-oxides (Pd_xO_y) upon reaction with molecular oxygen.⁴⁸

In this chapter, one of the most studied catalytic reactions, the CO combustion to CO₂, on supported-palladium clusters will be addressed. In contrast to the earlier studies,^{103,107,154} many later investigations on single crystal supported thin oxide films, revealed distinct size- and support- dependency in CO oxidation reaction rates and kinetics over Pd, Pt, Rh and Au clusters based catalysts.^{108,155,156}

Experimentally, variation in reactive sites, structural rearrangements, catalytic activities, and ionisation potentials of cluster catalysts upon reaction with oxygen (oxygen pretreatment) can be verified using TPR, FTIR, and MIES techniques.¹⁵⁷

TPR experiments are one of the fundamental tools in catalysis, which have been widely used to study surface reactivity, desorption and decomposition processes, and reaction mechanisms. The relative low cost and simplicity of the experimental equipment has further triggered development of new microscopic models for the analysis of the TPR spectra, which include adsorbate-adsorbate interactions, and energy distribution of the active sites (see § 3.2).

The usefulness of the FTIR method in surface science, as a tool for investigating adsorbed molecules and their interactions with the substrate was originally demonstrated by Eischens. *et al.*¹⁵⁸ and Baddour *et al.*¹⁵⁹. In these early works, the appearance of several adsorbed CO bands on supported transition metals (Ni, Pd, Pt) were attributed to the linear (a carbon atom is bonded to a single metal atom) and bridging (a carbon atom is bridged between two adjacent metal atoms) adsorption sites of a CO molecule in analogy to the IR spectra of the bulk metal carbonyls. Additionally, frequency shifts as a function of adsorbate coverage were assigned to the intermolecular vibrational dipole coupling. The variation in the IR band shapes was also believed to be due to the structural rearrangement of the metal particles under catalytic conditions.¹⁶⁰

The experimental TPR and FTIR investigations presented in this chapter aim at determining the structural modifications, catalytic properties, and reaction mechanisms of O₂ and ¹³CO treated Pd cluster catalysts.

5.1. Reactivity of oxygen treated Pd₁₃ clusters

As described in chapter 2, model catalysts were prepared by deposition of size-selected clusters (Pd₁₃, Pd₃₀, ~(0.17-0.2)% ML at ~100 K) onto oxide films. In the experiments reported here, defect-poor MgO films with coverage of ~8-10 ML were grown onto a Mo(100) single crystal (T~300 K, P_{oxygen} = 5 × 10⁻⁷ mbar) (see § 3.1 for corresponding AES and MIES spectra). Exploration of the catalytic activity of the Pd based catalysts (Pd₁₃, Pd₃₀ clusters) after oxygen pretreatment at different temperatures was carried out with various types of TPR schemes.

In detail, the formation of CO₂ was monitored over oxygen-treated palladium cluster catalysts during a temperature ramp from ~100 to ~750 K after exposing the catalyst to CO or O₂ and CO (coadsorption). Oxygen pretreatment was

performed at temperatures between ~370 and ~550 K in an oxygen background of about 5×10^{-7} mbar for one minute. For these TPR studies, isotopically labelled carbon monoxide (¹³CO) were used in order to increase the signal-to-noise ratio by reducing the ¹²C¹⁶O₂ background contribution. Furthermore, employing two different oxygen isotopes for oxidation at high temperature (¹⁶O₂) and low temperature dosage (¹⁸O₂, ~120 K) prior to reaction, may allow identifying possible reactions pathways for CO combustion on the oxygen-treated palladium cluster catalysts. In the TPR experiments with both reactant gases (O₂ and ¹³CO), they were sequentially administered to the surface by using a molecular beam doser (MBD); in the experiments shown here ¹⁸O₂ was dosed prior to ¹³CO. The MBD was calibrated and thus a known amount of reactant molecules could be dosed (see § 2.2.4).

5.1.1. TPR type I

In this simple type of TPR, size-selected clusters were first annealed in an oxygen background ($T = \sim 370$ K, $P_{\text{oxygen}} = 5 \times 10^{-7}$ mbar) subsequent to cluster deposition. Fig. 5.1 depicts type I TPR spectrum made on Pd₁₃ (~0.15% ML) clusters with ¹³CO molecules dosed to the surface at ~120 K.

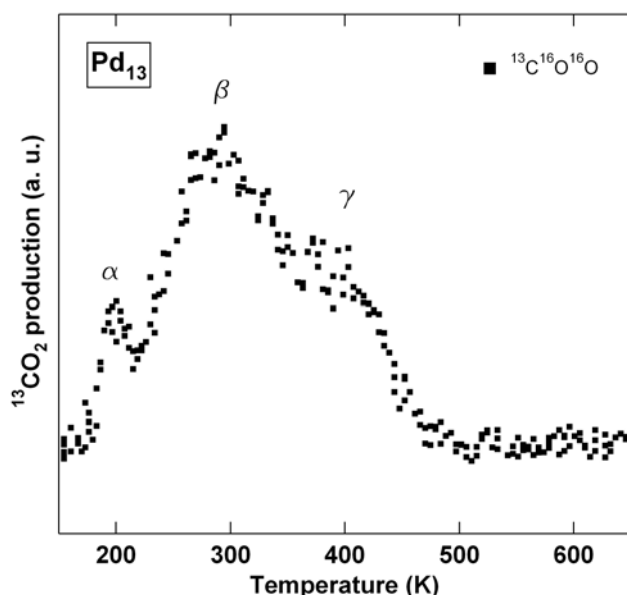


Fig. 5.1: Illustrating ¹³C¹⁶O₂ formation on Pd₁₃ clusters. The oxygen pretreatment step was made at ~370 K in a ¹⁶O₂ atmosphere. TPR experiment was performed with ¹³C¹⁶O starting at ~120 K.

The spectrum clearly reveals three different ¹³CO₂ formation temperatures, with a maximum reactivity peaked at ~200, ~300, and ~400 K (observed shoulder), which are labelled as α , β and γ , respectively. In order to distinguish between

the role of oxygen in palladium-oxide species and the oxygen adsorbed at ~120 K, isotopic labelling experiments were performed (see § 5.1.2).

5.1.2. TPR type II

To explore the presence and role of various chemisorbed oxygen sites as well as the formation of possible nano-oxide species, different oxygen isotopes were used. Isotopically labelled ¹³C¹⁶O₂ production catalysed on ¹⁶O₂ treated Pd₁₃ (~0.15% ML) catalysts using type II TPR experimental scheme is illustrated in Fig. 5.2. The oxygen pretreatment step was made at ~370 K in a ¹⁶O₂ atmosphere and the reactant gases (¹⁸O₂, ¹³CO) were coadsorbed on the prepared catalyst at ~120 K. The TPR spectra show one major reactivity peak for the ¹³C¹⁶O₂ isotopomer peaked at ~340 K and two active channels at ~210 K and ~330 K for the ¹³C¹⁸O¹⁶O isotopomer (Fig. 5.2). The presence of the low-temperature α -mechanism only in the spectrum of ¹³C¹⁸O¹⁶O isotopomer, suggests that ¹⁸O₂ is intensively involved in this reaction. This implies that the oxygen responsible for this reaction mechanism (α species) is weakly bound (molecularly) and not stable during the oxygen pretreatment at ~370 K. Thus, the empty α -sites are occupied by ¹⁸O₂ during the oxygen dosage at ~120 K.

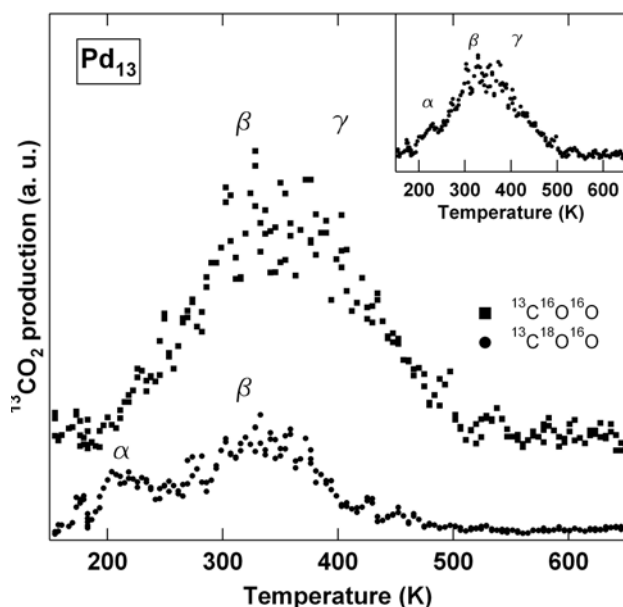


Fig. 5.2: TPR spectra of ¹³CO oxidation on Pd₁₃ clusters deposited onto an MgO film. The Pd clusters were annealed at ~370 K in a ¹⁶O₂ atmosphere; the reactant gases (¹⁸O₂ and ¹³CO) were sequentially dosed to the surface at ~120 K. A temperature ramp was performed from ~120 K to ~750 K. Possible reaction products are shown with ■ (¹³C¹⁶O¹⁶O) and ● (¹³C¹⁸O¹⁶O) markers. The inset illustrates the sum of the two spectra.

As no ¹³C¹⁶O¹⁸O isotopomer are seen in the spectra at temperatures above ~400 K, we exclude the isotopic scrambling for the γ -mechanism at high temperatures. On the other hand, at intermediate temperatures (β -mechanism)

both isotopomer were detected. This behaviour is consistent with a mechanism similar to the low-temperature reaction mechanism (α -mechanism), where some of the β -sites become empty and are then filled with $^{18}\text{O}_2$. As a consequence, the mixture of adsorbed ^{16}O and ^{18}O react with ^{13}CO . In the β -mechanism, isotopic scrambling may also occur upon reaction. Furthermore, the sum of the two spectra (inset spectrum) is similar to the one seen in figure 5.1 with decreased intensity in the temperature range below 300 K. To get further insight into these observations, additional experiments have been performed.

5.1.3. TPR type III

In this type of TPR experiment, the Pd clusters were first annealed at ~ 370 K in a $^{16}\text{O}_2$ atmosphere (5×10^{-7} mbar); subsequently the sample was heated to ~ 460 K in order to investigate the thermal stability of the oxide species. Prior to the TPR, the reactant gases were sequentially administered at ~ 120 K to the surface (first $^{18}\text{O}_2$ then ^{13}CO). The resulting TPR of the two possible $^{13}\text{C}^{16}\text{O}_2$ and $^{13}\text{C}^{16}\text{O}^{18}\text{O}$ products, performed on Pd₁₃ based catalysts, are depicted in Fig. 5.3. The TPR spectrum for the $^{13}\text{C}^{16}\text{O}^{18}\text{O}$ isotopomer shows two single peaks with the maxima at ~ 210 and ~ 330 K (α - and β - mechanisms similar to the previous observations) and a shoulder in the temperature range of the γ -mechanism. Furthermore, the relative intensity of the β -peak of the $^{13}\text{C}^{16}\text{O}^{18}\text{O}$ isotopomer has increased indicating that the annealing enhances the number of the free β -sites. On the other hand, the $^{13}\text{C}^{16}\text{O}_2$ isotopomer illustrates a main CO_2 production peaked at ~ 410 K. This is attributed to the higher thermal stability of oxygen species involved in the γ -mechanism (up to ~ 450 K) in comparison to the adsorbed oxygen on the other active species. Most importantly, the $^{13}\text{C}^{16}\text{O}_2$ isotopomer is still produced *via* the β -mechanism. This implies that isotopic scrambling to occur during the reaction step, which may be induced by an oxygen exchange from the γ -site to the β -site. Thus, γ -oxygen may serve as an oxygen reservoir for the β -mechanism.

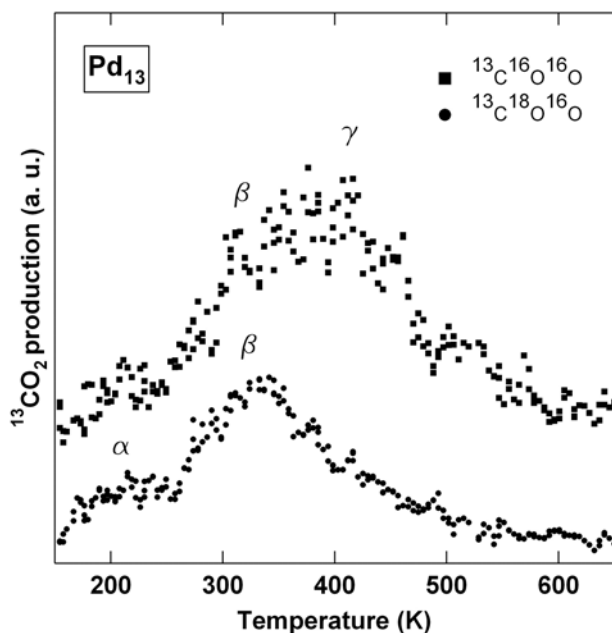


Fig. 5.3: Illustrating TPR spectra of ¹³C¹⁶O¹⁶O (■) and ¹³C¹⁸O¹⁶O (●) formation on Pd₁₃ clusters (0.17 % ML) deposited onto an MgO film. Catalysts were first annealed at ~370 K in a ¹⁶O₂ atmosphere (5×10^{-7} mbar) then heated to ~460 K; followed by a TPR run with ¹⁸O₂ and ¹³CO starting from ~120 K.

It is noteworthy to mention here that similar results were obtained with model catalysts consisting of larger clusters (see § 5.2).

Finally, the chemical reactivity and the thermal stability of the Pd₁₃ model catalyst in an oxygen atmosphere were investigated further by performing the oxygen treatment at higher temperatures. To this end, the cluster catalysts (Pd₁₃, ~0.17% ML) were initially, annealed at ~550 K in ¹⁶O₂ for one minute; ¹³CO was then dosed onto the surface and during a temperature ramp (~120 - 750 K), ¹³C¹⁶O₂ molecules were detected.

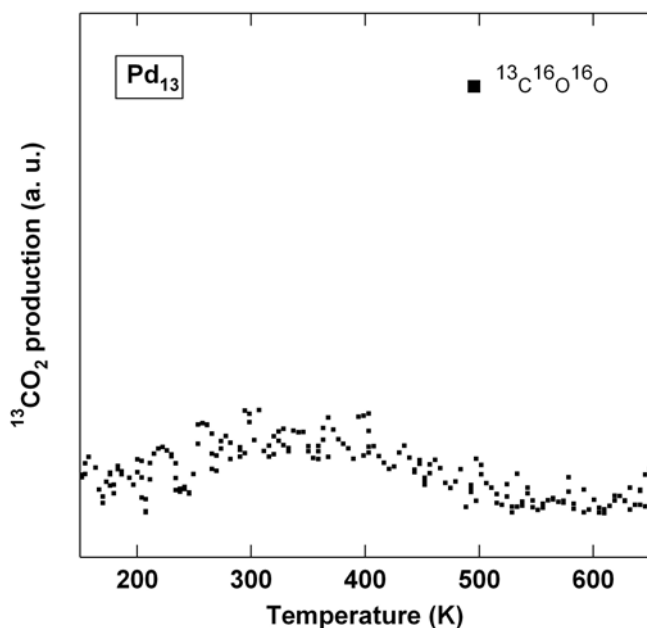


Fig. 5.5: Showing TPR spectrum (type I) of ¹³C¹⁶O₂ formation on Pd₁₃ cluster catalysts (~0.17% ML). The oxygen treatment step was made at ~550 K. A temperature ramp was made after ¹³CO dosage at ~120 K.

Under these experimental conditions hardly any carbon dioxide is formed (Fig. 5.5) indicating that palladium oxide is either not stable or that the clusters and/or

cluster-oxides diffuse on the surface and form large nanoparticles with a drastically reduced density of surface reactive sites in comparison to the highly dispersed Pd₁₃ clusters (changing surface-to-bulk ratio). Observed instability of the model catalysts has also been seen in independent pulsed-molecular beam reactive scattering experiments, in which the measured turnover frequencies (TOF's) drastically deviate from those calculated by microkinetic models (not including cluster diffusion steps) at temperatures around ~500 K.⁶¹

5.2. Reactivity of oxygen treated Pd₃₀ cluster catalysts

To explore possible size-dependent mechanistic details in the CO oxidation on small clusters, similar TPR experiments were carried out for Pd₃₀ model catalysts (~0.17% ML). To this aim, TPR schemes of type I and type III were applied.

The ¹³C¹⁶O₂ formation in a TPR experiment of type I (Fig. 5.6), where clusters were treated in oxygen (¹⁶O₂) at ~370 K prior to carbon monoxide exposure at ~180 K, is dominated by the β-mechanism. The γ-mechanism occurs at slightly lower temperatures when compared to Pd₁₃. Note the absence of the α-mechanism, which is due to the dosage of carbon monoxide at ~180 K. In fact, this mechanism (α) also takes place on Pd₃₀ cluster catalysts as shown in Fig. 5.7.

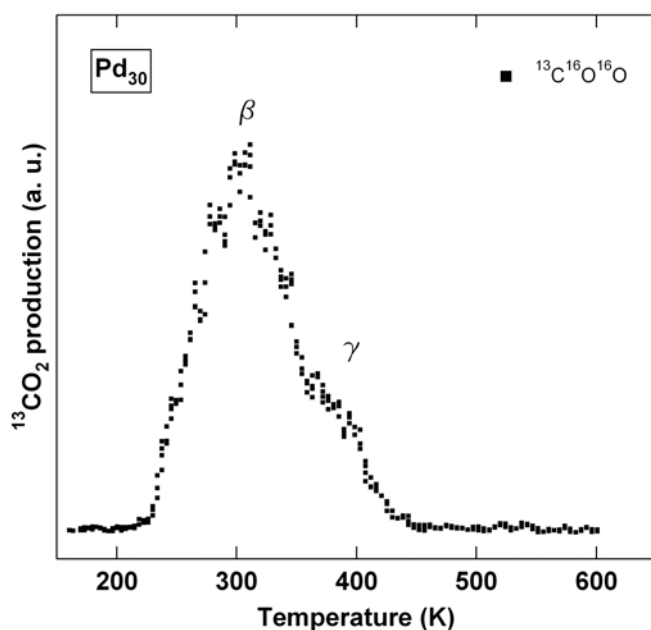


Fig. 5.6: Showing TPR spectrum (type I) of ¹³C¹⁶O₂ formation on Pd₃₀ clusters (~0.17% ML). Oxygen treatment was made at ~370 K. Temperature ramp (~120 K to ~600 K) was performed after ¹³CO dosage at ~180 K.

Similarly to Pd₁₃, the Pd₃₀ cluster catalyst was investigated by TPR experiments of type III. Surprisingly, the overall formation of CO₂ is dominated by γ -mechanism and the sum of the two spectra does not reflect the one depicted in figure 5.6. The β -mechanism, which was dominant after annealing the catalysts to ~ 370 K, is manifested in a small peak in the $^{13}\text{C}^{18}\text{O}^{16}\text{O}$ spectrum and a small shoulder in the $^{13}\text{C}^{16}\text{O}_2$ spectrum. Obviously, the thermal treatment at ~ 450 K lowered the number of β -sites either through a change of the Pd₃₀ cluster upon heating or a transformation of the β -sites into γ -sites. The transformation could be indicative of the formation of a more stable palladium-oxide at higher temperatures. Furthermore, a new reaction mechanism, δ , is observed above ~ 500 K, in which $^{13}\text{C}^{16}\text{O}_2$ is only formed.

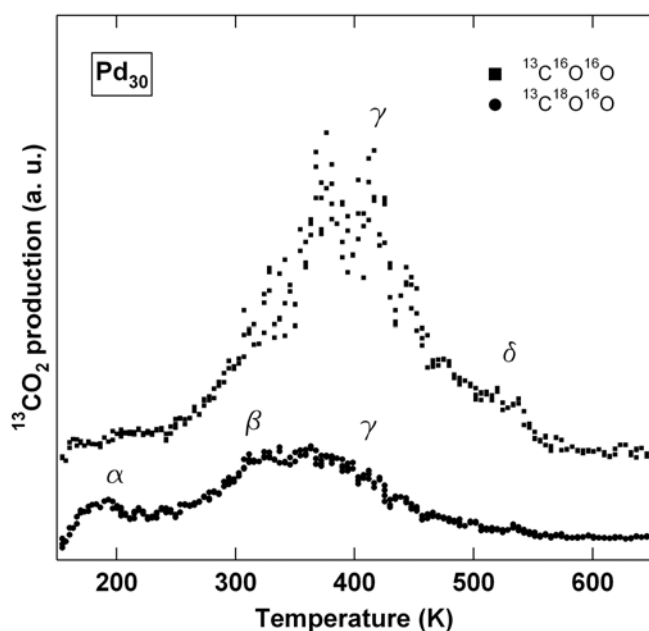


Fig. 5.7: Illustrating TPR spectra of $^{13}\text{C}^{16}\text{O}^{16}\text{O}$ (■) and $^{13}\text{C}^{18}\text{O}^{16}\text{O}$ (●) formation on Pd₃₀ clusters ($\sim 0.17\%$ ML) deposited onto an MgO film. Catalysts were first annealed at ~ 370 K in a $^{16}\text{O}_2$ atmosphere (5×10^{-7} mbar) then heated to ~ 460 K; followed by a TPR with $^{18}\text{O}_2$ and ^{13}CO starting from ~ 120 K.

5.3. FTIR investigations of palladium clusters

In these experiments, carbon monoxide serves as probe molecule to further characterise the clusters in the oxidised and reduced states. The ^{13}CO isotopomer was used to increase the signal-to-noise ratio of the FTIR measurements. For the oxidation and reduction step, the cluster catalysts were annealed at ~ 370 K in an O₂ or a ^{13}CO background of 5×10^{-7} mbar for 30 s. Subsequently, the model catalyst was saturated with ^{13}CO at ~ 110 K and the FTIR spectra were recorded. For all the FTIR measurements presented here,

the clusters were oxidised in a first step; the reduction of the catalyst was performed at ~ 370 K for 30 s in a ^{13}CO background; based on the reactivity results (§ 5.2), CO oxidation through β -mechanism occurs at these temperatures. Thus by re-dosing probe molecules and re-measuring the FTIR spectrum, it may be feasible to obtain information pertaining possible variations in the adsorption sites corresponding to the structural modifications. In all the measurements presented here, a background spectrum was recorded prior to the ^{13}CO dosage.

In the following, IR spectra of the size-selected and unselected palladium cluster catalysts, illustrated by the transmittance (%T) over a frequency range of $2300\text{-}1700\text{ cm}^{-1}$ will be discussed.

5.3.1. Pd_9 cluster catalysts

The vibrational bands of the adsorbed ^{13}CO on Pd_9 clusters ($\sim 0.2\%$ ML) are investigated directly after annealing the catalyst either in an oxidised or a reduced atmosphere. In Fig. 5.8 (a), main absorption band at 2063 cm^{-1} is observed for oxygen-treated catalyst. A small band at 1891 cm^{-1} is attributed to bridge bonded CO. Following the annealing of the catalyst in a ^{13}CO background (Fig. 5.8(b)), a shift of 15 cm^{-1} is seen in CO absorption band (2048 cm^{-1}) in comparison to the spectrum (a).

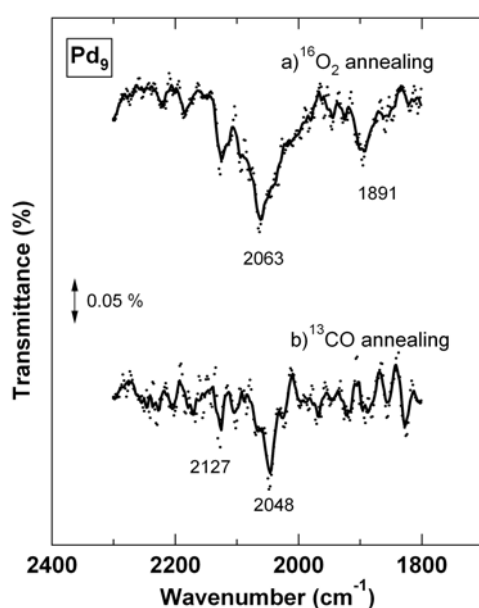


Fig. 5.8: IR spectra of ^{13}CO adsorbed on Pd_9 clusters after annealing the sample at ~ 370 K in different atmospheres (O_2 and ^{13}CO). The markers represent the raw data points and the solid line a smoothed data

5.3.2. Pd₁₃ cluster catalysts

The characteristic FTIR spectra of adsorbed ¹³CO, which were recorded following alternate oxygen and carbon monoxide treatments of the Pd₁₃ catalyst (~0.4% ML) are depicted in Fig. 5.9 (a-c). The collated spectra represent various absorption bands at 2068/2067 and 2052 cm⁻¹ for O₂ and ¹³CO treated sample, respectively. The observed shifts are rather small; however, results imply that the oxidation and reduction cycles are reversible. Note the broad absorption band at lower wavenumbers (1886 cm⁻¹) in the spectrum (c) (quite similar to the band observed for the Pd₉ clusters) is typical for bridge-bonded CO.

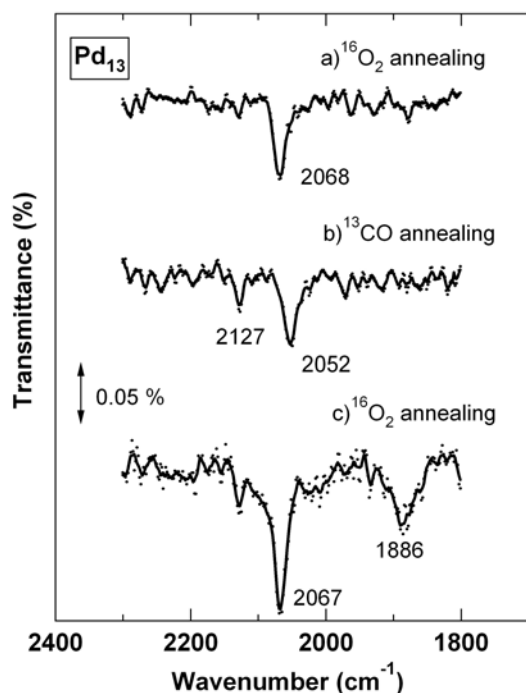


Fig. 5.9: Showing FTIR spectra of adsorbed ¹³CO on oxygen and CO treated Pd₁₃ clusters acquired at ~110 K. Oxygen and CO treatments were performed at ~370 K. Markers represent the experimental data points and the solid line a smoothed data.

5.3.3. Pd₃₀ cluster catalysts

In figure 5.10, a series of FTIR spectra for Pd₃₀ (~0.4% ML) clusters are shown, recorded after annealing cycles in ¹⁶O₂ and ¹³CO at ~370 K. In the former case, ¹³CO reveals a distinct band at 2076 cm⁻¹ and a small absorption at ~2146 cm⁻¹ (spectrum (a) and (c)). Additionally, the ¹³CO spectrum of the partly reduced catalyst (spectrum (b)) indicates vibrational frequencies of 2071 and 2052 cm⁻¹. Again, the oxidation and reduction cycles are reversible. Note that metallic Pd₃₀ clusters reveal characteristic bands at ~2055 and ~1930 cm⁻¹.¹⁶¹ The oxygen

treated sample exhibits a blue-shift of $\sim 20 \text{ cm}^{-1}$ for the atop bound ^{13}CO , whereas the reduced sample reveals a shift of just $\sim 3 \text{ cm}^{-1}$. Nevertheless, no bridge-bonded ^{13}CO is observed in either case. This suggests that the reduction is not complete and certain adsorption sites are still occupied by oxygen.

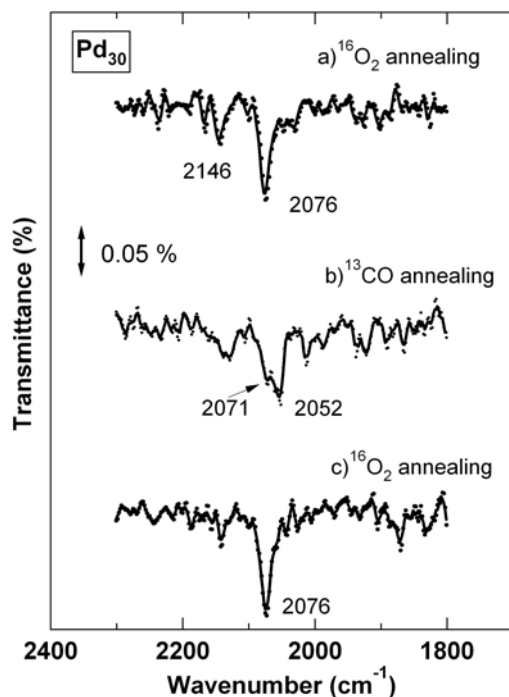


Fig. 5.10: Showing FTIR spectra of adsorbed ^{13}CO molecules on oxygen- and CO-treated Pd_{30} clusters acquired at $\sim 110 \text{ K}$. Oxygen and CO treatments were performed at $\sim 370 \text{ K}$ in an $^{16}\text{O}_2$ and a ^{13}CO atmosphere ($5 \times 10^{-7} \text{ mbar}$), respectively. Markers represent the experimental data points and the solid line a smoothed data.

5.3.4. Pd_n cluster catalysts

Further studies were made on a model catalyst with $\sim 1\%$ ML ($1 \text{ ML} = 2.25 \times 10^{15} \text{ clusters/cm}^2$) size-distributed Pd cluster, to minimise adsorption sites on the support material. IR spectra of adsorbed ^{13}CO on O_2 and CO treated palladium clusters (Pd_n , $n \geq 30$) are shown in Fig. 5.11. The top spectrum indicates a typical atop CO absorption band at 2081 cm^{-1} , and CO treated catalyst (spectrum (b)) shows two bands on atop and bridge positions at 2060 cm^{-1} and 1956 cm^{-1} , respectively.

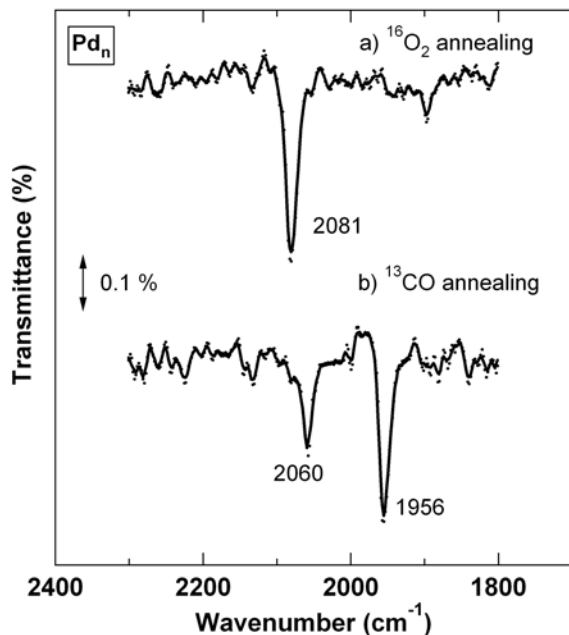


Fig. 5.11: IR spectra of ^{13}CO adsorbed on Pd_n clusters after annealing the catalyst at ~ 370 K in an oxidised and a reduced atmosphere. Markers represent the experimental data points and the solid line a smoothed data.

The frequencies of the vibrational bands for the O_2 and CO treated as well as metallic size-selected clusters are summarised in table 5.1.

	O_2 treated	CO treated	Metallic
Pd_9	2063, 1896	2048	2037, 2014, 1893(Pd_8)
Pd_{13}	2068	2052	-----
Pd_{30}	2076	2052	2055, 1930

Table 5.1: Stretching frequencies (cm^{-1}) of adsorbed ^{13}CO on various size-selected Pd clusters in three different indicated forms; obtained from experimental results.

Finally, figure 5.12 shows the ^{13}CO FTIR spectra of an oxidised Pd_{13} clusters upon heating at conditions similar to the type I TPR experiment. The lower spectrum was collected after reduction in ^{13}CO at ~ 370 K. The absorption band at 2068 cm^{-1} on oxidised catalyst is attenuated by increasing temperature and at ~ 235 K is not observed at all. The latter is attributed to complete desorption and/or reaction with remaining oxygen species. A reduced catalyst shows a blue-shifted absorption band at 2052 cm^{-1} .

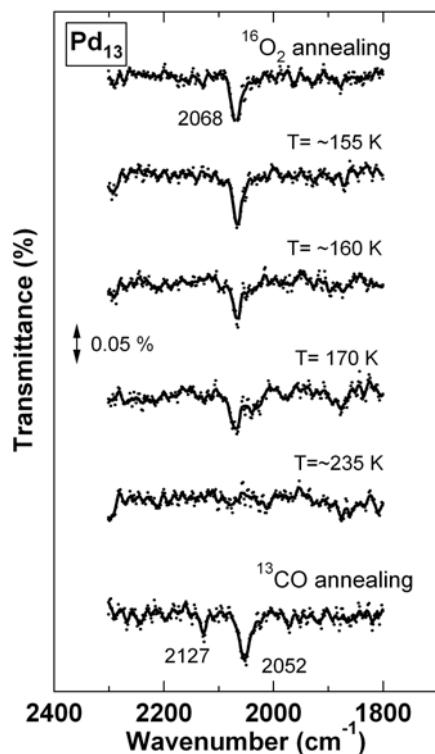


Fig. 5.12: Illustrating FTIR spectra of the oxygen annealed nanocatalyst at various temperatures. The lower spectrum indicates the annealed sample in a ¹³CO background.

5.4. Summary

In the CO combustion reaction over oxygen-treated palladium model catalysts, three main reaction mechanisms (α , β , γ) are involved. The low-temperature α -mechanism originates from highly activated molecularly bound oxygen. The second CO₂ formation at intermediate temperatures (~330 K) can also be due to molecularly adsorbed oxygen (β -mechanism), as oxygen is not dissociated on bulk materials at these temperatures. For the high-temperature γ -mechanism at ~410 K most likely, dissociatively adsorbed oxygen at surface or subsurface is responsible. A fourth reactivity observed at ~500 K for Pd₃₀ clusters only, originates from a mechanism similar to γ -mechanism. The relative contribution and population of the β - and γ -sites on Pd₁₃ and Pd₃₀ catalysts are different and vary with annealing temperature. These oxygen sites may exchange upon heating (scrambling effect). The γ -oxygen acts as a reservoir for the β -mechanism.

Metallic and treated catalysts (oxidised and reduced) contain different ¹³CO adsorption sites. Oxidation and reduction cycles are reversible to high extent;

Summary

however the reduction does not completely recover the metallic state of clusters. The knowledge about bonding type of adsorbed oxygen is necessary for precise conclusion about formation of nano-oxide clusters.

Chapter 6

6. Micro-cantilever sensors

Miniaturised cantilever sensors have enormous potential in gas detection, biochemical analysis, and medical applications issues. Depending on the measured physical property (resonance frequency and cantilever deflection), cantilever sensors can be operated in static, dynamic, or heat modes. In the latter case, the use of micro-mechanics for cantilever sensors outperform conventional calorimeters by enabling the detection of chemical reactions involving heat changes at the femtojoule level *via* the well-known bimetallic strip principle. Indeed, it is an ultra-sensitive mechanical way of converting chemical processes into a recordable signal using micro-fabricated cantilever arrays. Moreover, to obtain chemical functionality, cantilever beams are coated by sensor material to detect specific chemical interactions. The mechanical response is measured on the free-standing cantilever without resorting to a feedback loop.^{80,162-166}

Originally, micro-fabricated cantilevers are used as force sensors to image the topography of a surface by means of techniques such as scanning force microscopy (SFM) or atomic force microscopy (AFM).¹⁶⁷ In these methods, a cantilever with a sharp tip is scanned across a conductive or nonconductive surface using an x-y-z actuator system. The interaction of the cantilever tip with the surface, controlled by a feedback loop, is used to characterise and obtain a topography image of the sample's surface. The focus of the present research is, however, on applications of the cantilevers beyond the imaging of surfaces. Gerber and co-workers have designed a new type of calorimeter based on cantilevers for use in gaseous and vacuum environments, which can sense chemical reactions with an estimated limit of ~ 1 pJ.⁸⁰

Quite similarly, a bimetallic-cantilever based heat sensor has been developed in our group for measuring cluster binding energies, heats of adsorption, reaction, and desorption processes.⁸¹ Experimentally, possible applications of the sensor during cluster deposition and the catalytic hydrogenation of 1,3-butadiene over cluster model catalysts (a pulsed-molecular beam experiment) are addressed. Small dimension of the sensor elements result in short response times (μs -ms), and high sensitivities far superior to those possible with standard techniques.

6.1. Experimental

A highly sensitive micro-mechanical calorimeter was used for investigation of (a) the released heat during the deposition of metal clusters, and (b) a pulsed-molecular beam experiment (hydrogenation of 1,3-butadiene). As described in chapter 2, the measurement of the released heat ($Q > 0$) was carried out with a bimetallic cantilever (i.e. a two-component cantilever: an array of eight silicon cantilevers, each coated with a thin gold layer (~ 120 nm)). The released heat due to exothermic processes (e.g. cluster deposition, chemical reactions) increases the cantilever's temperature ($\Delta T > 0$), which leads to a bending of the sensor towards the layer with the smaller expansion coefficient (Fig. 6.1(b)). The bending is measured from the deflection of a reflected laser beam on a position sensitive detector (PSD), which is schematically shown in Fig. 6.1(a). However, during our experiments the total cantilever bending is also influenced by a transferred momentum P that is from the cluster's initial velocity, He carrier gas, or incoming reactant gas pulses (Fig. 6.1(c)). Therefore, the measured voltage signal from the deflection of the laser beam on the PSD depends on the orientation of the cantilever relative to the cluster beam and gas pulse axis. This voltage signal U_{1-2} (U_1-U_2) is proportional to the bending at the free end of the cantilever. Fig. 6.1 illustrates the sensor orientation in our setup. For this configuration the total time-dependent cantilever bending $\delta_l(t)$ is given by:

$$\delta_l(t) = \delta_l^Q(t) - \delta_l^P(t), \quad (1)$$

with the contribution δ_l^Q and δ_l^P from the released heat Q and the transferred momentum P , respectively.

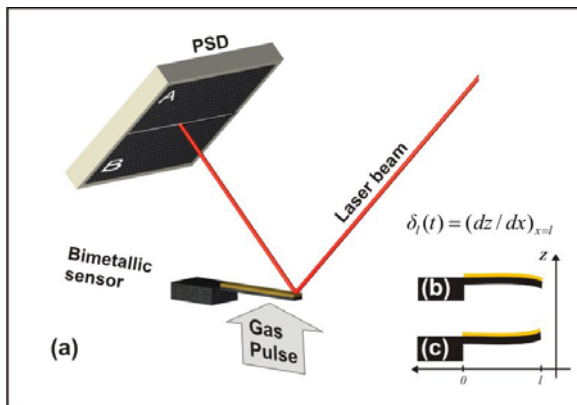


Fig. 6.1: Schematic description of the micro-cantilever based calorimeter, (a) orientation of the bimetallic-sensor, (b) mechanical response, and (c) thermal response. The layer having larger expansion coefficient (Al or Au) is faced to a laser beam. The measured signal of the position sensitive detector U_{A-B} is proportional to the bending δ_l at the free end of the sensor.

6.2. Operation modes and properties of bimetallic cantilevers

The thermal bending (operation mode) of the sensor (multilayered cantilever) depends on the temperature distribution along the length of the cantilever. Accordingly, a bimetallic sensor acts as a thermometer, when the sensor is in thermal equilibrium with a completely enclosed thermal bath (a uniform heat flux). As a consequence, the temperature along the cantilever is constant. In the so-called calorimeter mode, the sensor responds to its environment as heat evolves on the cantilever. This heat flows down along the cantilever to a heat sink at the point where the cantilever is fixed. It is assumed that the cantilever holder to be a perfect heat sink at a constant temperature, T_0 . In this mode of operation, two scenarios for the thermal response of the sensor are considered: i) the evolution of heat at the free-standing end of the cantilever (e.g. when a laser focused on the end of the sensor, for calibration purposes and during measurements (negligible)), ii) the evolution of the heat along the entire length of the sensor (e.g. when the sensor is coated with an absorbing sample).

For the rectangular cantilever of length l and width w , which consists of two layers with thickness t_1 and t_2 , the heat and momentum contributions to the total bending at different modes of operation are described by the following formulas:^{163,168}

$$\text{Thermometer mode: } \delta_l^T(t) = \frac{6(\alpha_1 - \alpha_2)(t_1 + t_2)l}{t_2^2 K} (T - T_0), \quad (1)$$

$$\text{Calorimeter mode: } \delta_l^Q(t) = \frac{2(\alpha_1 - \alpha_2)(t_1 + t_2)l^2}{t_2^2 (\kappa_1 t_1 + \kappa_2 t_2) w K} \dot{Q}, \quad (2)$$

$$\text{Momentum transfer: } \delta_l^P(t) = \frac{2(\alpha_1 - \alpha_2)(t_1 E_1 + t_2 E_2)l^2}{t_2^3 t_1 E_1 E_2 w K} \dot{P}, \quad (3)$$

wherein $\alpha_{1,2}$ are the thermal expansion coefficients, $\kappa_{1,2}$ the thermal conductivities, and $E_{1,2}$ the Young modulus of the two layers and

$$K = 4 + 6 \left(\frac{t_1}{t_2} \right) + 4 \left(\frac{t_1}{t_2} \right)^2 + \frac{E_1}{E_2} \left(\frac{t_1}{t_2} \right)^3 + \frac{E_2}{E_1} \left(\frac{t_2}{t_1} \right). \quad (4)$$

The subscript 2 refers to the Si layer. The relevant physical properties of the different materials employed in this study are given in Table 6.1.

Element	ρ 10^3 kg m^{-3}	E 10^{11} Pa	α 10^{-6} K^{-1}	K $\text{W m}^{-1} \text{ K}^{-1}$	C $10^2 \text{ J K}^{-1} \text{ kg}^{-1}$
Gold	19.3	0.78	14.2	320	1.27
Aluminum	2.7	0.70	23.1	235	9.04
Chrome	7.1	2.79	4.9	94	4.48
Silicon	2.3	0.47	2.6	150	7.2

Table 6.1: The physical properties of gold, aluminum, chrome, and silicon: density ρ , Young modulus E , thermal expansion coefficient α , thermal conductivity coefficient κ , and heat capacity per unit of mass c .¹⁶⁹

6.3. Calibration of the calorimeter

6.3.1. Sensitivity of the bimetallic-cantilevers

As shown in equations 1-3 (§ 6.2), the sensitivity of the bimetallic cantilevers is proportional to the difference between the expansion coefficients ($\alpha_{1,2}$) of the two layers. Thus, theoretically the sensitivity of Al-coated cantilevers will be two times higher than Au-coated ones. The Young modulus E_i also influences the sensitivity; however, it is less important since the Young's modulus of different metals is similar. Note that in the calorimeter mode (Eq. 2), the sensitivity of the cantilever with respect to the film thickness is controlled by two opposite effects. On one hand, the bending of the cantilever increases linearly with the thickness. On the other hand, the thermal capacity and diffusion of the cantilever also rises with the film thickness (due to larger amount of deposited material and surface areas). Enhancement of these two parameters lowers the sensitivity of multilayered cantilevers. In Fig. 6.2, the theoretical sensitivity of the multilayered cantilevers as a function of the relative thickness is depicted. Accordingly, the predicted optimum film thickness for gold and aluminum was found to be ~240 and ~200 nm, respectively. The relative thickness Θ is defined as a function of the absolute thickness of the metal layer (t_1) and is given by:

$$\Theta = \frac{t_1}{\sum_i t_i}. \quad (5)$$

It should be noted that based on the three layer mechanical model, the presence of the chromium interlayer (~1 nm) provides a negligible effect on the overall sensitivity of the cantilever.

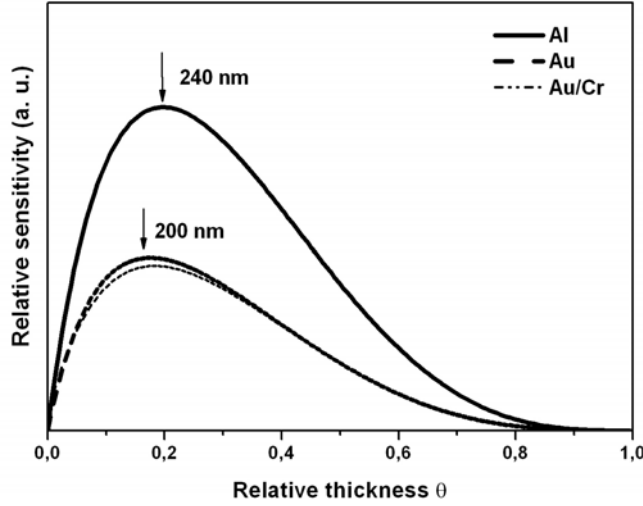


Fig. 6.2: Predicted sensitivity of the multilayered cantilevers in the calorimeter mode as a function of the relative thickness θ of the metal films: aluminum (solid-line), gold (dashed-line), and a gold with a ~10 nm chrome interface (dotted-line). Arrows show optimum thicknesses for Au and Al films on a Si cantilever of 1 μm thick.

6.3.2. Response time of the bimetallic-cantilever

To find the minimum detectable heat from the measured PSD signal, the system should be calibrated. Theoretically, the time constant τ for thermal relaxation of the sensor can be determined through the dynamics of the sensor. For the sensor in the thermometer mode (at a constant temperature along its length) τ is given by:¹⁶³

$$\tau = \frac{(\rho_1 C_1 t_1 + \rho_2 C_2 t_2)}{(\kappa_1 t_1 + \kappa_2 t_2)} l^2. \quad (6)$$

Similarly, for the calorimeter mode (heated either only at its end or across entire length) τ is determined by:

$$\tau = \frac{(\rho_1 C_1 t_1 + \rho_2 C_2 t_2)}{3(\kappa_1 t_1 + \kappa_2 t_2)} l^2, \quad (7)$$

where $\rho_{1,2}$ and $C_{1,2}$ are the density and heat capacity of the layers, respectively. For our sensors, when heated across their entire length, τ is predicted to be in the range of ~0.86 and ~1.9 ms for ~500 and ~750 μm long, Au-coated (~120 nm) cantilevers, respectively.

In order to verify theoretical estimations based on the mechanical model, and to determine the total released heat from the measured PSD signal the system has been calibrated. To this end, properties of the sensor in the calorimeter

mode for bimetallic-cantilevers of various lengths and thicknesses were characterised through measuring the sensor response to a known thermal load. This calibration process was described in more detail in § 3.2.2. Briefly, the thermal bending of the cantilever was determined by the displacement of the reflected laser spot on the PSD as a function of the power adsorbed on the sensor. To determine the adsorbed power on the sensor ($\sim 6 \mu\text{W}$), the reflectivity of the metal films was taken into account and the photon flux was normalised to the area of the sensor. Values for sensitivity and response time were obtained by measuring the amplitude and rise time of the cantilever response, respectively. In Fig. 6.3, a typical time-dependent response of the cantilevers ($750 \mu\text{m}$, 120 nm Au layer) to the pulsed laser in air (Fig. 6.3(a)) and vacuum (Fig. 6.3(b)) is depicted, respectively. Note that the response time of the cantilever is significantly faster in vacuum conditions (see below).

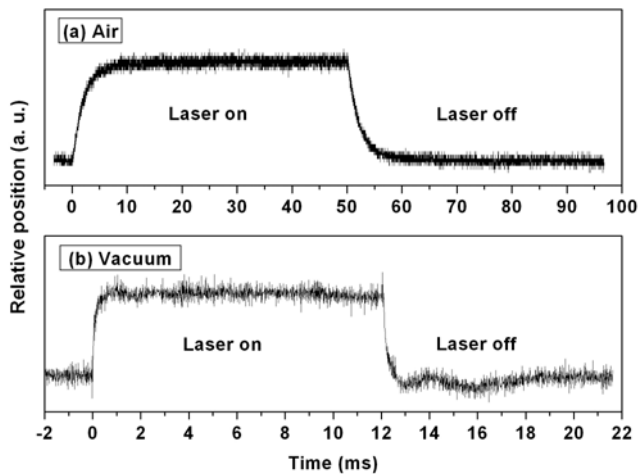


Fig. 6.3: The time-dependent response of the cantilever ($750 \mu\text{m}$, 120 nm Au-coated layer) to a known thermal load (pulsed laser). Note that scales are not the same for experiments in (a) air and (b) vacuum.

For experiments presented here, the sensitivity for each cantilever was calculated from the slope of the PSD signal (measured amplitude) as a function of the absorbed power. Consequently, the sensitivity can be quoted in units of $(\text{nW})^{-1}$. The obtained sensitivity for various bimetallic cantilevers (different lengths and metallic layers) is shown in Fig. 6.4. As predicted by the mechanical model, the measured cantilever sensitivity increases with the thickness of the metal film (Au and Al). However, the theoretically predicted optimum film thicknesses (Fig. 6.2) could not be achieved experimentally, due to the undesired curvature (not straight at room temperature) of the levers during/after long evaporation time of the metallic layer. Additionally, a higher length-dependent sensitivity in comparison to the theoretical model (quadratic relation in Eq. 2) is observed for gold-coated cantilevers with two different lengths (500

and 750 μm). Finally, the sensitivity for Al-coated cantilevers is almost 2-4 times higher than Au-coated cantilevers, which is in a good agreement with the theoretical model (Eq. 2).

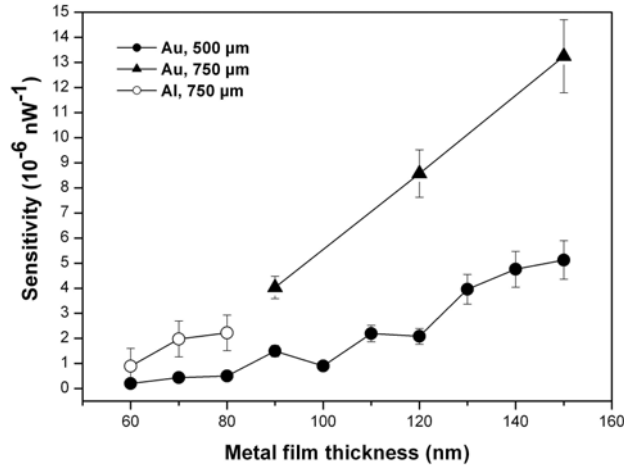


Fig. 6.4: Sensitivity of the bimetallic-cantilevers as a function of the metal film thickness. Au-coated cantilevers with different lengths are shown with filled symbols (500 μm ●, and 700 μm ▲) and Al-coated cantilevers with open symbol (○). Error bars were obtained from standard deviation of measured values.

As discussed above, the response time of the cantilever was obtained from an exponential fit of the PSD signal (relative position, U_{1-2}) to a thermal load. In Fig. 6.5, the response time of an Au-coated cantilever (750 μm long) measured under UHV condition was measured to be $\sim 70 \mu\text{s}$.

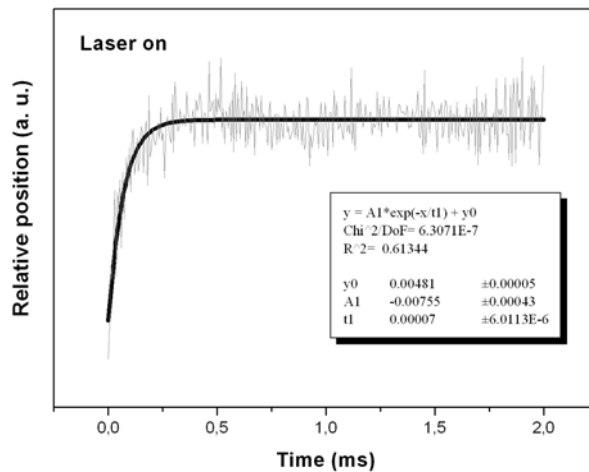


Fig. 6.5: Showing the exponential fit (solid line) of the cantilever response to a pulsed laser. Data is shown in grey colour for an Au-coated cantilever (750 μm , 120 nm gold layer).

Further characterisation was performed on Au-coated cantilevers (500 and 750 μm) as a function of the gold layer thickness under atmospheric condition (air). Fig. 6.6 illustrates the response time of the cantilever measured in air for different cantilevers having various thicknesses. These results clearly indicate that the response time is mainly dependent on the length of the cantilever, which defines the time of the heat exchange between cantilever and its body. This is also in consistence with the theoretical model (Eq. 7).

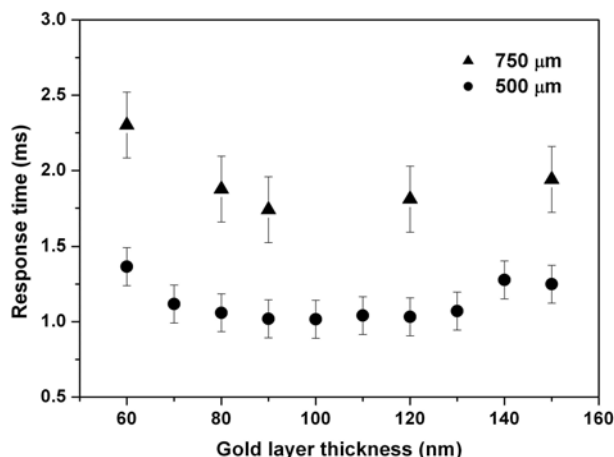


Fig. 6.6: Illustrating response time (heating) of the cantilever measured in air as a function of gold layer thickness for 750 μm (▲) and 500 μm (●) cantilevers. Error bars were obtained from standard deviation of measured values.

Considering aforementioned experimental results, the optimum sensor quality was obtained by Au-coated cantilevers with a length of 750 μm. A typical sensitivity of these cantilevers were $\sim 8.5 \times 10^{-6} \text{ nW}^{-1}$. By taking into account the PSD resolution (0.001 units), 118 nW would be a minimum detectable power for the sensors. Normalising the minimum detection limit to the area of the cantilever ($7.5 \times 10^{-8} \text{ m}^2$), a value of 1.6 W/m^2 was obtained. In air (vacuum) a response time of $\sim 2 \text{ ms}$ ($\sim 0.5 \text{ ms}$) allows a minimum detectable energy value of $\sim 236 \text{ pJ}$ ($\sim 59 \text{ pJ}$) to be achieved.

It is important to remark here that although the main function of the bimetallic cantilevers is the thermal sensing, they can also be used to detect very small mechanical forces (mechanical mode). Therefore, for the cluster deposition and pulsed-molecular beam experiments the mechanical response of the cantilever to the momentum transfer must be known.

For the pulsed-MBRS experiments, the mechanical signature was determined through calibration by using pulses of inert gases that are inert on the cantilever surface (no reaction heat). Figure 6.7 shows the normalised response time of the cantilever to a pulse of neon (Fig. 6.7(a)) and argon (Fig. 6.7(b)), for increasing flux. The opening time of the pulse valve on the electronic controller unit was increased from $\sim 50 \text{ μs}$ in the topmost curve to $\sim 150 \text{ μs}$ in the lower one. No *in situ* measurements were performed to determine the actual beam profile and pulse width for these studies. However, earlier calibration experiments in our group, using a fast ion gauge have shown that the actual pulse width at backing pressures of $\sim 1\text{-}2 \text{ bars}$ can be $\sim 4\text{-}6$ times larger than the opening time depending on the applied voltage. Assuming similar condition for the present study, a pulse width would be in a range of $\sim 200\text{-}900 \text{ μs}$, which is in

consistent with the time scale of the measured signal. In Fig. 6.7, for both measurements with Ne and Ar, a major peak is observed with a response time approximately five times faster than expected for a thermal response time. Therefore, this peak is assigned to the momentum transfer from gas phase atoms, (impinge directly onto the Si-oxide face). Additionally, a small counteraction is also seen.

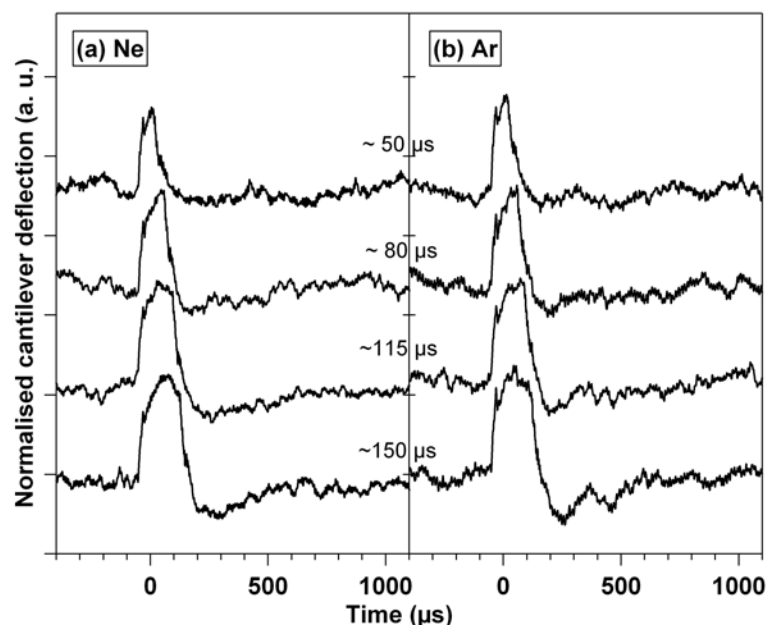


Fig. 6.7: Response of the cantilever to a pulse of (a) neon, (b) argon for increasing pulse duration. The signal is typically averaged over 200-300 pulses. All data are shown in an equal scale.

Note that the momentum transfer between the gas pulse and the cantilever is mass independent as observed for helium, argon and neon. Since the mean velocity of the pulsed gas atoms/molecules is proportional to the inverse of the

square root of the mass ($u = M \sqrt{\left(\frac{\gamma k_B T}{m}\right)}^{1/2}$), thus the momentum is proportional

to the square root of the mass. On the contrary, the flux of gas through the pulsed valve is proportional to the inverse of the mass square root

($F = \frac{P}{\sqrt{2\pi m k_B T}}$)⁷⁷. Consequently, these two terms cancel out mass dependency

in the momentum transfer and hence, the measured inert gas data can be used as a reference for the momentum transfer signature in other experiments with reactive gases.

6.4. Calorimetric applications

6.4.1. Cluster binding energies

Time-dependent measurements of the cantilever bending allow the determination of heat released during cluster deposition, which originates from cluster's momentum transfer, plastic deformation upon deposition, cluster/support binding energy, and neutralisation of the charged clusters.

A typical response of a bimetallic cantilever during cluster deposition (cluster current = ~ 380 pA) is depicted in Fig. 6.8. An increase in the PSD signal with time indicates that the sensor does not work in calorimeter mode. In fact, if the cantilever is exposed to a continuous source of heat (cluster beam), after a few milliseconds the cantilever temperature varies uniformly with the released heat and is not constant anymore. The cantilever body no longer acts as a perfect heat sink due to the limited heat capacity and imperfect thermal contact between the cantilever body and cantilever holder. This implies that the sensor operates in the thermometer mode during cluster deposition and is sensitive to temperature changes (Eq. 1). These observations are in consistence with other studies¹⁶⁸ used the same technique to investigate thermal properties of isolated metal clusters.

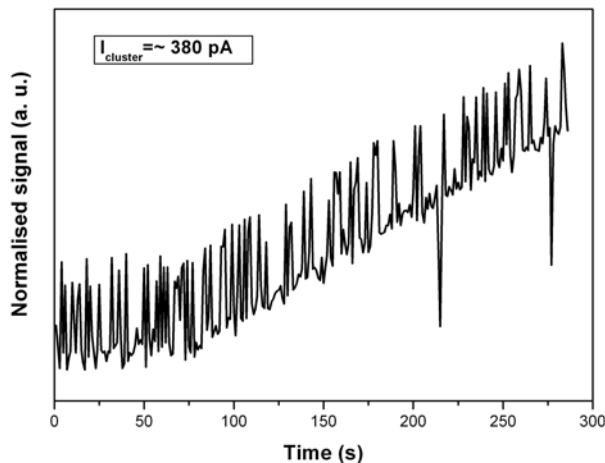


Fig. 6.8: Response of the sensor during cluster deposition (Pd_n , $n > 25$) having a cluster current of ~ 380 pA.

As mentioned in chapter 2, a focusing octopole was positioned in close vicinity of the cantilever array (uncoated surface) during cluster deposition. Therefore, the measured cantilever response during deposition can be partly caused by the radio-frequency (RF) power of this element. To determine the thermal effect (radiated heat) of the focusing octopole, the cantilever response was measured

in a separate experiment with the cluster source turned off. The thermal bending of the cantilever for two different RF powers is depicted in Fig. 6.9.

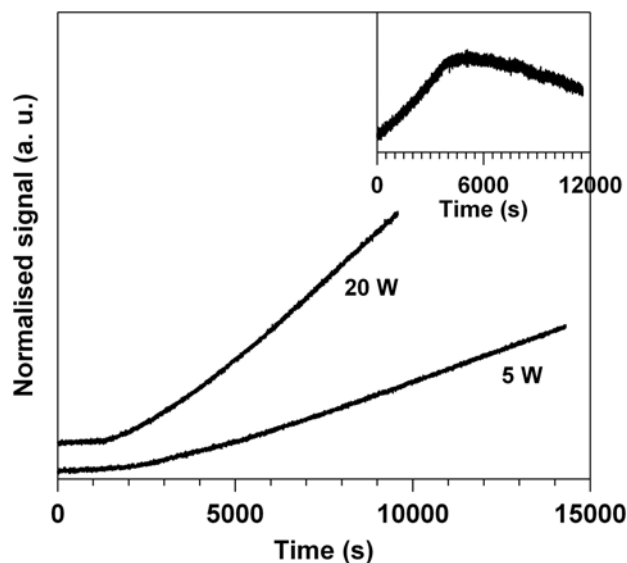


Fig. 6.9: Illustrating the time-dependent cantilever response as a function of the RF power (5 and 20 W) of the focusing octopole. The inset shows the cantilever response after turning off the RF power. Note that the power corresponds to the value set on the RF transceiver and not to the actual power transferred to the octopole.

The rate of the cantilever bending also increases with the RF power. The Inset shows the response of the cantilever after turning off the RF power. When the radio-frequency power was turned off, the cantilever was still heated for several minutes due to the thermal inertia of the rods. The cantilever finally began to cool down after approximately 6 minutes. While the octopole was turned off and moved away from the cantilever, the cooling was immediately observed; these results are consistent with the interpretation of the focusing octopole acting as an extra heating source during cluster deposition. Therefore, for investigating cluster deposition, the octopole-induced thermal bending was subtracted. The corrected cantilever bending is shown in terms of the bending rate as a function of the cluster current in Fig. 6.10. The temperature of the cantilever still exhibits a noticeable increase with time. A linear fit to the data, gives the slope of the bending rate ($2.68 \times 10^{-5} \text{ s}^{-1} \text{ pA}^{-1}$), having the calibration factor ($5.52 \times 10^{-7} \text{ J/unit}$), a value of $1.48 \times 10^{-11} \text{ W pA}^{-1}$ was obtained as a total power released upon clusters deposition, which corresponds to a total heat release of $14.8 \pm 3.6 \text{ eV}$ per deposited cluster. This is an important result allowing the interpretation of the energetics involved in cluster deposition and in particular the evaluation of the approximate binding energies of clusters to the support. Given a mean kinetic energy of the clusters (Pd_n , $n > 25$) of $\sim 2 \text{ eV}$ and cluster neutralisation energy ($\sim 5 \text{ eV}$)¹⁷¹, an adhesion energy (the energy balance between the energetic cost of the deformation of the cluster once in contact with the

substrate and the binding energy of the cluster to the substrate with respect to the gas-phase structure) was estimated to be $\sim 7\text{-}8$ eV. This estimation correlates well with existing data¹⁷². Medium-sized Pd_n clusters favor compact structures and the adhesion energy per cluster atom at the interface is $\sim 0.3\text{-}0.5$ eV¹⁷². Assuming that 10-12 atoms are at the interface, the binding energy would be $\sim 3\text{-}6$ eV per cluster.

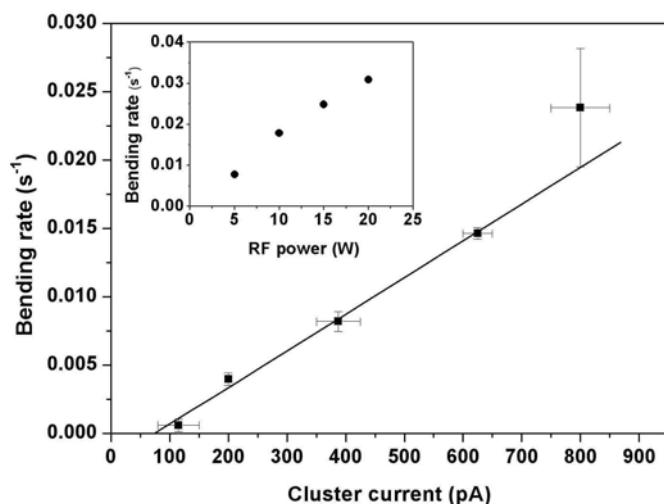


Fig. 6.10: Corrected response of the cantilever during the cluster deposition (Pd_n , $n > 25$) as a function of the cluster current. The inset shows, heat rates as a function of the octopole RF power.

6.4.2. Hydrogenation of 1,3-butadiene on Pd model catalysts

To explore the heat of reaction during hydrogenation processes over palladium catalysts, after depositing Pd_n clusters onto the uncoated side of the cantilever (natural SiO_2), an isotropic pressure of 1,3-butadiene was introduced into the UHV chamber using a leak valve. The partial pressure of 1,3-butadiene was varied between 5×10^{-8} and 1×10^{-5} mbar. The hydrogenation of 1,3-butadiene over Pd_n cluster catalysts, was induced by exposing the model catalyst to hydrogen pulses. The piezo-driven pulsed-valve was operated at 1 Hz ($V = -725$, opening time = 50-115 μs). Note that the interval between hydrogen pulses (1 s) are significantly larger than the response time of the cantilever ($\sim 0.5\text{-}1$ ms for a maximum absorbed power of about 6 μW) and thus the sensor acquires its equilibrated condition prior to the next incoming pulse. In these studies, for each experiment a new cantilever is used. Upon introduction of H_2 pulses onto the catalyst, heat releases due to the catalytic reaction. This leads to a temperature gradient along the cantilever, which induces bending. The bending was detected by a change in the angle of a light beam reflected from the lever and recorded by a PSD. The normalised signal, $(U_1 - U_2)/(U_1 + U_2)$ are presented here.

U_1 and U_2 are the signals detected by two opposite sectors of the PSD (see § 2.3.2).

As explained in § 6.3.1, to extract the absolute thermal bending of the cantilever, contribution of the momentum transfer (inert gas, Fig. 6.7) should be subtracted. Fig. 6.11 illustrates a representative response of the cantilever for both cases (inert gas and hydrogenation reaction) under the same experimental conditions. The area under the curve (hatched-area) after subtraction was taken as a total heat released during hydrogenation reaction. Note that the opposite deflection direction of the mechanical (positive) and thermal (negative) bending is consistent with our experimental configuration as shown in Fig. 6.1.

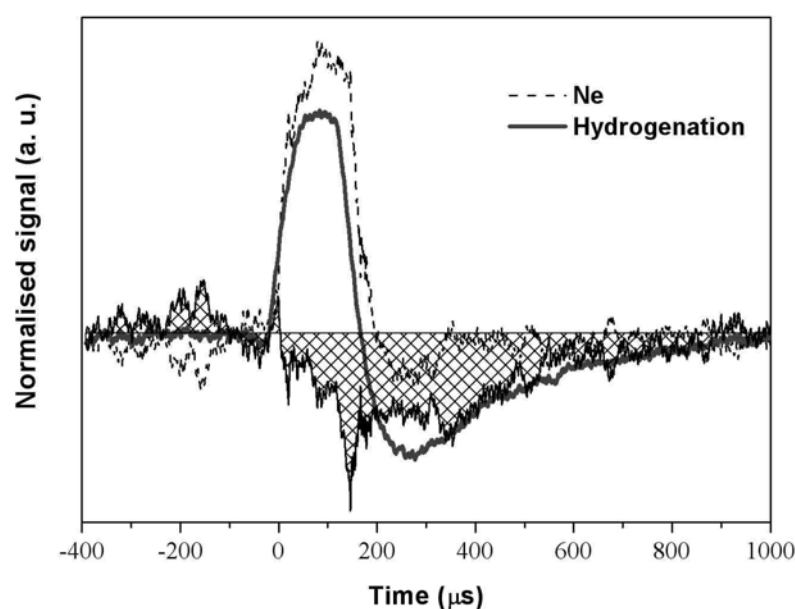


Fig. 6.11: Solid line: the time-dependent response of the cantilever during 1,3-butadiene hydrogenation over Pd_n clusters ($P_{\text{Butadiene}} = 5 \times 10^{-7}$ mbar). Dashed line: response of the cantilever to a pulse of Ne under the same valve conditions. Hatched-area: the difference between two signals. Data were averaged over 200 pulses.

In Fig. 6.12, total hydrogenation reaction heat over Pd_n cluster catalysts ($n > 25$, ~1% ML) as a function of 1,3-butadiene isotropic pressure and constant hydrogen pulses (opening time = 80 μs) are depicted. The reaction rate was increased with the 1,3-butadiene partial pressures and obtained its maximum at $\sim 6.6 \times 10^{-7}$ mbar, and then finally deteriorated at higher pressures as the clusters were saturated (poisoned) by butadiene. At the maximum reaction rate, the measured heat was found to be $\sim 1.66 \times 10^{-19}$ J per cluster and per pulse.

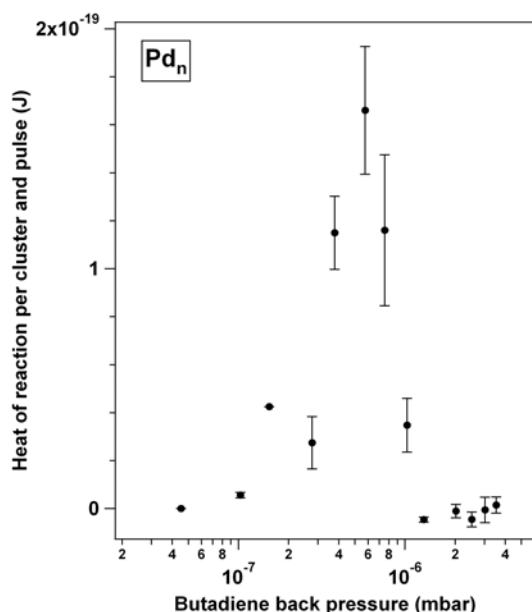
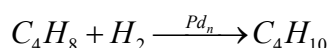
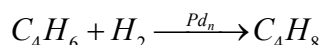


Fig. 6.12: Heat of reaction per cluster and hydrogen pulse detected with the cantilever sensor as a function of the isotropic pressure of 1,3-butadiene during the hydrogenation reaction on size-distributed, supported palladium clusters (~1 %ML).

In order to analyse reaction products, additional measurements utilising p-MBRS coupled with a mass spectrometer were performed in the analysis chamber under similar experimental conditions. That is hydrogenation of 1,3-butadiene at room temperature on Pd clusters, soft-landed onto the Si-oxide surface.

The hydrogenation products include butane (C_4H_{10} , 58 amu) and a number of butene (C_4H_8 , 56 amu) isomers (1-butene cis- and trans-2-butenes).



Based on the fragmentation pattern of the product molecules (Fig. 6.13), peaks at 41 and 43 mass-to-charge ratio (m/z) have the highest intensities among butene and butane fragments, respectively.¹⁷³ These fragmentation patterns are given in literature and measured under conventional electron ionisation conditions (~70 eV). Note that the peak at 41 m/z is also present in the mass spectrum of butane (Fig. 6.13(b)). Therefore, to precisely analyse the hydrogenation reaction and determine the origin of this peak (41 m/z) under our experimental condition (electron ionisation energy of ~90 eV), the sensitivity of the mass spectrometer to both of the product molecules (butene and butane) should be known.

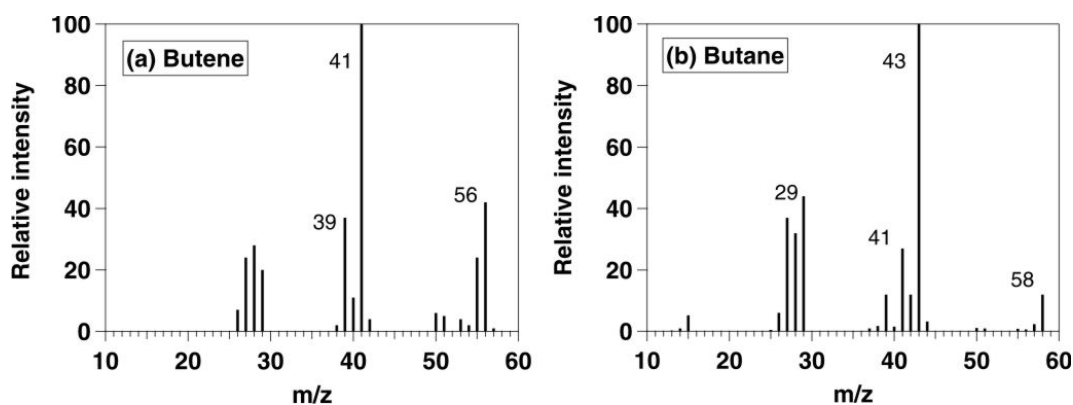


Fig. 6.13: Mass spectra of (a) butene and (b) butane by electron ionisation (~ 70 eV).¹⁷⁴

To do this (sensitivity measurement), the mass signal from dosing of defined amounts of butene and butane into the UHV chamber using a molecular beam doser at room temperature was measured. The main mass detected during butene exposure is only 41 amu, and for butane mass 43 and 41 amu are observed in a ratio (height-to-height intensity) of $\sim 2:1$, as shown in Fig. 6.14 (a) and (b), respectively. The mass ratio for both 41 amu fragments of butene and butane was evaluated to be 1:1.

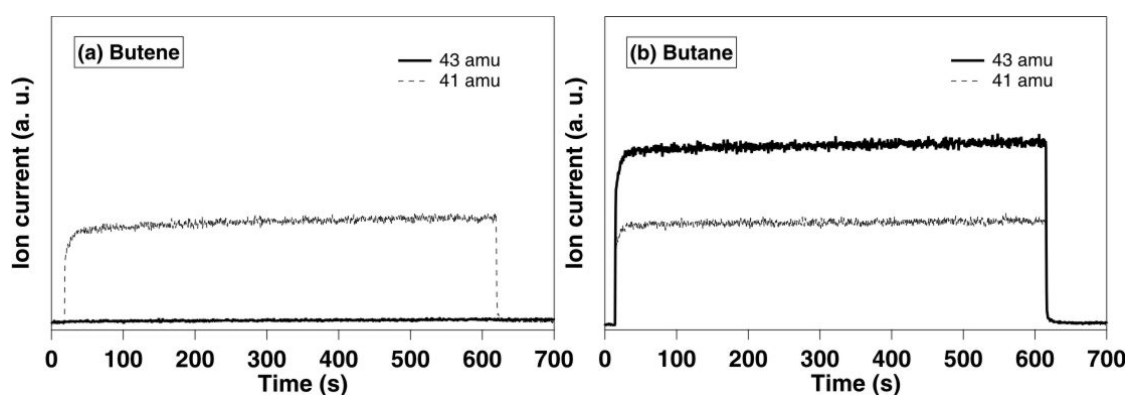


Fig. 6.14: Measured mass spectrometer signal (ion currents), released from a molecular beam doser at constant flux of butene (a) and butane (b), respectively. The experiment was performed at room temperature.

The p-MBRS experiments at various isotropic pressures of 1,3-butadiene were performed at constant hydrogen pulses (1 Hz) over size-distributed Pd clusters (Pd_n , $n > 25$). During hydrogenation reaction the parent ions of possible products (56, 58 amu) and selected fragments (41 and 43 amu) were monitored using a mass spectrometer. Typical transients of the detected ions on Pd_n clusters ($\sim 1\%$ ML) are depicted in figure 6.15. Note that negligible traces of parent ions were recorded during hydrogenation reaction.

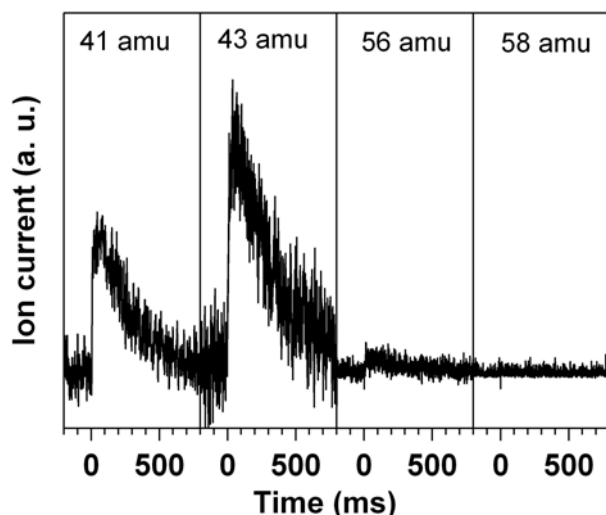


Fig. 6.15: The detected masses during the hydrogenation of 1,3-butadiene. The experiments (p-MBRS) were carried out at room temperature in a 1,3-butadiene atmosphere (5×10^{-7} mbar). The hydrogenation reaction was initiated on Pd_n clusters upon H₂ pulses at room temperature.

By integrating measured mass signals, a ratio of 2:1 was obtained for the masses 43 and 41. Furthermore, taking into account the sensitivity measurements that indicating two order of magnitudes higher values for the mass 43 amu with respect to the mass 41 amu, and the fact that the mass ratio for both 41 fragments of butane and butane at constant flux is unity; we conclude that under our experimental conditions (high partial pressure of hydrogen during a hydrogen pulse), the hydrogenation reaction was complete, and only butane was formed. Consequently, from the integration of mass signal (considering a calibration factor, see § 2.4.2), and known cluster coverage ($\sim 0.2\%$ ML, $1 \text{ ML} = 2.25 \times 10^{15} \text{ cluster cm}^{-2}$), the number of produced butane molecules per hydrogen pulse can be derived. The obtained reaction rates as a function of 1,3-butadiene back pressure are shown in Fig. 6.16. Note that for unselected cluster deposition, the size distribution is not necessarily identical and hence direct comparison between p-MRBS and calorimetric studies is not possible. However, the important result of the qualitative comparison is that the number of produced butane molecules exhibits a similar behavior to that observed by the micro-cantilevers, i.e. the highest reaction rate is observed at the same 1,3-butadiene pressure ($\sim 6 \times 10^{-7}$ mbar). Finally, normalising the measured maximum released heat on cantilevers ($\sim 1.66 \times 10^{-19}$ J per cluster, per pulse, Fig. 6.12) to the known reaction heat of butadiene hydrogenation (i.e. 3.9×10^{-19} J/molecule¹⁷⁵), the number of produced butane molecules was deduced to be ~ 0.43 butane molecules per Pd_n cluster and hydrogen pulse.

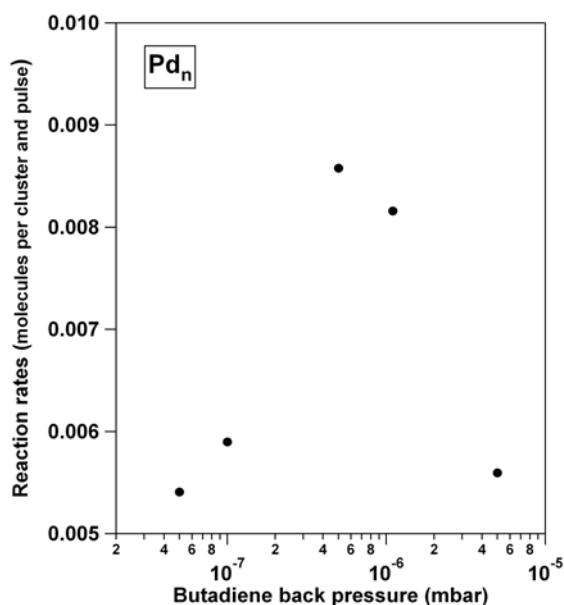


Fig. 6.16: Reaction rates of the hydrogenation of 1,3-butadiene on size-distributed palladium clusters (~1% ML) deposited onto a SiO₂ film. Experiments were performed in a separate p-MBRS setup at various isotropic pressures of 1,3-butadiene.

Hydrogen interaction on palladium clusters

In addition to the hydrogenation reaction, the interaction of hydrogen (1 Hz) with Pd_n clusters was also studied (Fig. 6.17). Upon each hydrogen pulse, repeated heat exchange with the cantilever sensor was measured and no saturation effects were detected during the continuous pulsing. By extracting the thermal contribution as detailed above, a total heat release of ~1.2 nJ pulse⁻¹ was obtained for a cluster density of ~2% ML. This implies an average heat exchange of $\sim 4 \times 10^{-20}$ J per pulse and per cluster. Currently, the exact mechanism of hydrogen interaction with the supported Pd_n clusters is unknown. Therefore, the detected energy, could be associated with a transfer of kinetic or vibrational energy of hydrogen molecules (adsorption and desorption process). Alternatively, hydrogen molecules may adsorb (and dissociated) on the Pd_n clusters and diffuse onto the cantilever holder. This would indicate a spill-over process.

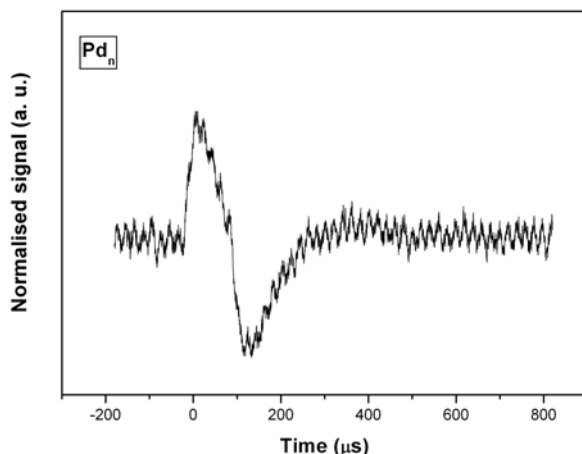


Fig. 6.17: The time-dependent response of the cantilever to a H_2 pulse over size-distributed Pd_n clusters ($\sim 2\%$ ML), 200 pulses averaged.

6.5. Summary

The experimental results indicate that a newly developed bimetallic sensor is indeed capable of approximating cluster binding energies and reaction heats of chemical processes. The accuracy of the measurements during the cluster deposition will be augmented in the future using size-selected clusters, for which the kinetic energies and electron affinities are known more precisely. In addition, it may be feasible to decelerate and neutralise the clusters prior to deposition, in order to diminish the contribution of heat transfer by these processes. Furthermore, for chemical reactions involving two reactants, it is possible to measure normalised adsorption and reaction heats when two pulsed-molecular beams are employed. A pulse of the first reactant results in a thermal bending of the cantilever due to the released adsorption heat. By introducing the second reactant, catalytic process occurs and total heat during reaction can be measured. Since the reaction heat is independent of the catalyst material in contrast to the heat of adsorption, by comparing the measured heat with the literature, the total heat of reaction can be normalised and thus be used as an internal calibration of the released heat.

Appendix A

A.1. Auger electron spectroscopy

The Auger effect was discovered by Pierre Auger in 1925 while working with X-rays and using a Wilson cloud chamber.¹⁷⁶

Auger electron spectroscopy (AES) has now emerged as one of the most widely used analytical techniques for obtaining the chemical composition of solid surfaces. The basic advantages of this technique are high sensitivity for chemical analysis in the 5-10 Å regions near the surface, a rapid data acquisition, detection of all elements above helium, and high-spatial resolution.¹⁷⁷⁻¹⁷⁹

A.2. Theory of Auger electron spectroscopy

There are two principal processes for the filling of an inner-shell electron vacancy in an excited or ionised atom: a radiative (X-ray) or non-radiative (Auger) process. The Auger effect is a two-electron process, in which an electron makes a discrete transition from a less bound shell to the vacant but more tightly bound electron shell. The energy gained in this process is transferred, *via* the electrostatic interaction to another bound electron, which then escapes from the atom. This outgoing electron is referred to as an Auger electron and is labelled by letters corresponding to the atomic shells involved in the process.^{177,179}

The Auger process can be understood by considering the ionisation process of an isolated atom under electron bombardment. The incident electron with sufficient primary energy, E_p , ionises the core level, such as a K level. The vacancy thus produced is immediately filled by another electron from L_1 . This process is shown in Fig. A.2. The energy ($E_K - E_{L1}$) released from this transition can be transferred to another electron, as in the L_2 level. This electron is ejected from the atom as an Auger electron. By the conservation of energy, the Auger electron kinetic energy E is energy given by:

$$E = E_K - E_{L1} - E_{L2}.$$

This excitation process is denoted as a KL_1L_2 Auger transition. Since the energy levels of atoms are discrete and well understood, the Auger energy is thus

signature of the emitting atom. It is obvious that at least two energy states and three electrons must take part in an Auger process. Therefore, H and He atoms cannot give rise to Auger electrons. The Auger electron energies are characteristic of the target material and independent of the incident beam energy.

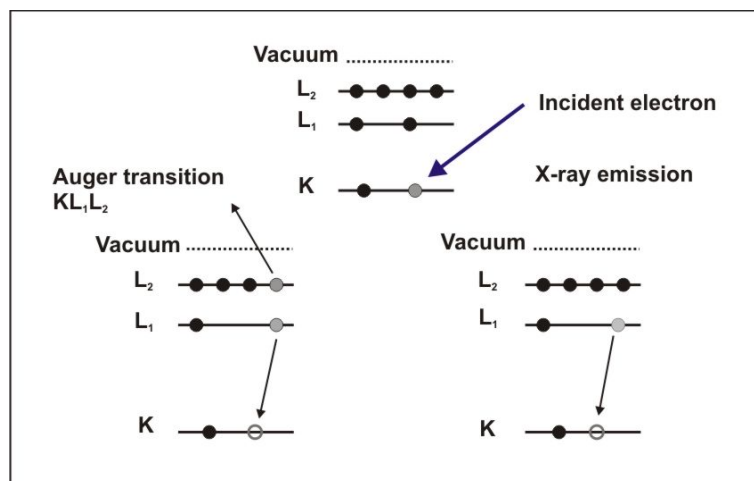


Fig. A.2: Energy level diagram in an Auger process. Electron from L_1 drops into the K level with the emission of an L_2 electron.

The most pronounced Auger transitions observed in AES involve electrons of neighbouring orbitals, such as *KLL*, *LMM*, *MNN*, *NOO*, *MMM*, and *OOO* families. The most prominent *KLL* transitions occur from elements with atomic number $Z = 3 - 14$, *LMM* transitions for elements with $Z = 14 - 40$, *MNN* transitions for elements with $Z = 40 - 79$, and *NOO* transitions for heavier elements. The Auger peak is commonly identified by the maximum negative peak in the $dN(E)/dE$ versus E spectrum.

A.3. AES instrumentation

The schematic of the experimental arrangement for basic AES is shown in Fig. A.2. The sample is irradiated with electrons from an electron gun. The emitted secondary electrons are analysed for energy by an electron spectrometer. The experiment is carried out in a UHV environment because the AES technique is surface sensitive due to the limited mean free path of electrons in the kinetic energy range of 20 to 2500 eV.¹⁸⁰ The essential components of an AES spectrometer are:

(i) UHV environment: The surface analysis necessitates the use of a UHV environment, since the equivalent of one monolayer of gas impinges on a surface every second in a vacuum of 10^{-6} torr. A monolayer is adsorbed on the surface of the specimen in about 1 second at 10^{-6} torr.

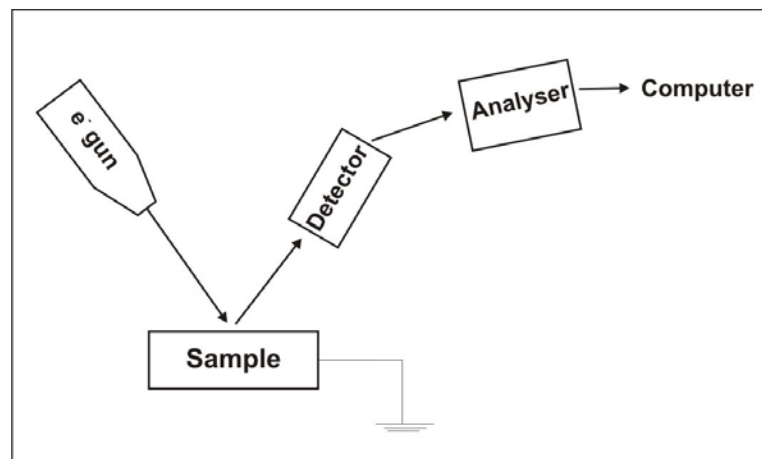


Fig. A.2: Schematic arrangement of the basic elements of an Auger electron spectrometer.

(ii) Electron gun: The range of beam currents normally used in AES is between 10^{-9} and 10^{-6} A. The electron gun system has two critical components: the electron source and the focusing forming lens. In most cases, the electron source is thermionic but for the highest spatial resolution the brighter field emission source may be used. The field emission sources have problems of cost and stability and are therefore limited in their use. The commonly used thermionic sources are a tungsten hairpin filament and Lanthanum hexaboride. The electron lenses used to focus the beam can be magnetic and electrostatic. The magnetic lenses have low aberrations and therefore give the best performance. However, these lenses are complicated and expensive. The electrostatic lenses are easier to fit in a UHV system. For spatial resolution of the order of a micron, a 10 keV electrostatic gun could be easily used. For spatial resolution below 100 nm electromagnetic lenses are used.

(iii) Electron energy analyser: The function of an electron energy analyser is to disperse the secondary emitted electrons from the sample according to their energies. An analyser may be either magnetic or electrostatic. Because electrons are influenced by stray magnetic fields (including the earth's magnetic field), it is essential to cancel these fields within the enclosed volume of the

analyser. The stray magnetic field cancellation is accomplished by using Mu metal shielding. Electrostatic analysers are used in all commercial spectrometers today, because of the relative ease of stray magnetic field cancellation.¹⁸¹ The cylindrical mirror analyser (CMA) and concentric hemispherical analyser (CHA) are two types of commonly used energy analysers. The main advantages that the CHA has over the CMA are much better access to the sample, and the ability to vary analyser resolution electrostatically without changing physical apertures.^{180,181}

(iv) Electron detector: Having passed through the analyser, the secondary electrons of a particular energy are spatially separated from electrons of different energies. Various detectors are used to detect these electrons. The detector used in conventional instrumentation is a channel electron multiplier, single channel detector (SCD). It is an electrostatic device that uses a continuous dynode surface (a thin-film conductive layer on the inside of a tubular channel). It requires only two electrical connections to establish the conditions for electron multiplication. The output of this detector consists of a series of pulses that are fed into a pulse amplifier/discriminator and then into a computer. The advantage of such a detector is that it can be exposed to air for a long time without damage. It counts electrons with a high efficiency, even at essentially zero kinetic energy, and the background is 0.1 count/sec or lower. The only drawback is that a high count rate ($> 10^6$ counts/sec) causes a saturation effect. On the other hand, in a multichannel detector (MCD), a multiple detection system is added at the output of the analyser. The system may be in the form of a few multiple, parallel, equivalent detector chains or position sensitive detectors spread across the whole of the analyser output slit plane. Such an arrangement can be devised in a number of ways: using phosphor screens and TV cameras, phosphor screens and charge-coupled devices, resistive anode networks, or discrete anodes.

(v) Data recording, processing, and output system: The Auger electrons appear as peaks on a smooth background of secondary electrons. If the specimen surface is clean, the main peaks would be readily visible and identified. However, smaller peaks and those caused by trace elements present on the surface may be difficult to discern from the background. Because the background is usually sloping, even increasing the gain of the electron detection

system and applying a zero offset is often not a great advantage. Therefore, the Auger spectra are usually recorded in a differential form. In the differential mode it is easy to increase the system gain to reveal detailed structure not directly visible in the undifferentiated spectrum.

Appendix B

B.1. Introduction to FTIR spectroscopy

The infrared region is valuable for the study of the structure of matter, because the natural vibrational frequencies of atoms in molecules and crystals fall in this range. Therefore, IR spectroscopy is a powerful technique that basically provides information about the molecular structure of materials (composition, conformation, orientation and functional groups) by simply measuring the characteristic vibrational frequencies of the chemical bonds.

The advantages of the IR spectroscopy such as, high sensitivity (typically 1/1000 of a CO monolayer), high resolution (1-5 cm^{-1}), and its ability to work at various pressures from UHV to atmospheric conditions on variety of surfaces, single crystals to supported catalysts, make it an important tool among other vibrational spectroscopies (Electron Energy Loss Spectroscopy, Surface Enhanced Raman Spectroscopy).

B.2. IR frequency range and spectrum presentation

Infrared radiation spans a section of the electromagnetic spectrum having wavelengths from roughly 0.78 to 1000 μm . It is bound by the red end of the visible region at high frequencies and the microwave region at low frequencies. IR absorption positions are generally presented as either wavelengths (λ) or wavenumbers ($\tilde{\nu}$). The wavenumber unit (cm^{-1}) is more commonly used in modern IR instruments, which defines the number of waves per unit length. Thus, wavenumbers are directly proportional to frequency, as well as the energy of the IR absorption.

IR absorption information is generally presented in the form of a spectrum with wavenumber as the x-axis and absorption intensity or percent transmittance as the y-axis. Transmittance, T , is the ratio of radiant power transmitted by the sample (I) to the radiant power incident on the sample (I_0). Absorbance (A) is the logarithm to the base 10 of the reciprocal of the transmittance (T).

$$A = \log\left(\frac{1}{T}\right) = \log\left(\frac{I_0}{I}\right)$$

The transmittance spectra provide better contrast between intensities of strong and weak bands because transmittance ranges from 0 to 100% T whereas absorbance ranges from infinity to zero.

The IR region is commonly divided into three smaller areas: near IR, mid IR, and far IR. We focus on the most frequently used mid IR region, between 4000 and 400 cm^{-1} . The far IR requires the use of specialised optical materials and sources. It is used for analysis of organic, inorganic, and organometallic compounds involving heavy atoms (mass number over 19). It provides useful information to structural studies such as conformation and lattice dynamics of samples. Near IR spectroscopy needs minimal or no sample preparation. It offers high-speed quantitative analysis without consumption or destruction of the sample. Its instruments can often be combined with UV-visible spectrometer and coupled with fiber optic devices for remote analysis. Near IR spectroscopy has gained increased interest, especially in process control applications.^{179,182}

B.3. Theory of infrared absorption/vibrational spectroscopy

At temperatures above absolute zero (even at absolute zero due to Heisenberg uncertainty principle), all the atoms in molecules are in continuous vibration with respect to each other. When the frequency of a specific vibration is equal to the incident frequency of the IR radiation, the molecule absorbs the radiation. A molecule composed of n -atoms has $3n$ degrees of freedom, six of which are translations and rotations of the molecule itself. This leaves $3n-6$ degrees of vibrational freedom ($3n-5$ if the molecule is linear). Vibrational modes are often given descriptive names, such as stretching, bending, scissoring, rocking and twisting. Infrared radiation is absorbed and the associated energy is converted into these types of motions. The absorption involves discrete, quantised energy levels. However, the individual vibrational motion is usually accompanied by other rotational motions. These combinations lead to the absorption bands, not the discrete lines, commonly observed in the mid IR region.

Among the $3n-6$ or $3n-5$ fundamental vibrations, those that produce a net change in the dipole moment may result in an IR activity and those that give polarisability changes may give rise to Raman activity. Naturally, some vibrations can be both IR- and Raman-active. The exact frequency at which a

given vibration occurs is determined by the strengths of the bonds involved and the mass of the component atoms.

B.4. FTIR instrumentation

In simple terms, IR spectra are obtained by detecting changes in transmittance (or absorption) intensity as a function of frequency. Most commercial instruments separate and measure IR radiation using dispersive spectrometers or Fourier transform spectrometers. However, the relative easy use of the commercial FTIR spectrometers, their superior speed and sensitivity make them the most popular approach for most research groups and therefore, the focus here is on this kind of spectrometers. Furthermore, in FTIR spectroscopy instead of viewing each frequency component sequentially, as in a dispersive IR spectrometer, all frequencies are examined simultaneously.¹⁷⁹

B.5. Spectrometer components

There are three basic spectrometer components in an FT system: (i) a radiation source, (ii) an interferometer and (iii) a detector. A simplified optical layout of a typical FTIR spectrometer is illustrated in Fig. B.1.

(i) The common radiation source for the IR spectrometer is an inert solid heated electrically to 1000-1800 °C. The hot material will then emit infrared radiation. Three popular types of sources are Nernst glower (constructed of rare-earth oxides), Globar (constructed of silicon carbide), and Nichrome coil. They all produce continuous radiations, but with different radiation energy profiles. However, the source is more often water-cooled to provide better power and stability.

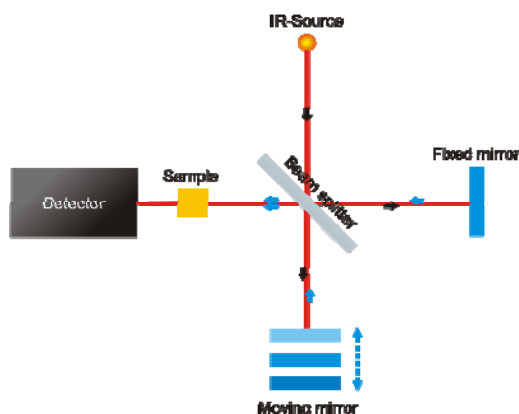


Fig. B.1: Simplified optical layout of a typical FTIR spectrometer.

(ii) The interferometer is a device, which divides radiant beams, generates an optical path difference between the beams, and then recombines them in order to produce repetitive interference signals. As its name implies, the interferometer produces interference signals, which contain infrared spectral information generated after passing through a sample. The most commonly used interferometer is a Michelson interferometer. It consists of three active components: a moving mirror, a fixed mirror, and a beam splitter (Fig. B.1). The two mirrors are perpendicular to each other. The beam splitter is a semi reflecting device and is often made by depositing a thin film of germanium onto a flat KBr substrate.

(iii) The most popular detectors for a FTIR spectrometer are the deuterated triglycine sulfate (DTGS) and mercury cadmium telluride (MCT). The former is a pyroelectric detector that delivers rapid responses because it measures the changes in temperature rather than the value of temperature. The MCT detector is a photon detector that relies on the quantum nature of radiation and also exhibits very fast responses. Whereas DTGS detectors operate at room temperature, MCT detectors must be maintained at liquid nitrogen temperature (77 K) to be effective. In general, the MCT detector is faster and more sensitive than the DTGS detector.

The entire performance of the spectrometer can be summarised as follow: the radiation from the broadband IR source is collimated and directed into the interferometer, and impinges on the beam splitter. At the beam splitter, half the IR beam is transmitted to the fixed mirror and the remaining half is reflected to the moving mirror. After reflection of the divided beams from the two mirrors, they are recombined at the beam splitter.¹⁸²

An interference pattern is generated, due to changes in the relative position of the moving mirror to the fixed mirror. The resulting beam then passes through the sample and is eventually focused on the detector. The detector signal is sampled at small, precise intervals during the mirror scan. Finally, a Fourier transformation converts the interferogram (a time domain spectrum displaying intensity versus time within the mirror scan) to the final IR spectrum, which is the familiar frequency domain spectrum showing intensity versus frequency. This also explains how the term *Fourier transform infrared* spectrometry takes its name.

Appendix C

C.1. Electron spectroscopy with metastable atoms

Techniques based on the interaction of atoms or ions with low kinetic energy will exhibit the highest sensitivity for the outermost atomic layer of a surface, since these particles do not penetrate into the solid. Metastable atom electron spectroscopy (MAES) is essentially non-destructive, because metastable atoms are usually introduced only with thermal kinetic energies. The fact that electronically excited metastable noble gas atoms (A^*) de-excite with nearly unit probability at solid surfaces also makes MAES useful for surface analysis. However, the interpretation of the electronic spectra is never unambiguous due to the participation of more than one de-excitation mechanism. The de-excitation process is based on the interaction of A^* with the electronic states of the outermost surface layer and leads to emission of electrons.¹⁸³

An atom is in a metastable state if the transition into its ground state *via* photon emission is quantum mechanically forbidden. During its lifetime, the atom carries its excitation energy in the form of potential energy. Relevant properties of metastable He, Ne, and Ar atoms are listed in Table C.1, together with corresponding ground-state properties. The most commonly used atom in MIES source is helium.¹⁸⁴

	Electronic State	Excitation energy E^* (eV)	Ionisation potential E_i (eV)	Life time τ (s)
He	$^1S_0(1s^2)$	0.0	24.58	∞
	$^3S_1(1s\ 2s)$	19.82	4.77	4.2×10^3
	$^1S_0(1s\ 2s)$	21.62	3.97	4.2×10^{-2}
Ne	$^1S_0(2p^6)$	0.0	21.56	∞
	$^3P_2(2p^5\ 3s)$	16.62	4.95	24.4
Ar	$^1S_0(3p^6)$	0.0	15.76	∞
	$^3P_2(3p^5\ 4s)$	11.55	4.21	55.9

Table C.1: Properties of ground-state and metastable noble gas atoms.

C.2. De-excitation mechanisms

Metastable atoms may interact *via* different mechanisms depending on the surface electronic structure and work function of the system. On the solid

surface, rare gas metastable atoms de-excite through resonance ionisation (RI) followed by Auger neutralisation (AN) in addition to direct Penning ionisation (PI):



The RI+AN process proceeds at surfaces of ordinary metals and semiconductors. In RI, the electron in the outer orbital of the metastable atom tunnels into an empty level of the surface (target atoms, T). The positive ion thus formed is then neutralized through AN, in which an electron in the solid transfers to the vacant inner orbital of the ion and another electron in the solid is ejected. When an empty level of the surface is not present opposite to the outer level of the metastable atom as in the case of insulators, the metastable atom is de-excited through PI or Auger de-excitation (AD), in which an electron in the solid transfers to the inner vacant orbital of the metastable atom and the electron of the outer orbital is ejected.^{183,185}

It is generally observed that at clean and atomic-adsorbate-covered transition metal surfaces (with the exception of adsorbed alkali metal atoms) de-excitation occurs by RI followed by AN. Whereas at surfaces covered with molecular adsorbates frequently AD dominates.¹⁸⁴ These various steps which may be involved in the de-excitation of noble gas metastables at a surface are illustrated by Fig. C.1.

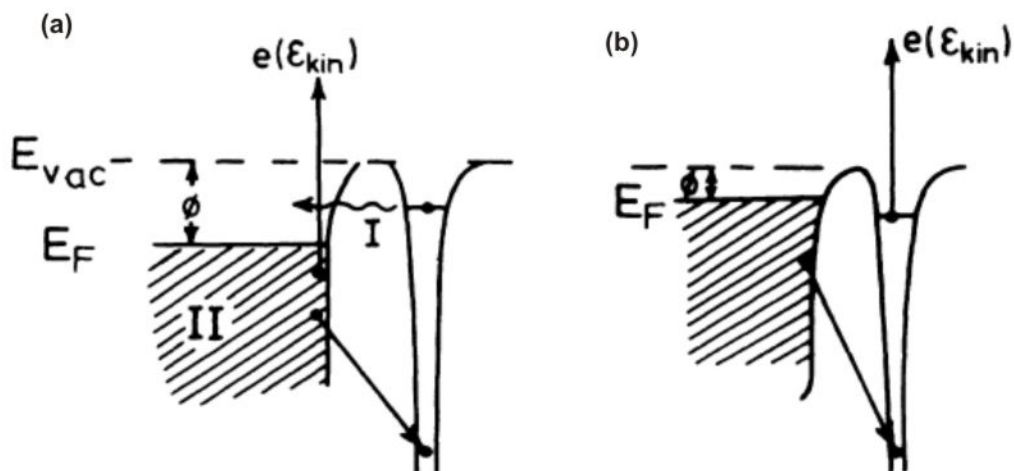


Fig. C.1: De-excitation mechanism of a metastable noble gas atom at surfaces. (a) De-excitation by resonance ionisation (I) followed by Auger neutralisation (II). (b) Auger de-excitation (AD). E_{kin} is the energy transferred to the emitted electron.¹⁸⁴

C.3. Instrumentation

Rare gas metastable beams are usually produced by three types of sources: electron bombardment, cold and hot discharge types. In operation, cold and hot cathode discharges give mainly $\text{He}^*(2^3\text{S})$ species, while electron bombardment produces some amount of $\text{He}^*(2^1\text{S})$, whose intensity depends on the collision energy of electrons.

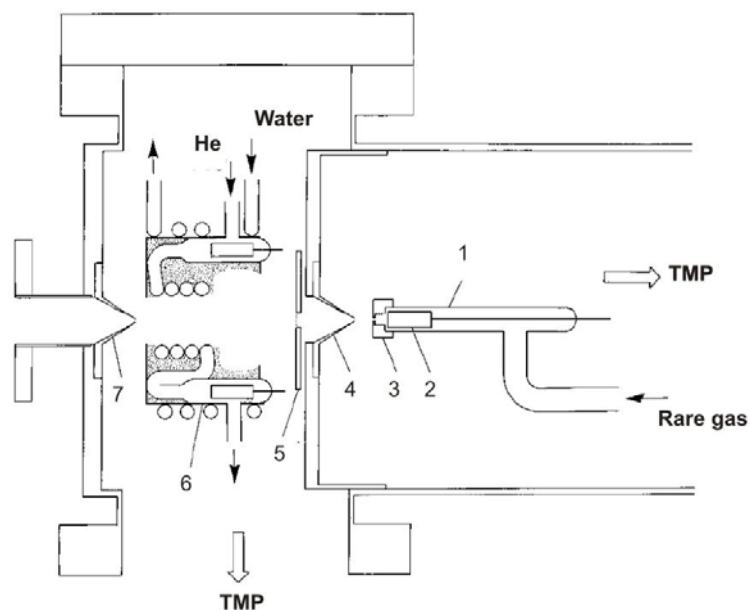


Fig. C.2: Metastable atom source: (1) Pyrex tube, (2) tantalum cathode, (3) boron nitride nozzle, (4) skimmer, (5) repeller grid, (6) quench lamp, and (7) skimmer.

Figure C.2 shows a cold cathode discharge source, originally designed by Leasure *et al.*¹⁸⁶ and Fahey *et al.*¹⁸⁷ The discharge is maintained between a tantalum hollow cathode 2 and stainless-steel skimmer 4 across a pressure gradient created by differential pumping. Electrons due to discharge are removed with a repeller grid 5. For the measurement of $\text{He}^*(2^3\text{S})$ spectra, $\text{He}^*(2^1\text{S})$ atoms are quenched *via* the transition of $2^1\text{S} \rightarrow n^1\text{P} \rightarrow 1^1\text{S}$ ($n = 2, 3, 4$, etc.) with the light from a helium discharge lamp 6. More than 99% of the $\text{He}^*(2^1\text{S})$ atoms are quenched with this type of lamp.¹⁸³

Appendix D

TPR simulations

```
#pragma rtGlobals=1          // Use modern global access method.

function
SimCO2_2(nEL,nTs,ndeltaT,TetaOs,TetaCOs,nHeatRate,nClusterCoverage,nClusterRadius,n
ClusterSites,nEDiffMgO,nMode)

Variable
nEL,nTs,ndeltaT,TetaOs,TetaCOs,nHeatRate,nClusterCoverage,nClusterRadius,nClusterSites,
nEDiffMgO,nMode // ClusterRadius m
Variable nL,nCZCO,nRoh,nRind,ndiffusiveCO
nL = 1e-2/((3.14*nClusterCoverage)^(0.5)) // Clustercoverage cm-2// nL m
nRind = 1e-10

string sFolder,sName,sPos,sNameC
sFolder = "EL_"+num2str(nEL)+"_"+num2str(nHeatRate)
sName = "EL_"+num2str(nEL)+"_"+num2str(nHeatRate)

variable i,j,k,kk

NewDataFolder/S $sFolder
Make/N=1000 AllCO2

if (nMode == 0)
    kk = 1
    else
    kk=100
endif

for (k=0;k<kk;k+=1)

    Make/N=1000/O wTemperature, wkL, wkD, wEDes,wTetaO,
wTetaCO,wRCO2,wXs,wPBess,wAlphaG
    Make/N=1000/O
wJdiff,wCaptureZ,wDdiff,wEDesMgO,wTetaMgO,wEdesRind,wTetaRind

    wTemperature [0] = nTs
    wTetaO[0] = TetaOs
    wXs[0] = (3e-10)*exp(24121/(2*(8.314)*nTs)) // in m; Esad = 24121 J/mol
    wPBess[0] = (Besseli(1,(nL/wXs[0]))*Besselk(1,(nClusterRadius/wXs[0]))-
Besselk(1,(nL/wXs[0]))*Besseli(1,(nClusterRadius/wXs[0])))/(Besseli(1,(nL/wXs[0]))*Besselk(0,(
nClusterRadius/wXs[0]))+Besselk(1,(nL/wXs[0]))*Besseli(0,(nClusterRadius/wXs[0])))
    wAlphaG[0] =
3.14*nClusterCoverage*1e4*(2*0.5*nClusterRadius*wXs[0]*wPBess[0]+nClusterRadius*nCluste
rRadius)
    wJdiff[0] = 2*3.14*nClusterRadius*wXs[0]*0.5*wPBess[0]*1.25e19
    wCaptureZ[0] = 2*3.14*nClusterRadius*wXs[0]*wPBess[0] // Capture Zone Area
    wTetaCO[0] = TetaCOs+wJdiff[0]*wCaptureZ[0]/0.5
    wkL[0] = (10^(7.9))*exp((-nEL*1000)/(8.314*nTs))
    wEDes [0] = 118000*0.9
    wkD[0] = 1e14*exp(-118000*0.9/(8.314*nTs))
    wRCO2[0] = wkL[0]*wTetaO[0]*wTetaCO[0]
    wDdiff[0] = (9e-20)*exp(-nEDiffMgO/(8.314*nTs))*1e10 //vD = 1e10!!
    wEDesMgO [0] = 90000*0.9
    wTetaMgO[0] = 0.5
```

TPR simulations

```
wEdesRind [0] =80000
wTetaRind [0] = 0

nCZCO = 2.2e19*wCaptureZ[0]/2 // #of CO molecules inside the capture zone in case
of saturation (coverage = 0.5)
nRoh = (((2*3.14*nClusterRadius)^2+4*3.14*wCaptureZ[0])^(0.5)-
2*3.14*nClusterRadius)/6.28

for (i=1;i<1000;i+=1)

    //ndiffusiveCO = 0

    wTemperature [i] = nTs+ndeltaT*i

    wDdiff[i] = (9e-20)*exp(-10131/(8.314*wTemperature[i]))*1e10 //vD = 1e10!!

    wkL[i] = (10^(7.9))*exp((-nEL*1000)/(8.314*wTemperature[i]))

    wTetaO[i] = wTetaO[i-1]-(wkL[i-1]*wTetaCO[i-1]*wTetaO[i-
1])*(ndeltaT/nHeatRate)

    wXs[i] = (3e-10)*exp(24121/(2*(8.314)*wTemperature[i])) // in m; Esad = 24121
J/mol

    wPBess[i] = (Besseli(1,(nL/wXs[i]))*Besselk(1,(nClusterRadius/wXs[i]))-
Besselk(1,(nL/wXs[i]))*Besseli(1,(nClusterRadius/wXs[i])))/(Besseli(1,(nL/wXs[i]))*Besselk(0,(nClu
sterRadius/wXs[i]))+ Besselk(1,(nL/wXs[i]))*Besseli(0,(nClusterRadius/wXs[i])))

    wAlphaG[i] = 3.14*nClusterCoverage*1e+4*
(2*0.5*nClusterRadius*wXs[i]*wPBess[i]+nClusterRadius*nClusterRadius)

    wJdiff[i] = 2*3.14*nClusterRadius*wXs[i]*0.5*wPBess[i]*1.25e19

    wCaptureZ[i] = 2*3.14*nClusterRadius*wXs[i]*wPBess[i]

    for(j=0;j<nCZCO;j+=1)

        XdiffusiveCO[j] = XdiffusiveCO[j]+((-1)^(floor(abs(enoise(1))+1.5)))
(wDdiff[i]*(ndeltaT/nHeatRate))^(0.5)

        if (XdiffusiveCO[j]< (nClusterRadius+nRind))

            ndiffusiveCO +=1
            //print j,"got to cluster",i,COMgOPos[j]
            XdiffusiveCO[j] = nClusterRadius+nRind

        endif

    endfor

    wTetaMgO[i] = wTetaMgO[i-1]-((1e14*exp(-wEDesMgO[i-
1]/(8.314*wTemperature[i-1]))*wTetaMgO[i-1]) +1e10*exp(-nEDiffMgO/(8.314*wTemperature[i-
1]))*wTetaMgO[i-1])*(ndeltaT/nHeatRate)

    wEDesMgO [i] = 90000*(1-(wTetaMgO[i]/5))

    wTetaRind [i] = wTetaRind[i-1]-((1e14*exp(-wEDesRind[i-
1]/(8.314*wTemperature[i-1]))*wTetaMgO[i-1])-1e10*exp(-nEDiffMgO/(8.314*wTemperature[i-
1]))*wTetaMgO[i-1])*(ndeltaT/nHeatRate)-0.5*wTetaRind[i-1]*
(3.14*nRind*(nRind+2*nClusterRadius)*1e15)/nClusterSites
```

```

        if (wTetaRind[i]>0.5)
            wTetaRind[i]=0.5
        endif
        if (wTetaRind[i]<0)
            wTetaRind[i]=0
        endif
        if (wTetaMgO[i]<0)
            wTetaMgO[i]=0
        endif
        wEdesRind [i] =80000*(1-(wTetaRind[i]/5))
        if (nMode == 0)
            wTetaCO[i] = wTetaCO[i-1]-(wkL[i-1]*wTetaCO[i-1]*wTetaO[i-1]+wkD[i-1]*wTetaCO [i-1]) *(ndeltaT/nHeatRate)
        else
            wTetaCO[i] = 0.5*wTetaRind[i-1]
            *(3.14*nRind*(nRind+2*nClusterRadius)*2.2e15)/nClusterSites+wTetaCO[i-1]-(wkL[i-1]*wTetaCO[i-1]*wTetaO[i-1]+wkD[i-1]*wTetaCO [i-1]) *(ndeltaT/nHeatRate)
        endif
        if (wTetaCO[i]>0.5)
            wTetaCO[i]=0.5
            //ndiffusiveCO -=1
        endif
        wEDes[i] = 118000*(1-(wTetaCO[i]/5))
        wkD [i] = 1e14*exp(-wEDes[i]/(8.314*wTemperature[i]))
        wRCO2[i] = wkL[i]*wTetaO[i]*wTetaCO[i]
    endfor
    sNameC = "EL_"+num2str(nEL)+"_"+num2str(nHeatRate)+num2str(k)
    Duplicate wRCO2 $sNameC
    AllCO2 = AllCO2+wRCO2
endfor
//print ndiffusiveCO

SetDataFolder root:

End

```


Acknowledgements

I would like to firstly thank my supervisor Prof. Ulrich Heiz, for his constant support and advice given me throughout my PhD thesis. I greatly appreciate his proofreading and guidance for writing this dissertation.

I am very thankful to Dr. Christopher Harding for his constant advice, help, and friendship throughout my PhD. Thanks to Sebastian Kunz for the time working together in the lab.

Special thanks to my friend, Dr. Jean-Marie Antoneitti for his support since my graduate days. I would also like to extend my thanks to Dr. Marina Pivetta and Markus Bieletzki for their friendship during my PhD studies.

I would like to acknowledge Sean Aston for proofreading some chapters of this dissertation. Thanks to Dr. Matthias Arenz, Dr. Martin Röttgen and Viktoria Teslenko for working together in the lab in the first couple of months of my PhD. Thanks to all staffs of the electrical and mechanical workshop of the Technische Universität München.

To Aras, I am forever grateful for the true love and unconditional support he has me, encouraging me to be the best I can be. Many thanks to my family from bottom of my heart for being always there for me.

References

- (1) Heiz, U.; Landman, U. *Nanocatalysis*; Springer: New York, 2006.
- (2) Sanchez, A.; Abbet, S.; Heiz, U.; Schneider, W. D.; Hakkinen, H.; Barnett, R. N.; Landman, U. *The Journal of Physical Chemistry A* **1999**, *103*, 9573.
- (3) Reinhard, P.-G.; Suraud, E. *Introduction to Cluster Dynamics*; WILEY-VCH: Weinheim, 2004.
- (4) Ertl, G.; Freund, H.-J. *Physics Today* **1999**, *52*, 32.
- (5) Henry, C. R.; Chapon, C.; Giorgio, S.; Goyhenex, C. *Chemisorption and Reactivity on Supported Clusters and Thin Films - Towards an Understanding of Microscopic Processes in Catalysis* **1997**, *331*, 117.
- (6) Libuda, J.; Meusel, I.; Hoffmann, J.; Hartmann, J.; Piccolo, L.; Henry, C. R.; Freund, H. J. *The Journal of Chemical Physics* **2001**, *114*, 4669.
- (7) Landman, U.; Yoon, B.; Zhang, C.; Heiz, U.; Arenz, M. *Topics in Catalysis* **2007**, *44*, 145.
- (8) Kao, C. C.; Tsai, S. C.; Bahl, M. K.; Chung, Y. W.; Lo, W. J. *Surface Science* **1980**, *95*, 1.
- (9) Haruta, M. *CATTECH* **2002**, *6*, 102.
- (10) Schubert, M. M.; Hackenberg, S.; van Veen, A. C.; Muhler, M.; Plzak, V.; Behm, R. J. *Journal of Catalysis* **2001**, *197*, 113.
- (11) Tauster, S. J.; Fung, S. C.; Garten, R. L. *Journal of the American Chemical Society* **1978**, *100*, 170.
- (12) Tauster, S. J.; Fung, S. C.; Baker, R. T. K.; Horsley, J. A. *Science* **1981**, *211*, 1121.
- (13) Hakkinen, H.; Manninen, M. *The Journal of Chemical Physics* **1996**, *105*, 10565.
- (14) Pacchioni, G.; Rösch, N. *Surface Science* **1994**, *306*, 169.
- (15) Mavrikakis, M.; Stoltze, P.; Nørskov, J. K. *Catalysis Letters* **2000**, *64*, 101.
- (16) Giordano, L.; Goniakowski, J.; Pacchioni, G. *Physical Review B* **2001**, *64*, 075417.
- (17) Wertheim, G. K. *Zeitschrift für Physik D Atoms, Molecules and Clusters* **1989**, *12*, 319.
- (18) Haruta, M. *Catalysis Today* **1997**, *36*, 153.
- (19) Heiz, U.; Sanchez, A.; Abbet, S.; Schneider, W. D. *Journal of the American Chemical Society* **1999**, *121*, 3214.
- (20) Henry, C. R. *Surface Science Reports* **1998**, *31*, 231.
- (21) Piccolo, L.; Henry, C. R. *Journal of Molecular Catalysis A: Chemical* **2001**, *167*, 181.
- (22) Molina, L. M.; Hammer, B. *Journal of Catalysis* **2005**, *233*, 399.
- (23) Heiz, U.; Schneider, W. D. *Journal of Physics D-Applied Physics* **2000**, *33*, R85.
- (24) Abbet, S.; Riedo, E.; Brune, H.; Heiz, U.; Ferrari, A. M.; Giordano, L.; Pacchioni, G. *Journal of the American Chemical Society* **2001**, *123*, 6172.
- (25) Hakkinen, H.; Abbet, W.; Sanchez, A.; Heiz, U.; Landman, U. *Angewandte Chemie-International Edition* **2003**, *42*, 1297.
- (26) Kohiki, S.; Ikeda, S. *Physical Review B* **1986**, *34*, 3786.
- (27) Cai, Y. Q.; Bradshaw, A. M.; Guo, Q.; Goodman, D. W. *Surface Science* **1998**, *399*, L357.
- (28) Heiz, U.; Vanolli, F.; Sanchez, A.; Schneider, W. D. *Journal of the American Chemical Society* **1998**, *120*, 9668.
- (29) Heiz, U.; Bullock, E. L. *Journal of Materials Chemistry* **2004**, *14*, 564.
- (30) Billas, I. M. L.; Chatelain, A.; de Heer, W. A. *Science* **1994**, *265*, 1682.
- (31) Broqvist, P.; Molina, L. M.; Grönbeck, H.; Hammer, B. *Journal of Catalysis* **2004**, *227*, 217.
- (32) Campbell, C. T. *Surface Science Reports* **1997**, *27*, 1.
- (33) Kulawik, M.; Nilius, N.; Freund, H. J. *Physical Review Letters* **2006**, *96*, 036103.

- (34) Moseler, M.; Häkkinen, H.; Landman, U. *Physical Review Letters* **2002**, *89*, 176103.
- (35) Ferrari, A. M.; Pacchioni, G. *The Journal of Physical Chemistry* **1996**, *100*, 9032.
- (36) Giordano, L.; Pacchioni, G. *Physical Chemistry Chemical Physics* **2006**, *8*, 3335.
- (37) Onishi, H.; Aruga, T.; Egawa, C.; Iwasawa, Y. *Surface Science* **1988**, *199*, 54.
- (38) Zhang, Z.; Henrich, V. E. *Surface Science* **1992**, *277*, 263.
- (39) Dake, L. S.; Lad, R. J. *Surface Science* **1993**, *289*, 297.
- (40) Magkoev, T. T.; Vladimirov, G. G. *Journal of Physics: Condensed Matter* **2001**, L655.
- (41) Giordano, L.; Goniakowski, J.; Pacchioni, G. *Physical Review B* **2003**, *67*, 045410.
- (42) Giordano, L.; Cinquini, F.; Pacchioni, G. *Physical Review B (Condensed Matter and Materials Physics)* **2006**, *73*, 045414.
- (43) Pivetta, M.; Patthey, F.; Stengel, M.; Baldereschi, A.; Schneider, W.-D. *Physical Review B* **2005**, *72*, 115404.
- (44) Loppacher, C.; Zerweck, U.; Eng, L. M. *Nanotechnology* **2004**, S9.
- (45) Rainer, D. R.; Vesecky, S. M.; Koranne, M.; Oh, W. S.; Goodman, D. W. *Journal of Catalysis* **1997**, *167*, 234.
- (46) Kolehmainen, J.; Häkkinen, H.; Manninen, M. *Zeitschrift für Physik D Atoms, Molecules and Clusters* **1997**, *40*, 306.
- (47) Sun, D. Y.; Gong, X. G. *Journal of Physics: Condensed Matter* **1997**, 10555.
- (48) Huber, B.; Koskinen, P.; Hakkinen, H.; Moseler, M. *Nat Mater* **2006**, *5*, 44.
- (49) Pacchioni, G.; Rosch, N. *The Journal of Chemical Physics* **1996**, *104*, 7329.
- (50) Cunningham, D.; Tsubota, S.; Kamijo, N.; Haruta, M. *Research on Chemical Intermediates* **1993**, *19*, 1.
- (51) Liu, Z. M.; Vannice, M. A. *Catalysis Letters* **1997**, *43*, 51.
- (52) Ricci, D.; Bongiorno, A.; Pacchioni, G.; Landman, U. *Physical Review Letters* **2006**, *97*, 036106.
- (53) Broqvist, P.; Grönbeck, H. *Surface Science* **2006**, *600*, L214.
- (54) Sterrer, M.; Risse, T.; Heyde, M.; Rust, H. P.; Freund, H. J. *Physical Review Letters* **2007**, 98.
- (55) Bondzie, V. A.; Parker, S. C.; Campbell, C. T. "Oxygen adsorption on well-defined gold particles on TiO₂(110)"; Papers from the 45th National Symposium of the American Vacuum Society, 1999, Baltimore, Maryland (USA).
- (56) Molina, L. M.; Hammer, B. *Physical Review B* **2004**, *69*, 155424.
- (57) Molina, L. M.; Hammer, B. *Physical Review Letters* **2003**, *90*, 206102.
- (58) Ioannis N. Remediakis, N. L. J. K. N. *Angewandte Chemie International Edition* **2005**, *44*, 1824.
- (59) Henry, C. R. *Surface Science* **1989**, *223*, 519.
- (60) Henry, C. R.; Chapon, C.; Duriez, C. *The Journal of Chemical Physics* **1991**, *95*, 700.
- (61) Rottgen, M. A.; Abbet, S.; Judai, K.; Antonietti, J.-M.; Worz, A. S.; Arenz, M.; Henry, C. R.; Heiz, U. *Journal of the American Chemical Society* **2007**, *129*, 9635.
- (62) Hagen, J.; Socaciu, L. D.; Elijazyfer, M.; Heiz, U.; Bernhardt, T. M.; Woste, L. *Physical Chemistry Chemical Physics* **2002**, *4*, 1707.
- (63) Hagen, J.; Socaciu, L. D.; Le Roux, J.; Popolan, D.; Bernhardt, T. M.; Woste, L.; Mitric, R.; Noack, H.; Bonacić-Koutecky, V. *Journal of the American Chemical Society* **2004**, *126*, 3442.
- (64) Cunningham, D. A. H.; Vogel, W.; Haruta, M. *Catalysis Letters* **1999**, *63*, 43.
- (65) Daté, M.; Haruta, M. *Journal of Catalysis* **2001**, *201*, 221.
- (66) Daté, M.; Okumura, M.; Tsubota, S.; Haruta, M. *Angewandte Chemie International Edition* **2004**, *43*, 2129.

- (67) Calla, J. T.; Davis, R. J. *Journal of Catalysis* **2006**, *241*, 407.
- (68) Wallace, W. T.; Wyrwas, R. B.; Whetten, R. L.; Mitric, R.; Bonacic-Koutecky, V. *Journal of the American Chemical Society* **2003**, *125*, 8408.
- (69) Bongiorno, A.; Landman, U. *Physical Review Letters* **2005**, *95*, 106102.
- (70) Heiz, U.; Vanolli, F.; Trento, L.; Schneider, W. D. *Review of Scientific Instruments* **1997**, *68*, 1986.
- (71) Rottgen, M. A.; Judai, K.; Antonietti, J. M.; Heiz, U.; Rauschenbach, S.; Kern, K. *Review of Scientific Instruments* **2006**, *77*.
- (72) Röttgen, A. M. Untersuchung von katalytischen Eigenschaften gröÙenselektierter Clusters mittels gepulster Molekularstrahlen. Dissertation, Technische Universität München, 2007.
- (73) Wörz, A. S. Oxidation reactions on nanoassembled model catalysts. Dissertation, Universität Ulm, 2005.
- (74) Vanolli, F. Properties of size-selected and supported metal clusters, de l'Universite de Lausanne, 1997.
- (75) Ochs, D.; Maus-Friedrichs, W.; Brause, M.; Günster, J.; Kempter, V.; Puchin, V.; Shluger, A.; Kantorovich, L. *Surface Science* **1996**, *365*, 557.
- (76) Judai, K.; Abbet, S.; Worz, A. S.; Rottgen, M. A.; Heiz, U. *International Journal of Mass Spectrometry* **2003**, *229*, 99.
- (77) Somorjai, G. *Introduction to surface chemistry and catalysis*; Wiley & Son: New York, 1994.
- (78) Majni, G.; Ottaviani, G.; Prudenziati, M. *Thin Solid Films* **1976**, *38*, 15.
- (79) Zhang, X. R.; Xu, X. *Applied Physics Letters* **2005**, *86*, 021114.
- (80) Gimzewski, J. K.; Gerber, C.; Meyer, E.; Schlittler, R. R. *Chemical Physics Letters* **1994**, *217*, 589.
- (81) Antonietti, J.-M.; Gong, J.; Habibpour, V.; Rottgen, M. A.; Abbet, S.; Harding, C. J.; Arenz, M.; Heiz, U.; Gerber, C. *Review of Scientific Instruments* **2007**, *78*, 054101.
- (82) Schintke, S.; Messerli, S.; Pivetta, M.; Patthey, F.; Libioulle, L.; Stengel, M.; De Vita, A.; Schneider, W.-D. *Physical Review Letters* **2001**, *87*, 276801.
- (83) Valeri, S.; Altieri, S.; del Pennino, U.; di Bona, A.; Luches, P.; Rota, A. *Physical Review B* **2002**, *65*, 245410.
- (84) Silvia, S.; Wolf-Dieter, S. *Journal of Physics: Condensed Matter* **2004**, R49.
- (85) Gallagher, M. C.; Fyfield, M. S.; Bumm, L. A.; Cowin, J. P.; Joyce, S. A. *Thin Solid Films* **2003**, *445*, 90.
- (86) Kim, Y. D.; Stultz, J.; Goodman, D. W. *Surface Science* **2002**, *506*, 228.
- (87) Freund, H. J.; Kuhlbeck, H.; Libuda, J.; Rupprechter, G.; Bäumer, M.; Hamann, H. *Topics in Catalysis* **2001**, *15*, 201.
- (88) Kolmakov, A.; Stultz, J.; Goodman, D. W. *The Journal of Chemical Physics* **2000**, *113*, 7564.
- (89) Wu, M.-C.; Corneille, J. S.; Estrada, C. A.; He, J.-W.; Wayne Goodman, D. *Chemical Physics Letters* **1991**, *182*, 472.
- (90) Wu, M.-C.; Corneille, J. S.; He, J.-W.; Estrada, C. A.; Goodman, D. W. *Journal of Vacuum Science Technology A* **1992**, *10*, 1467.
- (91) Di Valentin, C.; Del Vitto, A.; Pacchioni, G.; Abbet, S.; Worz, A. S.; Judai, K.; Heiz, U. *Journal of Physical Chemistry B* **2002**, *106*, 11961.
- (92) Xu, X.; Goodman, D. W. *Surface Science* **1993**, *282*, 323.
- (93) Lawrence E. Davis, N. C. M., Paul W. Palmberg, Gerald E. Riach, Roland E. Weber *Handbook of Auger Electron Spectroscopy*; Physical Electronics Industries, Inc.: Eden Prairie, Minnesota 55343, 1976.
- (94) Wendt, S.; Kim, Y. D.; Goodman, D. W. *Progress in Surface Science* **2003**, *74*, 141.
- (95) Bielezki, M. *to be published* **2009**.
- (96) Gunster, J.; Liu, G.; Kempter, V.; Goodman, D. W. "Coadsorption of sodium and water on MgO(100)/Mo(100) studied by ultraviolet photoelectron and

- metastable impact electron spectroscopies"; Papers from the 44th national symposium of the AVS, 1998, San Jose, California (USA).
- (97) Kantorovich, L.; Shluger, A.; Günster, J.; Stultz, J.; Krischok, S.; Goodman, D. W.; Stracke, P.; Kempter, V. *Nuclear Instruments and Methods in Physics Research Section B: Beam Interactions with Materials and Atoms* **1999**, *157*, 162.
- (98) Günster, J.; Krischok, S.; Kempter, V.; Stultz, J.; Goodman, D. W. *Surface Review and Letters* **2001**, *9*, 1511.
- (99) Stracke, P. R. Elektronenspektroskopische Untersuc der Metalladsorption auf MgO, TU Clausthal, 2000.
- (100) Cvetanovi, R. J.; Amenomiya, Y. *Catalysis Reviews* **1972**, *6*, 21.
- (101) Falconer, J. L.; Schwarz, J. A. *Catalysis Reviews* **1983**, *25*, 141
- (102) Engel, T. *The Journal of Chemical Physics* **1978**, *69*, 373.
- (103) Engel, T.; Ertl, G. *The Journal of Chemical Physics* **1978**, *69*, 1267.
- (104) Harding, C. J.; Kunz, S.; Habibpour, V.; Teslenko, V.; Arenz, M.; Heiz, U. *Journal of Catalysis* **2008**, *255*, 234.
- (105) Taylor, J. B.; Langmuir, I. *Physical Review* **1933**, *44*, 423.
- (106) Kisliuk, P. *Journal of Physics and Chemistry of Solids* **1957**, *3*, 95.
- (107) Mieher, W. D.; Ho, W. *The Journal of Chemical Physics* **1993**, *99*, 9279.
- (108) Heiz, U.; Sanchez, A.; Abbet, S.; Schneider, W. D. *European Physical Journal D* **1999**, *9*, 35.
- (109) Campbell, C. T.; Ertl, G.; Kuipers, H.; Segner, J. *The Journal of Chemical Physics* **1980**, *73*, 5862.
- (110) Coulston, G. W.; Haller, G. L. *The Journal of Chemical Physics* **1991**, *95*, 6932.
- (111) Bernasek, S. L.; Leone, S. R. *Chemical Physics Letters* **1981**, *84*, 401.
- (112) Dohnalek, Z.; Kimmel, G. A.; Joyce, S. A.; Ayotte, P.; Smith, R. S.; Kay, B. D. *The Journal of Physical Chemistry B* **2001**, *105*, 3747.
- (113) Blyholder, G. *The Journal of Physical Chemistry* **1964**, *68*, 2772.
- (114) Moulijn, J. A.; M. van Leeuwen, P. W. N.; A. van Santen, R. Chapter 4 Bonding and elementary steps in catalysis. In *Studies in Surface Science and Catalysis*; Elsevier, 1993; Vol. Volume 79; pp 89.
- (115) Palmer, R. L.; Smith, J. J. N. *The Journal of Chemical Physics* **1974**, *60*, 1453.
- (116) Kuppens, J.; Plagge, A. *Journal of Vacuum Science and Technology* **1976**, *13*, 259.
- (117) Baddour, R. F.; Modell, M.; Heusser, U. K. *The Journal of Physical Chemistry* **1968**, *72*, 3621.
- (118) Ackermann, M. D.; Pedersen, T. M.; Hendriksen, B. L. M.; Robach, O.; Bobaru, S. C.; Popa, I.; Quiros, C.; Kim, H.; Hammer, B.; Ferrer, S.; Frenken, J. W. M. *Physical Review Letters* **2005**, *95*, 255505.
- (119) Hendriksen, B. L. M.; Bobaru, S. C.; Frenken, J. W. M. *Surface Science* **2004**, *552*, 229.
- (120) Scott, S. K. *Oscillations, Waves and Chaos in Chemical Kinetics*; Oxford University Press, 1994.
- (121) Ladas, S.; Imbihl, R.; Ertl, G. *Surface Science* **1989**, *219*, 88.
- (122) Turner, J. E.; Sales, B. C.; Maple, M. B. *Surface Science* **1981**, *103*, 54.
- (123) Collins, N. A.; Sundaresan, S.; Chabal, Y. J. *Surface Science* **1987**, *180*, 136.
- (124) Conrad, H.; Ertl, G.; Küppers, J.; Latta, E. E. *Surface Science* **1977**, *65*, 235.
- (125) Conrad, H.; Ertl, G.; Küppers, J.; Latta, E. E. *Surface Science* **1977**, *65*, 245.
- (126) Harding, C. J.; Kunz, S.; Habibpour, V.; Heiz, U. *Physical Chemistry Chemical Physics* **2008**, *10*, 5875.
- (127) Hoffmann, J.; Meusel, I.; Hartmann, J.; Libuda, J.; Freund, H. J. *Journal of Catalysis* **2001**, *204*, 378.
- (128) Harding, C. J.; Kunz, S.; Habibpour, V.; Heiz, U. *Chemical Physics Letters* **2008**, *461*, 235.
- (129) Matolin, V.; Gillet, E. *Surface Science* **1986**, *166*, L115.
- (130) Conrad, H.; Ertl, G.; Küppers, J. *Surface Science* **1978**, *76*, 323.

- (131) Engel, T.; Ertl, G. *Journal of Chemical Physics* **1978**, *69*, 1267.
- (132) Sterrer, M.; Risse, T.; Freund, H.-J. *Surface Science* **2005**, *596*, 222.
- (133) Sterrer, M.; Risse, T.; Freund, H.-J. *Applied Catalysis A: General* **2006**, *307*, 58.
- (134) Haruta, M.; Kobayashi, T.; Sano, H.; Yamada, N. *Chemistry Letters* **1987**, *16*, 405.
- (135) Haruta, M.; Yamada, N.; Kobayashi, T.; Iijima, S. *Journal of Catalysis* **1989**, *115*, 301.
- (136) Valden, M.; Lai, X.; Goodman, D. W. *Science* **1998**, *281*, 1647.
- (137) Sault, A. G.; Madix, R. J.; Campbell, C. T. *Surface Science* **1986**, *169*, 347.
- (138) Hammer, B.; Norskov, J. K. *Nature* **1995**, *376*, 238.
- (139) Haruta, M.; Tsubota, S.; Kobayashi, T.; Kageyama, H.; Genet, M. J.; Delmon, B. *Journal of Catalysis* **1993**, *144*, 175.
- (140) Yoon, B.; Hakkinen, H.; Landman, U.; Worz, A. S.; Antonietti, J. M.; Abbet, S.; Judai, K.; Heiz, U. *Science* **2005**, *307*, 403.
- (141) Campbell, C. T. *Science* **2004**, *306*, 234.
- (142) Haruta, M.; Daté, M. *Applied Catalysis A: General* **2001**, *222*, 427.
- (143) Herzing, A. A.; Kiely, C. J.; Carley, A. F.; Landon, P.; Hutchings, G. J. *Science* **2008**, *321*, 1331.
- (144) Kresse, G.; Furthmüller, J. *Phys. Rev. B* **1996**, *54*, 11169.
- (145) Kresse, G.; Hafner, J. *Phys. Rev. B* **1993**, *47*, R558.
- (146) Perdew, J. P.; Chevary, J. A.; Vosko, S. H.; Jackson, K. A.; Pederson, M. R.; Singh, D. J.; Fiolhais, C. *Phys. Rev. B* **1992**, *46*, 6671.
- (147) Vanderbilt, D. *Phys. Rev. B* **1990**, *41*, 7892.
- (148) Bielecki, M. Charakterisierung dünner MgO-Filme auf Ag(001) und massenselektierten Clustern auf HOPG mittels Rastersondenteknik. Dissertation, Technische Universität München, 2009.
- (149) Yoon, B.; Landman, U.; Würz, A.; Antonietti, J.-M.; Abbet, S.; Judai, K.; Heiz, U. *Science* **2005**, *307*, 403.
- (150) Harding, C.; Habibpour, V.; Kunz, S.; Farnbacher, A. N.-S.; Heiz, U.; Yoon, B.; Landman, U. *Journal of the American Chemical Society* **2009**, *131*, 538.
- (151) Zhang, C.; Yoon, B.; Landman, U. *J. Am. Chem. Soc.* **2007**, *129*, 2228.
- (152) Linsmeier, C.; Knözinger, H.; Taglauer, E. *Nuclear Instruments and Methods in Physics Research Section B: Beam Interactions with Materials and Atoms* **1996**, *118*, 533.
- (153) Schalow, T.; Brandt, B.; Starr, D.; Laurin, M.; Schauermaun, S.; Shaikhtudinov, S.; Libuda, J.; Freund, H. J. *Catalysis Letters* **2006**, *107*, 189.
- (154) Rumpf, F.; Poppa, H.; Boudart, M. *Langmuir* **1988**, *4*, 722.
- (155) Becker, C.; Henry, C. R. *Surface Science* **1996**, *352-354*, 457.
- (156) Heiz, U.; Sanchez, A.; Abbet, S.; Schneider, W. D. *Chemical Physics* **2000**, *262*, 189.
- (157) Huber, B.; Moseler, M. *The European Physical Journal D - Atomic, Molecular, Optical and Plasma Physics* **2007**, *45*, 485.
- (158) Eischens, R. P.; Pliskin, W. A.; Eley, D. D.; Frankenburg, W. G.; Komarewsky, V. I.; Weisz, P. B. The Infrared Spectra of Adsorbed Molecules. In *Advances in Catalysis*; Academic Press, 1958; Vol. Volume 10; pp 1.
- (159) Baddour, R. F.; Modell, M.; Goldsmith, R. L. *The Journal of Physical Chemistry* **1970**, *74*, 1787.
- (160) Hoffmann, F. M. *Surface Science Reports* **1983**, *3*, 107.
- (161) Worz, A. S.; Judai, K.; Abbet, S.; Heiz, U. *Journal of the American Chemical Society* **2003**, *125*, 7964.
- (162) Battiston, F. M.; Ramseyer, J. P.; Lang, H. P.; Baller, M. K.; Gerber, C.; Gimzewski, J. K.; Meyer, E.; Güntherodt, H. J. *Sensors and Actuators B: Chemical* **2001**, *77*, 122.
- (163) Barnes, J. R.; Stephenson, R. J.; Woodburn, C. N.; O'Shea, S. J.; Welland, M. E.; Rayment, T.; Gimzewski, J. K.; Gerber, C. *Review of Scientific Instruments* **1994**, *65*, 3793.

- (164) Lang, H. P.; Berger, R.; Battiston, F.; Ramseyer, J. P.; Meyer, E.; Andreoli, C.; Brugger, J.; Vettiger, P.; Despont, M.; Mezzacasa, T.; Scandella, L.; Güntherodt, H. J.; Gerber, C.; Gimzewski, J. K. *Applied Physics A: Materials Science & Processing* **1998**, *66*, S61.
- (165) McKendry, R.; Zhang, J.; Arntz, Y.; Strunz, T.; Hegner, M.; Lang, H. P.; Baller, M. K.; Certa, U.; Meyer, E.; Güntherodt, H.-J.; Gerber, C. *Proceedings of the National Academy of Sciences of the United States of America* **2002**, *99*, 9783.
- (166) Bachels, T.; Schafer, R. *Review of Scientific Instruments* **1998**, *69*, 3794.
- (167) Binnig, G.; Quate, C. F.; Gerber, C. *Physical Review Letters* **1986**, *56*, 930.
- (168) Bachels, T.; Tiefenbacher, F.; Schafer, R. *The Journal of Chemical Physics* **1999**, *110*, 10008.
- (169) Lide, D. R. *CRC Handbook of Chemistry and Physics*, 53rd ed.; CRC Press/Taylor and Francis: Boca Raton, FL.
- (170) Haberland, H.; Buck, U.; Tolle, M. *Review of Scientific Instruments* **1985**, *56*, 1712.
- (171) Watari, N.; Ohnishi, S. *Phys. Rev. B* **1998**, *58*, 1665.
- (172) Vervisch, W.; Mottet, C.; Goniakowski, J. *Physical Review B* **2002**, *65*, 245411.
- (173) Hoffmann, E.; Stroobant, V. *Mass Spectrometry Principles and Applications*, 2nd ed.; John Wiley & Sons, LTD: West-Sussex, 2001.
- (174) McLafferty, F. W.; Stauffer, D. B. *The Wiley/NBS Registry of Mass Spectral Data*; John Wiley & Sons, LTD: New York, 1988; Vol. 1.
- (175) Cox, J.; Pilcher, G. *Thermochemistry of Organic and Organometallic*; Academic Press: New York, 1970.
- (176) Auger, M. P. *Comptes Rendus Chemie* **1925**, *180*, 65.
- (177) Parker, S. P. *Spectroscopy Source Book*, 6th ed.; McGraw-Hill: New York, 1988.
- (178) Harris, L. A. *Journal of Applied Physics* **1968**, *39*, 1419.
- (179) Atkins, P. *Atkin's Physical Chemistry*, Seventh ed.; Oxford University Press, 2002.
- (180) Chourasia, A.; Chopra, D. R. *Handbook of Instrumental Techniques for Analytical Chemistry*.
- (181) Seah, M. P. *Methods of Surface Analysis*; Cambridge University Press: Cambridge, 1989.
- (182) Trenary, M. *Annual Review of Physical Chemistry* **2000**, *51*, 381.
- (183) Harada, Y.; Masuda, S.; Ozaki, H. *Chemical Reviews* **1997**, *97*, 1897.
- (184) Sesselmann, W.; Woratschek, B.; Küppers, J.; Ertl, G.; Haberland, H. *Physical Review B* **1987**, *35*, 1547.
- (185) Conrad, H.; Ertl, G.; Küppers, J.; Sesselmann, W.; Haberland, H. *Surface Science* **1982**, *121*, 161.
- (186) Leasure, E. L.; Mueller, C. R.; Ridley, T. Y. *Review of Scientific Instruments* **1975**, *46*, 635.
- (187) Fahey, D. W.; Parks, W. F.; Schearer, L. D. *Journal of Physics E: Scientific Instruments* **1980**, 381.